Investigating laser-nanoparticle interactions using time-resolved laser-induced incandescence

by

Stephen C. Robinson-Enebeli

A thesis

presented to the University of Waterloo

in fulfillment of the

thesis requirement for the degree of

Masters of Applied Science

in

Mechanical and Mechatronics Engineering (Nano)

Waterloo, Ontario, Canada, 2020

Author’s declaration

I hereby declare that I am the sole author of this thesis. This will be a true copy of the thesis, including any required final revisions, as accepted by my examiners.

I understand that my thesis may be made electronically available to the public.

Abstract

Nanotechnology is extending the frontiers of science and technology, mainly through the applications of engineered nanomaterials. For instance, metal nanoparticles have seen wide-spread applications in the fields of biomedicine, electronics, manufacturing and fabrication, and environmental remediation. Since the functionalities of nanoparticles are strongly size-dependent, there is a need for an accurate and streamlined diagnostic that meets the growing demand for engineered nanomaterials. Time-resolved laser-induced incandescence (TiRe-LII) is an *in situ* optical diagnostic technique that characterizes nanoparticle properties in the gas phase. In this technique, nanoparticles suspended in a gas are heated to incandescent temperatures with a laser and allowed to thermally equilibrate with the surrounding gas. The emitted incandescence are size-dependent and provide other information about the physical characteristics of the gas-phase nanoparticles. However, some anomalies have been reported in the literature, including excessive absorption and non-incandescent laser-induced emissions (LIE) that corrupt the TiRe-LII technique and introduce uncertainties to inferred results.

In this work, some of the anomalies that originate from the laser-nanoparticle interactions are investigated using the TiRe-LII modelling framework by applying tools such as the fluence study, examining the trends in inferred quantities-of-interest (QoI) that are inferred from an improved spectroscopic and heat transfer submodel, and analyzing LII data from plasmonic nanoparticles. The results show that LIE affects the inference of QoI, and further analysis of LII data from plasmonic nanoparticles can shed light on laser-nanoparticle interactions during TiRe-LII.

Acknowledgements

I would like to thank my supervisor, Dr. Kyle Daun, for giving me the opportunity to work on this amazing project and guiding me every step of the way. Thank you for being patient with my writing skills and encouraging me to be better, and finally, thank you for your mentorship and the many other opportunities during this project; it has all made me a much better researcher.

To all the wonderful folks at the National Research Council (NRC), Ottawa, Dr. Greg Smallwood, Dr. Prem Lobo, Dr. Fengshan Liu, Dr. Joel Corbin, Dr. Jalal Norooz Oliaee, Dr. Stéphanie Gagné, Dan Clavel, Simon-Alexandre Lussier, and Brett Smith. I appreciate all your help and support during my times on the campus and for making me feel like part of the fantastic research team. Of particular note, many thanks to Dan Clavel for patiently training me on the equipment. And to the researchers at the NRC campus on Sussex drive, Dr. Linda Johnston, Dr. Kennedy David, and Dr. Filip Kunc, thank you for your help and consultation on nanoparticle synthesis.

To Dr. Anna Klinkova and the researchers at the Klinkova lab, Kesinya Medvedeva, Dr. Iiuri Medvedev, and Stephen Tatarchuk, thank your help and collaboration. Of particular note, thanks to Kesinya Medvedeva for greatly assisting with nanoparticle synthesis and supplementing my chemistry knowledge.

Thank you to Andrew Kacheff for somehow always being available whenever I needed assistance for nanoparticle characterization. I also appreciated our long conversations that spanned a variety of topics.

Special thank you to Dr. Timothy Sipkens for providing expert consultation during the project, and to Dr. Robert Liang for assisting with some of the nanoparticle synthesis.

A very big thank you and appreciation to my wonderful colleagues at the Waterloo Laboratory for Inverse Analysis and Thermal Science (WatLIT) – Dr. Sina Talebi Moghaddam, Rodrigo Brenner, Stanislav Musikhin, Ned Zhou, Mohit Verma, Kaihsiang Lin, Roger Tsang, Fatima Suleiman, Tom Zhao, Cameron Klassen, Arpan Singh, and Michael Nagorski, thank you for your continuous support and companionship. Of particular note, many thanks to the LII-SSS-Team – Dr. Sina Talebi Moghaddam, for your patience and continuous assistance during this project, and Stanislav Musikhin, for always suggesting great ideas for experimental and troubleshooting tactics.

I would also like to thank my committee members, Dr. Kevin Musselman and Dr. Chao Tan. Your detailed review and thoughtful questions were much appreciated.

I am very grateful to the funding bodies: Natural Science and Engineering Research Council (NSERC), Waterloo Institute for Nanotechnology (WIN), and the province of Ontario. Your generosities were very much appreciated.

Finally, and most notably, I would like to thank my family; my parents – Robinson and Irene, my brothers – Reuben, Peter, and Gregory, and my love, Hiba Natsheh. Your continuous support, love, and patience throughout this experience were invaluable.

Nnéké nd'ibém, n'ékéné èshi òdum n'óbi

Table of contents

List of figures

List of tables

Nomenclature

This section provides a summary of the nomenclature used in this thesis document. There are occasionally overlapping symbols which are differentiated by the unit and definition.

Latin characters

Symbol	Unit	Definition
a_s	-	Scattering coefficient
$\mathbf{b}$	-	Observed data
b_s	-	Scattering coefficient
c_0	m/s	Speed of light in vacuum
$conc_{critical}$	mg/mL	Critical colloid concentration
c_g	m/s	Mean thermal speed of the gas
c_p	J/(kg·K)	Specific heat capacity
c_v	m/s	Mean thermal speed of the evaporated species
$C_{abs,\lambda}$	m^2, nm^2	Spectral absorption cross-section
C_λ	-	Calibration constant
d_p	m, nm	Nanoparticle diameter
E_i	J	Pre-collision energy
E_o	J	Post-collision energy
$E(\mathbf{m}_\lambda)$	-	Spectral absorption function
$E(\mathbf{m})_r$	-	Ratio of two spectral absorption functions
f	1/s	Temporal laser fluence profile

F_0	mJ/mm^2	Laser fluence
h	J·s	Planck's constant
H_{ref}	J/mol	Reference molar enthalpy of evaporation
ΔH_v	J/mol	Molar enthalpy of evaporation
$I_{b,\lambda}$	W/(sr·m)	Spectral blackbody intensity
J_λ	-	Spectral incandescence intensity
k_λ	-	Imaginary component of the complex index of refraction
k_B	$(m^2 \cdot kg)/(s^2 \cdot K)$	Boltzmann's constant
Kn	-	Knudsen number
L	nm	Length scale
m_{evap}	kg	Mass of evaporated species
m_g	kg	Mass of the gas molecule
m_p	kg	Mass of the nanoparticle
m_v	kg	Molar mass of the evaporated species
$\mathbf{m}_\lambda$	-	Complex index of refraction
n_λ	-	Real component of the complex index of refraction
n_g	$molecules/m^3$	Molecular number density of the gas
n_v	$molecules/m^3$	Molecular number density of the evaporated species
N_A	molecules/mol	Avogadro constant
N_g''	$molecules/(m^2 \cdot s)$	Molecular number flux of the gas
N_p	-	Number of monomers
N_v''	$molecules/(m^2 \cdot s)$	Molecular number flux of the evaporated species
$p(\cdot)$	-	Probability density function

$p(\mathbf{b})$	-	Evidence
$p(\mathbf{b}\|\mathbf{x})$, $p(\mathbf{b}\|\mathbf{x},\boldsymbol{\theta})$	-	Likelihood, Joint likelihood
$p(\mathbf{x}\|\mathbf{b})$, $p(\mathbf{x},\boldsymbol{\theta}\|\mathbf{b})$	-	Posterior, Joint posterior distribution
p_g	Pa	Gas pressure
$p_{pr}(\mathbf{x})$	-	Prior distribution
p_{ref}	Pa	Reference pressure
p_v	Pa	Vapour pressure of the evaporated species
$p_{v,o}$	Pa	Vapour pressure of the bulk material
q_{laser}	W	Rate of laser absorption
q_{cond}	W	Rate of conduction heat transfer
q_{evap}	W	Rate of evaporation heat transfer
$Q_{abs,\lambda}$	-	Spectral absorption efficiency
$Q_{ext,\lambda}$	-	Spectral extinction efficiency
$Q_{abs,\lambda}$	-	Spectral scattering efficiency
R	J/(mol·K)	Universal gas constant
R_s	J/(kg·K)	Specific gas constant
t	ns	time
T	K	Temperature
T_b	K	Boiling temperature
T_{cr}	K	Critical temperature
$T_{p,eff}$	K	Effective nanoparticle temperature
T_m	K	Melting temperature
T_g	K	Gas temperature

T_p	K	Nanoparticle temperature
T_{peak}	K	Nanoparticle peak temperature
T_{ref}	K	Reference temperature
$\mathbf{u}$	-	Relative refractive index
U, $U_{internal}$	J	Internal energy
x_p	-	Size parameter
$\mathbf{x}$	-	Inferred parameters

Greek characters

Symbol	Unit	Definition
α	-	Thermal accommodation coefficient (TAC)
β	-	Evaporation coefficient
γ_s	N/m	Surface tension
$\boldsymbol{\varepsilon}_\lambda$	-	Complex dielectric function
$\boldsymbol{\varepsilon}_{I,\lambda}$	-	Real component of dielectric function
$\boldsymbol{\varepsilon}_{II,\lambda}$	-	Imaginary component of dielectric function
ζ_{rot}	-	Rotational degrees-of-freedom
$\boldsymbol{\theta}$	-	Nuisance parameters
λ	nm	Wavelength
λ_{laser}	nm	Laser Wavelength
λ_{MFP}	nm	Mean free path

Λ	-	Intensity scaling factor (ISF)
μ	-	Reduced mass
μ	-	Mean of a normal distribution
μ_g	-	Geometric mean of a lognormal distribution
ξ_s	-	Riccati-Bessel function of order s
ρ	kg/m^3	Density
σ	-	Standard deviation of a normal distribution
σ_g	-	Geometric standard deviation of a lognormal distribution
ψ_s	-	Riccati-Bessel function of order s

Common superscripts and subscripts

Subscript	Definition
eff	effective
g	Gas
i, j, k	Indices
p	Nanoparticle
ref	reference
v	vapour

Superscript	Definition
exp	Experimental
mod	Modelled

Abbreviations

Abbreviation	Definition
AAC	Aerodynamic aerosol classifiers
DDA	Discrete dipole approximation
DMA	Differential mobility analyzer
DLS	Dynamic light scattering
ICE	Integrated cooling and electronics
ISF	Intensity scaling factor
LII	Laser-induced incandescence
MAP	Maximum a posteriori
MD	Molecular dynamics
MLE	Maximum likelihood estimate
NRC	National Research Council
pdf	Probability density function
PMT	Photomultiplier tube
PRF	Pulse repetition frequency
QoI	Quantities-of-interest
TAC	Thermal accommodation coefficient
TEM	Transmission electron microscopy
TiRe-LII	Time-resolved laser-induced incandescence
RDG-FA	Rayleigh-Debye-Gans fractal aggregate
UV-Vis	Ultra-violet visible

Chapter 1

Introduction to time-resolved laser-induced incandescence

This chapter introduces time-resolved laser-induced incandescence (TiRe-LII), a diagnostic for characterizing aerosols of nanoparticles, and compares it to alternative diagnostics methods. A literature review is presented to provide relevant background knowledge of the diagnostic. The chapter concludes by summarizing the overarching goal of this thesis work and the structure to which it is presented.

1.1 Motivation

The impact of suspended particulate matter in the air on human health is strongly size-dependent. For example, Environment Canada has classified suspended particles of sizes PM_{10} (particulate matter, PM) of diameter 10 μm or less as toxic [1]. Particles may enter the atmosphere through natural sources such as forest fires or windblown soil and anthropogenically through mechanical combustion processes or industrial activities such as welding [2]. These issues motivate significant ongoing efforts to develop measurement methods that help determine compliance with ambient air quality standards for suspended particles [3].

Nanoparticles also have many benefits [4]. In particular, metal nanoparticles are increasingly used in a wide range of engineering and science disciplines due to their unique and versatile size-dependent properties. In biomedicine, for example, gold and iron oxide nanoparticles are used for drug and gene delivery, and protein detection due to their biocompatibility [5,6]. They have also been used as optical sensors, catalysts, and UV filters owing to their tunable plasmonic properties, large surface area, and high refractive indices [7,8]. Metal nanoparticles are also useful for

pharmaceutical inhalation aerosols for pulmonary drug delivery [9]. Such benefits have contributed to the rapidly growing field of aerosol nanotechnology [10].

There is a need to measure suspended particles both to assess their impact on the environment and human health and their regulatory compliance, and to characterize the properties of engineered nanoparticle [3,11]. Although there are currently a range of *ex situ* techniques such as transmission electron microscopy (TEM) and dynamic light scattering (DLS)[1] that can be used to characterize these particles, they disallow the temporal and spatial resolution needed for many applications and inevitably cause system perturbations due to the nature of particle sampling required for such methods. There are *in situ* instruments such as differential mobility analyzers (DMA) [11] or aerodynamic aerosol classifiers (AAC) [12] available, but these methods have inaccuracies in size determination and also pose certain limitations. In the case of the DMA, since particles are characterized based on their electrical mobility, the assumption of singly charged particles introduces inaccuracies in particle sizing for aerosols containing particles that are multiply charged [11]. In the case of the AAC, particles are sized based on their relaxation time: the lower limit of the method is sensitive to diffusion losses and achievable rotational speeds, while the upper limit is sensitive to particle impaction [12]. In addition to these limitations, these methods can be considered "semi" *in situ* as sampling requires the aerosols to flow into the equipment for analysis.

Optical diagnostics present an alternative methodology for truly *in situ* measurements of properties of suspended particles. Time-resolved laser-induced incandescence (TiRe-LII) has become one of the most prevalent optical diagnostics as it is capable of making both *in situ*, and temporally- and spatially-resolved nanoparticle size measurements as well as other characteristics such as chemical composition [13] and thermophysical properties [14]. It can be applied to

[1] DLS can be considered *in situ* when characterizing nanoparticles suspended in a liquid solvent.

environmental air quality measurements to improve the resolution of the averaging time for total suspended particulates (TSP) measurements [15] and in the industry (where most nanoparticles are produced in the gas phase [16], particularly through flame synthesis [17]) for real-time online monitoring of the fabrication process.

TiRe-LII was initially conceived as a combustion diagnostic to study soot formation [18–23] and has quickly grown in its application to characterize other gas-borne nanoparticles containing metals and metalloids [24–29]. In this technique, the nanoparticles in a probe volume of aerosol are heated to incandescent temperatures with a laser pulse and then return to the motive gas temperature through conductive, evaporative, and radiative cooling. Spectral incandescence is measured throughout the process, usually at several wavelengths, using photomultiplier tubes (PMTs) equipped with narrow bandpass filters. A schematic of the process is shown in Figure 1-1. The observed incandescence is a thermal phenomenon resulting from the emission of electromagnetic radiation from the hot particle due to its high temperature. Since the heat transfer processes governing nanoparticle cooling are size-dependent, the incandescent decay rate can be used to infer the size classes of the aerosolized nanoparticles. The inference is achieved by regressing either the measured incandescence or the pyrometrically-inferred temperature history to a model that consists of two coupled submodels: a spectroscopic submodel, which relates the observed spectral incandescence to the temperature and size distribution of the nanoparticles, and the heat transfer submodel that relates the temperature decay rate to the nanoparticle size distribution and other physical properties such as the conduction efficiency, defined by the thermal accommodation coefficient (TAC).

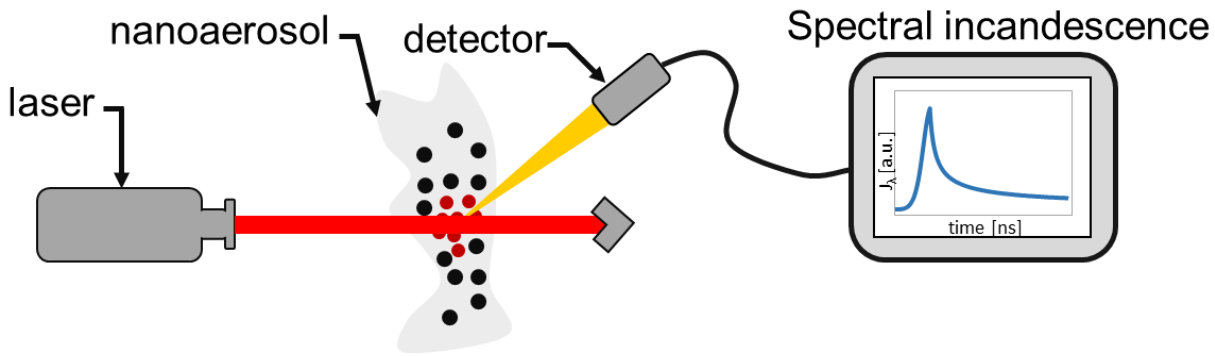

Figure 1-1: Schematic of time-resolved laser-induced incandescence

1.2 Background and literature review

1.2.1 TiRe-LII analysis on nanoparticles

It has long been known that particles in an aerosol interact with lasers and incandesce [30,31]; however, Weeks and Duley [18] first exploited this phenomenon to size aerosol particulates (carbon black and alumina) by proposing that the emitted signals could be related to particle size due to the size-dependent radiative emissions from the particles. Eckbreth extended the technique to combustion generated particulates [32], although with the aim of quantifying the amount of signal corruption introduced by LII during laser Raman diagnostics. Since then, TiRe-LII has become a standard technique for sizing and monitoring the volume fraction of soot particles produced from combustion processes [23,33–37].

In 2006, Schulz *et al*. [33] evaluated the understanding of the LII process on gas-borne soot nanoparticles by comparing several LII models. Most models accounted for particle heating by laser absorption and thermal equilibration by cooling mechanisms, including conduction, evaporation, sublimation, and radiative emission. They found that gaps in the understanding of the LII process led to wide variability in inferred nanoaerosol properties even under well-defined conditions. Michelsen *et al*. [38] conducted a similar evaluation the following year and also found considerable variability among competing models, although with a much better agreement than

the previous year. Both studies attributed the limited understanding to uncertainties both in the thermophysical and radiative properties of the soot nanoaerosol, some of which persist.

Vander Wal *et al*. [24] recognized the growing need to characterize gas-borne metal nanoparticles due to their growing importance in science and engineering [4,9,10]. They extended the TiRe-LII characterization technique to metal nanoparticles with measurements on tungsten (W), iron (Fe), molybdenum (Mo), and titanium (Ti) nanoparticles. The results showed that, although there are other laser-induced emissions (LIE) from the nanoparticles, only LII emissions persisted at longer cooling time scales and could be utilized for measuring nanoparticle mass concentration. Within the same year, Filipov *et al*. [39] showed, with experiments on silver (Ag) and titanium nitride (TiN) nanoparticles, that the LII signal can recover the size distribution of metal nanoparticles by numerically solving a Fredholm integral equation of the first kind and regressing it to the data. Murakami *et al*. [25] attempted to size Mo nanoparticles by employing the heat transfer model developed by Filipov *et al*.; however, there were some issues with this model [40], which included both Filipov *et al*. and Murakami *et al*. utilizing the conduction regime of the nanoparticle cooling to determine nanoparticle size but inherently implying a 100% conduction cooling efficiency (defined by the thermal accommodation coefficient (TAC)) between the nanoparticles and the motive gas, which further studies showed was unlikely [26,40].

Although Murakami *et al*. [25] utilized the conduction regime for sizing, they also studied the evaporation regime of the Mo nanoparticles by irradiating the nanoparticles with varying laser energies in an effort to investigate heat transfer processes at high temperatures [25]. They found that particle evaporation is the dominant mode of heat transfer in the first microseconds of particle cooling. Previously, Stephens *et al*. [13] utilized the vaporization information of the nanoparticles to distinguish between particle composition by monitoring the abrupt termination of elastically

scattered light and using pyrometry to find the temperature during the vaporization process. Neither Murakami *et al*. [25] nor Stephens *et al*. [13] accounted for the temperature-dependent thermophysical properties of the particles in the TiRe-LII model, which could alter evaporation results.

Starke *et al*. [41] carried out the sizing of Fe nanoparticles in a shock tube diluted with argon (Ar). They simultaneously inferred the TAC between the Fe nanoparticles and Ar motive gas as 0.33 by incorporating prior knowledge from *ex situ* size characterization of the nanoparticles. Kock *et al*. [26] and Eremin *et al*. [42] carried out more experiments on Fe nanoparticles aerosolized in different motive gases and attempted to infer the TACs while incorporating temperature-dependent thermophysical properties. The inferred results from both studies varied amongst the same nanoaerosol. Daun *et al*. approached the inference of TACs through molecular dynamics (MD) simulations for soot [43], nickel (Ni) [44,45], and Fe and Mo [46] nanoaerosols. However, Daun *et al*. reported a TAC of 0.5 for the Ni-Ar nanoaerosol, which is higher than expected when compared to TACs of other metal-gas aerosols [47]. Sipkens *et al*. [48,49] utilized the MD simulation approach to infer the TACs of various Fe and Si nanoaerosols with inferred results for the Fe nanoaerosols closely agreeing with experimentally-inferred results from the literature. Recently, Altman [50] proposed that the TACs for metal-gas systems are not constant but drop at high temperatures due to particle charging by thermionic emission.

Eremin *et al*. [51] reported size-dependent optical properties of soot and Fe nanoparticles by regressing the TiRe-LII model to the spectral incandescence signal from growing particles in a shock tube reactor. Sipkens *et al*.'s [29] analysis of experimental LII data of Fe, Ag and Mo nanoparticles showed excessive absorption by the Fe and Ag metal nanoparticles at the laser wavelength when the complex refractive index of these materials and the Rayleigh limit of Mie

theory were used to infer the spectral absorption cross-section compared to the value inferred from calorimetry based on the peak temperatures and laser fluence. However, when complex refractive indices were treated as constant across all detection wavelengths, as was done by Kock *et al*. [26], the peak temperatures of the nanoparticle plateaued at the boiling point of the metal and reasonable nanoaerosol properties were inferred. Menser *et al*. [28] observed, from LII experiments on silicon (Si) nanoparticles at high fluences, that the pyrometrically derived peak temperatures of the nanoparticles were higher than the boiling point of the metal. They attributed the high temperatures to superheating, which proposes that heat is being added to the nanoparticle by the laser faster than it can be removed by evaporation. They also acknowledged that there could be LII signal corruption of non-thermal origins such as anomalous incandescence behaviour, where there appears to be a sudden increase in incandescence signal due to some nanoparticle clusters undergoing micro explosions following thermal excitation [52], excessive absorption, and laser-induced Bremmstrahlung, where the observed signal is due to a vaporized plasma around the nanoparticle [53]. Earlier experiments by Vander Wal *et al*. [24] also suggested that there could be other laser-induced emission (LIE) sources that occurred during metal nanoparticle aerosol excitation including, excited-state emissions from the motive gas, electronically excited emissions from vaporized species, chemiluminescence from recombining vaporized species, particle photoluminescence, and particle plasmon resonance. Some of these phenomena were observed by Maffi *et al*. [54] with their study on titania (TiO_2) nanoparticles in which they found the incandescence signal to be corrupted by several narrowband spectral emissions at high fluences, and by Di Iuliis *et al*. [55], who observed signal corruption from fluorescence due to the metal oxide crystal structure. An anomalous cooling phenomenon, where the nanoparticle appears to cool faster than predicted by the LII heat transfer submodel, has also been observed [29,56,57].

Talebi-Moghaddam *et al*. [58] further investigated the proposed Bremmstrahlung phenomenon with simulations of laser interaction with Si, Fe and Mo nanoparticles, which laid the theoretical framework for the phenomenon within the context of LII. Subsequently, they also attempted to account for excessive absorption by modifying the standard LII spectroscopic sub-model [59]. They realized that the Rayleigh approximation of Mie theory, which is commonly used to interpret LII signals, was invalid for most metal nanoparticles because the phase-shift criterion: $x_p|\mathbf{m}_\lambda| << 1$, was not usually satisfied, where x_p is the nanoparticle size parameter that compares the size of the nanoparticle to the wavelength of the electromagnetic wave and $\mathbf{m}_\lambda$ is the complex refractive index at the laser wavelength (λ = 1064 nm). Although the magnitude of excessive absorption was reduced after applying the full essence of the Mie theory, it was not eliminated for Fe nanoparticles. In the case of Ag nanoparticle, the phenomena remained particularly significant and was attributed to the fact that Ag nanoparticles should not heat up more than 100 K at the laser wavelength and fluence, suggesting that observed signals are due to non-incandescent emissions.

1.2.2 TiRe-LII signal detection

Early TiRe-LII studies were often qualitative experiments carried out at one detection wavelength [18]; however, the first quantitative experiments for sizing nanoparticles with one-colour[2] LII was carried out by Will *et al*. [60] where the ratio of the signal intensities at two time-instances was used to define a parameter that was directly related to particle size. In the following year, Roth and Filipov [34] inferred the size distribution of aerosolized nanoparticles by solving a Fredholm integral equation that modelled the TiRe-LII process and regressing it to normalized signals obtained at a single wavelength. Since incandescence is a broadband phenomenon similar to a blackbody distribution, data at one wavelength were single measurements on the broadband

[2] Generally, #-colour refers to the number, #, of detection wavelengths on an LII system.

spectrum [61,62]. Due to the uncertainties in calibration, the radiative properties of the nanoparticles, and TiRe-LII model parameters, measuring the incandescence at multiple wavelengths significantly increases the reliability of the measurement [61].

Consequently, two-colour LII was also developed to utilize information from more than one detection wavelength and reduce the influence of uncertainties. Flower [63] first performed two-colour pyrometry on soot formed in premixed flames to determine the temperature history of the nanoparticles and soot volume fraction. Many studies have subsequently applied two-colour pyrometry techniques due to the improved robustness it provides [21,26,36,51]. Consequently, experiments have been performed with three-colour [64], four-colour [65], and a streak camera (continuous broadband detector) [65] setups that provide even more information across the wavelength spectrum.

A constant calibration factor is usually applied to experimental data obtained from TiRe-LII detector setup to relate the detector signals to spectral incandescence for quantitative analysis. Calibration can be carried out indirectly or directly [66]. Indirect calibration involves comparing the LII inferred parameters of well-characterized particles to the values obtained from *ex situ* measurements [67]; the LII signals are then appropriately scaled so that LII results match *ex situ* measurements. Direct calibration involves measuring the spectral emission from a radiant source, with well known spectral radiance, and ensuring that the measured signal intensities at the detection wavelengths match that of the radiant source by scaling each signal accordingly [66,68]. The TiRe-LII system can be directly calibrated for absolute or relative sensitivity. Absolute sensitivity calibration requires knowing the absolute spectral intensity of the radiant source and scaling each detected signal to match the corresponding spectral intensity. However, an absolute sensitivity calibration is not required when particle volume fraction is not of interest, in which case

a relative sensitivity calibration is sufficient [68]. For a relative sensitivity calibration, only knowledge of the magnitude ratio of the intensities at the detection wavelengths, is required. The ratio of the LII signals at each detection wavelength is then scaled to match that of the radiant source.

Mansmann *et al*. [66] established a robust relative calibration procedure for the PMT detector system based on a relative calibration technique developed by Snelling *et al*. [68]. However, experimental results from work by Menser *et al*. [28] showed that there is a temporal variation in the calibration constant during the experiment. Sipkens *et al*.'s investigation [69] showed that polydispersity in the nanoparticle-size distribution is a potential cause of the observed temporal variation. Work by Liu *et al*. [70] supported their finding when they showed that accounting for the size distribution of the nanoaerosol is needed for accurate LII analysis.

1.3 Present work

Considering the uncertainty in the understanding of TiRe-LII parameters in the literature, the overarching goal of the present work is to further develop the TiRe-LII technique for metal nanoparticles by regressing the TiRe-LII model to the spectral incandescence data while solving for the absorption efficiencies of the nanoparticle using Mie theory, temperature-dependent properties, and accounting for the polydispersity of the nanoparticles, thereby improving existing TiRe-LII analysis techniques presented in the literature.

Anomalies that are currently present in LII literature are also investigated through TiRe-LII experiments on plasmonic nanoparticles that are not expected to heat up during the experiments. This work was carried out with experimental measurements on aerosols of Ni, Fe, Ag, and gold (Au) nanoparticles. For added experimental and analytical robustness that reduce the influence of uncertainties during analyses, a two-colour detector system obtained from the National Research

Council (NRC), was upgraded with an additional detection wavelength. All nanoparticles in this work were synthesized in-house through wet chemical synthesis procedures.

The rest of the thesis is organized as follows: Chapter 2 provides the theoretical framework for TiRe-LII modelling, consisting of the spectroscopic and heat transfer submodels. The spectroscopic model predicts the observed signal of a nanoparticle ensemble at a given temperature while taking into account the absorption and emission properties of the nanoparticle. The heat transfer model predicts the temperature profile of the nanoparticles by considering the energy balance of the system that includes laser heating and cooling by mostly conduction and evaporation. The radiative and thermodynamic properties of Ni and Fe nanoparticles are presented.

Chapter 3 describes the operation of the TiRe-LII apparatus with a detailed discussion of various system components. The aerosol generation process during the experiment is also detailed.

Chapter 4 describes the synthesis procedure of the nanocolloids used in this work and reports the results from *ex situ* measurements. The data collection procedure using the TiRe-LII apparatus is also described.

Chapter 5 presents TiRe-LII results on aerosols of Ni and Fe nanoparticles followed by an interpretation of the results. A detailed description of the TiRe-LII analysis procedure used in this work is described. Since Fe nanoparticles have been extensively studied in the literature, results from the Fe nanoparticle data analysis are compared to the literature.

Chapter 6 presents experimental results on aerosols of Ag and Au nanoparticles in an effort to isolate a proposed LII signal corruption proposed by Talebi-Moghaddam *et al*. [58]. A qualitative assessment of the experimental results is presented.

Chapter 7 provides conclusions of the analysis of the present work and recommends future work that can be explored.

Appendices are presented following the described research outcomes. A detailed description of the calibration procedure carried out for the TiRe-LII apparatus is described. The mathematical theory of the minimization schemes used for model analysis is also described, along with other supplemental information.

Chapter 2

Time-resolved laser-induced incandescence modelling

Accurate and robust inference of quantities-of-interest (QoIs) from TiRe-LII data requires accurate modelling of the physical processes that underlie the measurement. The overall theoretical framework is based on an energy and mass balance of the system [71] that considers the heat up of the nanoparticles by laser excitation and their cooling by various heat transfer processes [38], which is modelled by a heat transfer submodel that predicts the temperature history of the nanoparticle. A spectroscopic submodel then uses the instantaneous temperatures to predict the observed instantaneous incandescence signals. This chapter provides an overview of the standard TiRe-LII model that is used in the literature.

2.1 Spectroscopic submodel

The spectroscopic submodel predicts the emitted spectral incandescence from the laser heated nanoparticles within an aerosol. For an optically thin, polydisperse nanoaerosol, the instantaneous spectral incandescence, $J_\lambda(t)$, emitted by the heated nanoparticles is given by [28]

$$J_\lambda(t) = C_\lambda \Lambda \int_0^\infty p(d_\mathrm{p}) \frac{\pi d_\mathrm{p}^2}{4} Q_{\mathrm{abs},\lambda}(d_\mathrm{p}, \mathbf{m}_\lambda) I_{\mathrm{b},\lambda}\left[T_\mathrm{p}(t, d_\mathrm{p})\right] d(d_\mathrm{p}), \tag{2.1}$$

where C_λ is the calibration constant applied to the LII channel equipped with a bandpass filter centred at a wavelength λ (*cf.* Appendix A), Λ is the intensity scaling factor (ISF) that accounts for the volume fraction of nanoparticles within nanoaerosol [28,69], d_p is the nanoparticle size, $p(d_\mathrm{p})$ is the probability density function (pdf) of the particle size distribution, $\mathbf{m}_\lambda$, is the complex index of refraction of the nanoparticle particle material at wavelength λ, $Q_{\mathrm{abs},\lambda}$, is the spectral absorption

efficiency, and $I_{b,\lambda}$ is the blackbody spectral intensity emitted at the nanoparticle temperature, $T_p(t,d_p)$. The absorption cross-section of the nanoparticle is defined as

$$C_{abs,\lambda} = \frac{\pi d_p^2}{4} Q_{abs,\lambda}\left(d_p, \mathbf{m}_\lambda\right). \tag{2.2}$$

Although aerosols are often polydisperse, for a sufficiently narrow pdf, a monodisperse approximation can be used to simplify Eq. (2.1) to

$$J_\lambda(t) = C_\lambda \Lambda \frac{\pi d_p^2}{4} Q_{abs,\lambda}\left(d_p, \mathbf{m}_\lambda\right) I_{b,\lambda}\left[T_p\left(t, d_p\right)\right]. \tag{2.3}$$

The blackbody intensity, $I_{b,\lambda}$, of the nanoparticles, surrounded by a non-participating gas medium, is given by

$$I_{b,\lambda} = \frac{2\pi h c_0^2}{\lambda^5\left[\exp\left(\frac{hc_0}{k_B \lambda T_p}\right) - 1\right]}, \tag{2.4}$$

where h is Planck's constant, c_0 is the speed of light in a vacuum, λ is the wavelength at which the intensity is determined, k_B is Boltzmann constant, and T_p is the temperature of the nanoparticle.

In the case of spherical particles, the spectral absorption efficiency, is obtained from the exact solution provided by Mie theory [72], which is given by the following equations:

From energy conservation,

$$Q_{abs,\lambda}^{Mie} = Q_{ext,\lambda}^{Mie} - Q_{sca,\lambda}^{Mie}, \tag{2.5}$$

where $Q_{abs,\lambda}^{Mie}$ is the Mie predicted spectral absorption efficiency, and $Q_{ext,\lambda}^{Mie}$ and $Q_{sca,\lambda}^{Mie}$ are the spectral extinction and scattering efficiencies, respectively, given by

$$Q_{ext,\lambda}^{Mie} = \frac{2}{x_p^2}\sum_{s=1}^{\infty}(2s+1)\,\mathrm{Re}\left(a_s + b_s\right) \tag{2.6}$$

$$Q_{\mathrm{sca},\lambda}^{\mathrm{Mie}} = \frac{2}{x_{\mathrm{p}}^2}\sum_{s=1}^{\infty}(2s+1)\left(|a_s|^2+|b_s|^2\right), \tag{2.7}$$

where a_s and b_s are the scattering coefficients given by

$$\begin{aligned} a_s &= \frac{\mathbf{u}\psi_s(\mathbf{u}x_{\mathrm{p}})\psi_s'(x_{\mathrm{p}}) - \psi_s(x_{\mathrm{p}})\psi_s'(\mathbf{u}x_{\mathrm{p}})}{\mathbf{u}\psi_s(\mathbf{u}x_{\mathrm{p}})\xi_s'(x_{\mathrm{p}}) - \psi_s(x_{\mathrm{p}})\xi_s'(\mathbf{u}x_{\mathrm{p}})} \\ b_s &= \frac{\psi_s(\mathbf{u}x_{\mathrm{p}})\psi_s'(x_{\mathrm{p}}) - \mathbf{u}\psi_s(x_{\mathrm{p}})\psi_s'(\mathbf{u}x_{\mathrm{p}})}{\psi_s(\mathbf{u}x_{\mathrm{p}})\xi_s'(x_{\mathrm{p}}) - \mathbf{u}\psi_s(x_{\mathrm{p}})\xi_s'(\mathbf{u}x_{\mathrm{p}})} \end{aligned}; \tag{2.8}$$

for a surrounding medium of gas, **u**, the relative refractive index, is equal to the complex refractive index, $\mathbf{m}_\lambda$, of the nanoparticle where $\mathbf{m}_\lambda = n_\lambda + ik_\lambda$, where n and k are the real and complex indices of refraction; $x_{\mathrm{p}} = \pi d_{\mathrm{p}}/\lambda$ is the size parameter, and ψ_s and ξ_s are Riccati-Bessel functions of order s.

However, it is common in LII literature [22,29] to approximate the spectral absorption efficiency predicted by the exact solution provided by Mie theory with the Rayleigh approximation when $|\mathbf{m}_\lambda|x_{\mathrm{p}} << 1$ (phase-shift parameter criterion) and $x_{\mathrm{p}} << 1$ (size parameter criterion) [72,73].

The Rayleigh approximation is given by

$$Q_{\mathrm{abs},\lambda}^{\mathrm{Rayliegh}} = 4x_{\mathrm{p}}E(\mathbf{m}_\lambda), \tag{2.9}$$

where $E(\mathbf{m}_\lambda)$ is the spectral absorption function given by

$$E(\mathbf{m}_\lambda) = \mathrm{Im}\left(\frac{\mathbf{m}_\lambda^2 - 1}{\mathbf{m}_\lambda^2 + 2}\right) = \frac{6n_\lambda k_\lambda}{\left(n_\lambda^2 - k_\lambda^2 + 2\right)^2 + 4n_\lambda^2 k_\lambda^2}. \tag{2.10}$$

Drude theory can be used to estimate the bulk dielectric properties of metals, from which $\mathbf{m}_\lambda$ can be determined [28,29,65,74]. In Drude theory, the metal is modelled as a plasma of free electrons that collide with massive background ions as they are accelerated and decelerated by an electromagnetic wave [72]. Drude theory is generally more accurate for estimating the optical

properties of liquid metals compared to solid metals because there is no electron scattering from lattice boundaries since the electronic band structure above the Fermi level is absent in the liquid state, and there are no surface roughness and contamination effects [75]. Although the theory works well for some metals, for example, copper (Cu), liquid Si (which metallizes upon melting) [28,65], and Ag [29], it does not apply to transition metals such as Ni and Fe because the d-band electrons cross the Fermi-level surface and overlap the conduction band [75], and, consequently, the optical properties in the wavelength spectrum important to LII are due to both intraband and interband transitions [74].

Instead, the refractive indices are obtained from ellipsometry results in the literature. For both Ni and Fe nanoparticles, these properties are obtained from Krishnan *et al*. [76], who determined the optical conductivity and real part of the dielectric property of the metals through laser ellipsometric measurements on electromagnetically levitated liquid metals in a vacuum. Figure 2-1 presents these results and the corresponding $E(\mathbf{m}_\lambda)$ values. Results by Miller [74] and Shvarev *et al*. [77] were also considered to show the extent of variability of the optical properties in the literature. The refractive indices of solid Ni were taken from Ordal *et al*. [78].

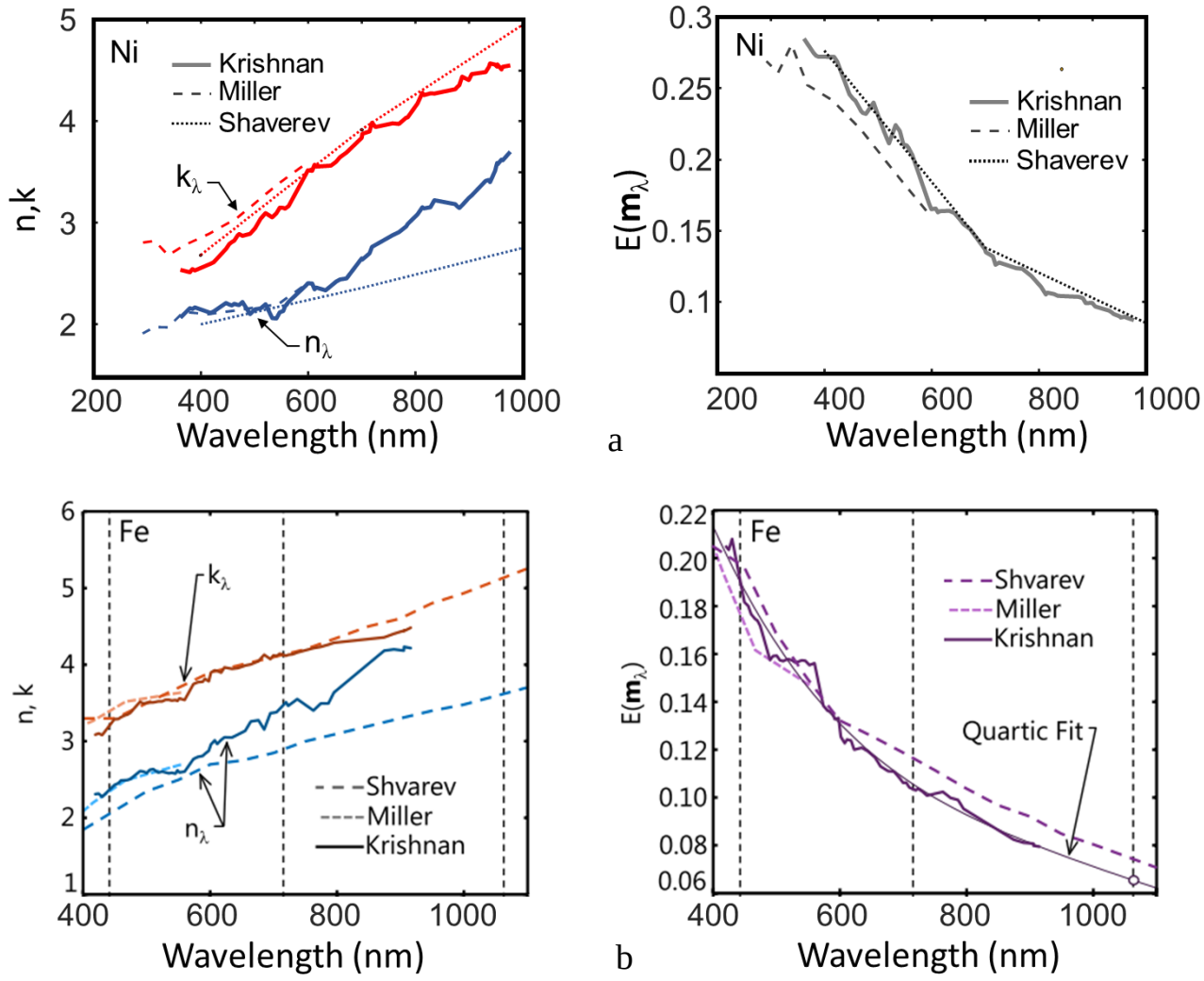

Figure 2-1: Refractive indices of liquid (a)(left) Ni and (b)(left) Fe [29] and corresponding absorption function (a)(right) and (b)(right) [29]. Refer to Appendix E.1 for the relationship between optical conductivity, dielectric constants and refractive indices.

The Rayleigh approximation is usually valid for soot nanoparticles, since the size parameter and phase shift criteria are usually satisfied. However, this is not generally the case for metal nanoparticles because the phase-shift criterion is not usually satisfied [59]. Figure 2-2 shows that the Rayleigh approximation is invalid for liquid Ni particles greater than 40 nm. The Mie theory provides more accurate estimates of the absorption efficiencies.

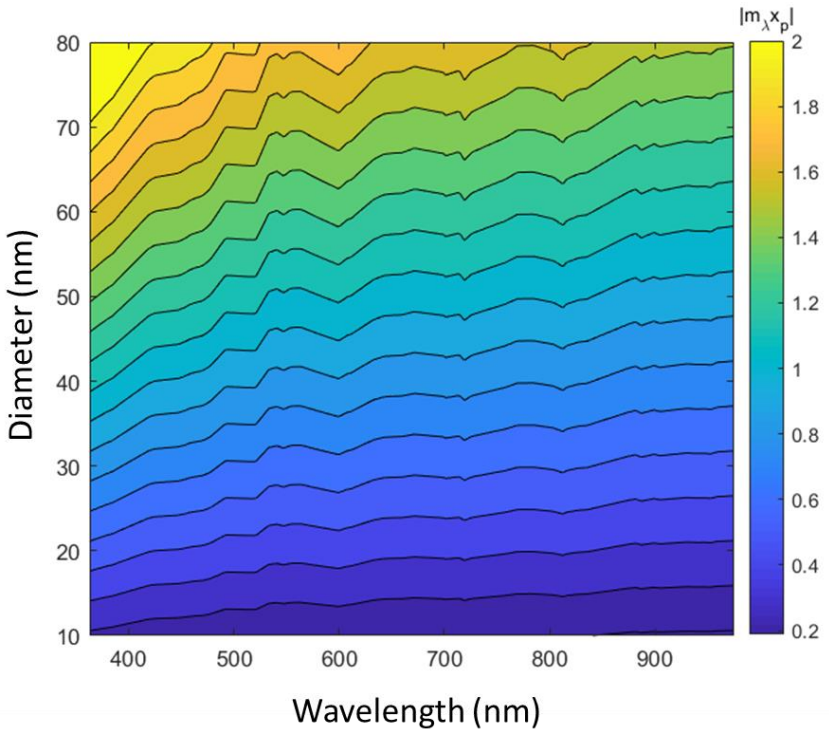

Figure 2-2: Phase-shift parameter of liquid Ni nanoparticles.

Absorption efficiencies have been presented with the assumption that the nanoparticles within the probe volume exist as spherical monomers, which is sometimes not the case. The monomers often assemble into aggregates, in which case other models such as Rayleigh-Debye Gans Fractal Aggregate theory (RDG-FA), or Discrete Dipole Approximation (DDA) need to be employed to estimate $Q_{\mathrm{abs},\lambda}$. RDG-FA determines the absorption efficiency by assuming the aggregates are made of identical and independent scattering spheres and the total scattered amplitude is proportional to the number of monomers, N_{p}, that make up the aggregate and the total scattering intensity is proportional to N_{p}^2 [73,79]. DDA discretizes the aggregates into point dipoles and solves Maxwell's equations for the scattering problem in a local field [80].

2.1.1 Optical pyrometry

During laser heating, the nanoparticles in the aerosol are at different temperatures depending on their size. The pdf of the size distribution, $p(d_p)$, which depends on the synthesis procedure of the nanoparticles [81,82], is usually approximated as narrow, allowing for an "effective" temperature, $T_{p,eff}$, of the nanoparticle ensemble to be computed from the incandescence signals through optical pyrometry. The effective temperature is meant to provide an indication of the instantaneous internal energy of the nanoparticles within the probe volume. However, polydispersity can complicate the interpretation of the effective temperature since the pdf representing the temperature distribution of the particles at any instant becomes wider with increasing polydispersity (*cf.* §2.2.2). Nevertheless, many studies [21,29,41,51] have utilized pyrometry for particle characterization by fitting the modelled temperature to the experimentally determined pyrometric temperature. By measuring incandescence signals at one or more wavelengths, $T_{p,eff}$ as well as, $\Lambda_{p,eff}$, the effective ISF, can be determined by solving the non-linear minimization problem,

$$\begin{bmatrix} T_{p,eff} \\ \Lambda_{p,eff} \end{bmatrix} = \underset{T,\Lambda}{\arg\min} \left\{ \left\| \begin{matrix} J_{\lambda_1}^{exp} - J_{\lambda_1}^{mod} \\ \vdots \\ J_{\lambda_w}^{exp} - J_{\lambda_w}^{mod} \end{matrix} \right\|_2^2 \right\}, \tag{2.11}$$

where $J_{\lambda,w}^{exp}$ is the experimentally measured incandescence at the w^{th} wavelength channel and $J_{\lambda,w}^{mod}$ is the modelled incandescence signal at the w^{th} wavelength given by Eq. (2.1) or Eq. (2.3); all variables are time-dependent. When pairs of wavelength incandescence signals are used in the Rayleigh limit, the minimization problem can be simplified by a closed-form solution provided by two-colour ratio pyrometry, which involves taking the ratio of the signals at the two wavelengths

and solving for the time-dependent temperature [59]. By doing this and invoking Wien's[3] approximation (where the exponential term in Eq. (2.4), $\exp(hc_0/k_B\lambda T) >> 1$), the effective temperature is given by

$$T_{\mathrm{p,eff}} = \frac{hc_0}{k_\mathrm{B}}\left(\frac{1}{\lambda_2}-\frac{1}{\lambda_1}\right)\left[\ln\left(\frac{J_{\lambda,1}}{J_{\lambda,2}}\frac{E\left(\mathbf{m}_{\lambda,2}\right)}{E\left(\mathbf{m}_{\lambda,1}\right)}\left(\frac{\lambda_1}{\lambda_2}\right)^6\right)\right]^{-1}. \tag{2.12}$$

Although the ratio of the emission efficiencies, $E(\mathbf{m})_r = E(\mathbf{m}_{\lambda,1})/E(\mathbf{m}_{\lambda,2})$, can be determined from the ellipsometry-derived complex index of refraction or Drude theory, some TiRe-LII studies have obtained practical results with $E(\mathbf{m})_r$ of unity or close to unity of Fe nanoparticles [26,29,83]. Employing Rayleigh approximation for pyrometry to interpret data from metal nanoparticles introduces modelling error further complicates results in a polydisperse nanoaerosol (*cf.* §2.2.2).

Using $Q_{\mathrm{abs},\lambda}^{\mathrm{Mie}}$ to find the effective temperature requires knowledge of the nanoparticle size distribution; in this case, an effective diameter, d_{eff}, which is commonly defined as the geometric mean of the polydisperse aerosol and best represents the diameter of an equivalent monodisperse aerosol approximation [33], can be used. Information for d_{eff} will have to be informed by prior *ex situ* characterization or chosen so that the effective temperature corresponds to a representative thermodynamic temperature of the ensemble [59].

2.2 Heat transfer submodel

The heat transfer submodel predicts the temperature history of the nanoparticle ensemble in the probe volume by an energy balance on a nanoparticle, schematically shown in Figure 2-3 and given by

[3] This approximation is accurate to within 1% for λT less than 3000 μm·K.

$$\dot{U}_{\text{internal}} = q_{\text{laser}}(t, d_{\text{p}}) - q_{\text{evap}}(T_{\text{p}}, d_{\text{p}}) - q_{\text{cond}}(T_{\text{p}}, d_{\text{p}}), \tag{2.13}$$

where $\dot{U}_{\text{internal}}$ is the rate of internal energy change by the nanoparticle, $q_{\text{laser}}(t, d_{\text{p}})$ is the time dependent laser energy absorbed by the nanoparticle, and $q_{\text{evap}}(t, d_{\text{p}})$ and $q_{\text{cond}}(t, d_{\text{p}})$ are energy loss from the nanoparticle due to evaporation and conduction, respectively; all energy transfer terms depend on nanoparticle diameter.

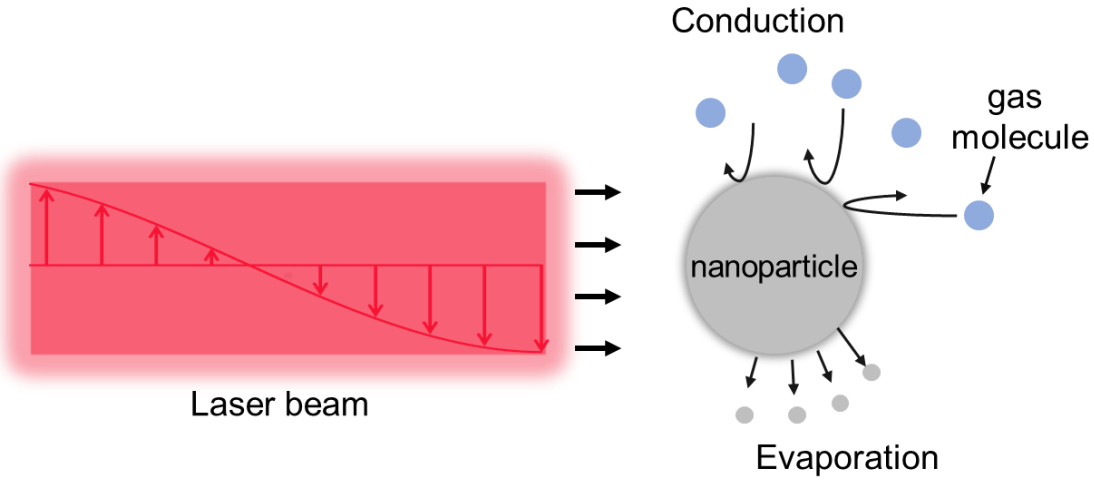

Figure 2-3: Schematic of the laser excitation and cooling process of the nanoparticle.

Other cooling mechanisms such as radiation[4], sublimation, thermionic emission, as well as other heating terms including, oxidation have been found to be orders of magnitudes less than those used in Eq. (2.13) (*cf.* Figure 2-4) [29,38]. During the heat transfer process, the nanoparticle dilates due to the temperature-dependent density. To account for the mass loss due to evaporation, Eq. (2.13) is solved simultaneously with a second differential [59],

$$\dot{m}_{\text{p}} \equiv -\dot{m}_{\text{evap}}\left(T_{\text{p}}, d_{\text{p}}\right), \tag{2.14}$$

i.e., the rate of change of nanoparticle's mass, $\dot{m}_{\text{p}}$, is due to the mass loss by evaporation, $\dot{m}_{\text{evap}}$.

[4] Although radiation is the phenomenon that allows the detection of incandescence, it is still significantly less than the presented heat transfer phenomena.

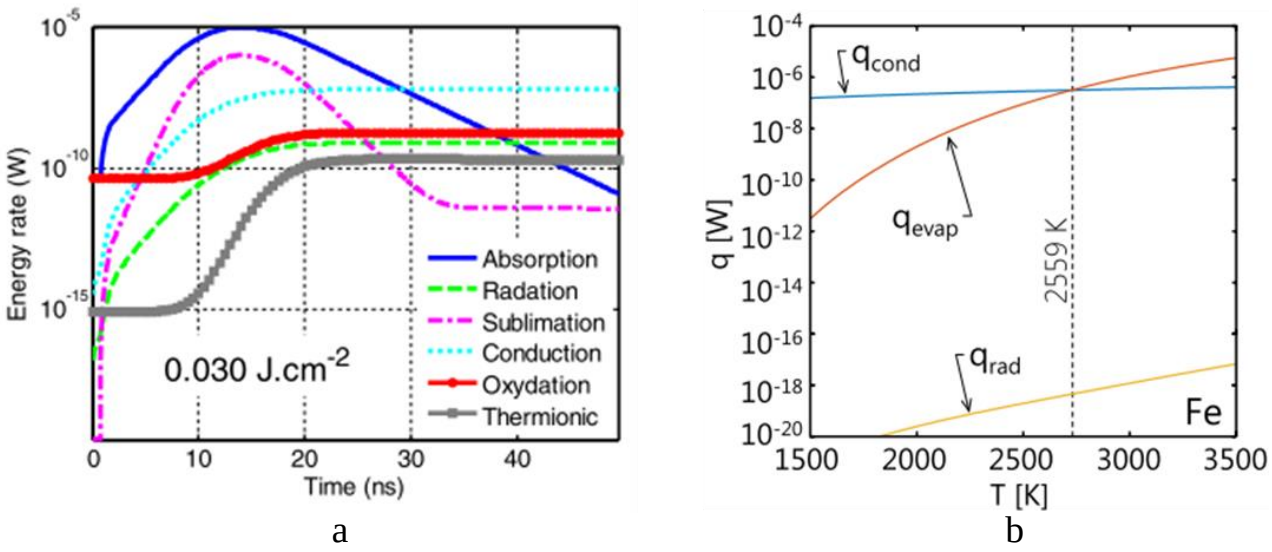

Figure 2-4: Plots comparing cooling mechanisms for (a) soot [84] and (b) iron nanoparticles [29].

The following sections provide in-depth modelling consideration of terms in Eq. (2.13) and Eq. (2.14).

2.2.1 Internal energy

The internal energy of the nanoparticles changes over time due to the rate at which energy is lost and gained by the nanoparticle over time as a result of the cooling and heating processes and is given by

$$\dot{U}_{\text{internal}} = c_{\text{p}}\left(T_{\text{p}}\right) m_{\text{p}}\left(T_{\text{p}}\right) \frac{d\left(T_{\text{p}}\left(t\right)\right)}{dt}, \tag{2.15}$$

where $m_{\text{p}}(T_{\text{p}})$ is the temperature-dependent mass of the nanoparticle given by

$$m_{\text{p}}\left(T_{\text{p}}\right) = \frac{\rho_{\text{p}}\left(T_{\text{p}}\right)\pi d_{\text{p}}^{3}}{6}, \tag{2.16}$$

and $c_{\text{p}}(T_{\text{p}})$, and $\rho_{\text{p}}(T_{\text{p}})$ are the temperature-dependent heat capacity and density of the nanoparticle of diameter, d_{p} at an instantaneous temperature $T_{\text{p}}(t)$ given in Table 2-1 for Ni and Fe.

Table 2-1: Density and specific heat of Ni and Fe nanoparticles.

Property	**Ni**	**Fe***
$\rho_p(T_p)$ [kg/m^3]	$T_p > T_m$: 8981.7 – 0.6441T$_p$ [85]	8171 – 0.64985T_p [85]
	$T_p < T_m$: 8900 [86]	
$c_p(T_p)$ [J/(kg·K)]	$T_p > T_m$: 747.15 [87,88]	835 [89]
	$T_p < T_m$: *cf.* Figure 2-5	

*all properties are as cited by [29].

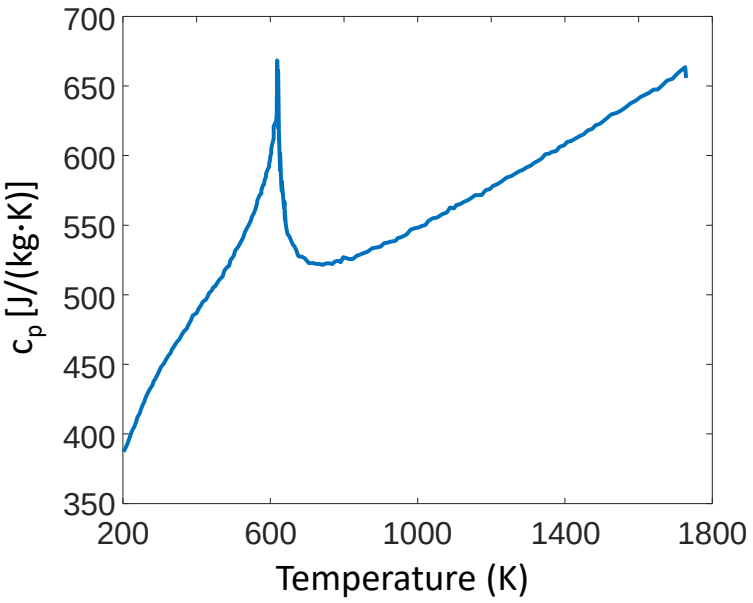

Figure 2-5: Temperature-dependent specific heat of Ni below 1700 K [89].

2.2.2 Laser energy absorption

The laser absorption term, $q_{laser}(t, d_p)$, adds energy to the nanoparticle due to the time dependent laser excitation and is given by

$$q_{laser}(t, d_p) = F_0 f(t) \frac{\pi d_p^2}{4} Q_{abs,\lambda_{laser}}(\mathbf{m}_\lambda, d_p), \tag{2.17}$$

where F_0 is the laser fluence[5], $f(t)$ is the laser temporal profile (typically a Gaussian distribution in time), $Q_{abs,\lambda laser,}$ is the absorption efficiency of the nanoparticle of diameter, $d_{p,}$ at the laser wavelength, λ_{laser}. The exact Mie solution or the Rayleigh approximation can be used to compute $Q_{abs,\lambda laser}$ depending on whether or not the phase-shift or size parameter criteria are satisfied [73].

When the laser heating model in Eq. (2.17) assumes the nanoparticle absorbs energy in the Rayleigh limit, $q_{laser}(t, d_p)$ is proportional to d_p^3, consequently, there is a volumetric heating of the nanoparticle with no temperature gradient, an assumption that is generally accepted in TiRe-LII modelling [90,91]. However, this can introduce some inaccuracies determining the temperature of metal nanoparticles in a polydisperse aerosol because the different size classes reach different peak temperatures, as determined from Mie theory (*cf.* Figure 2-6), but reach approximately identical temperatures when modelled in the Rayleigh regime [59]. This complicates the interpretation of the pyrometrically-inferred temperatures that employ the Rayleigh approximation.

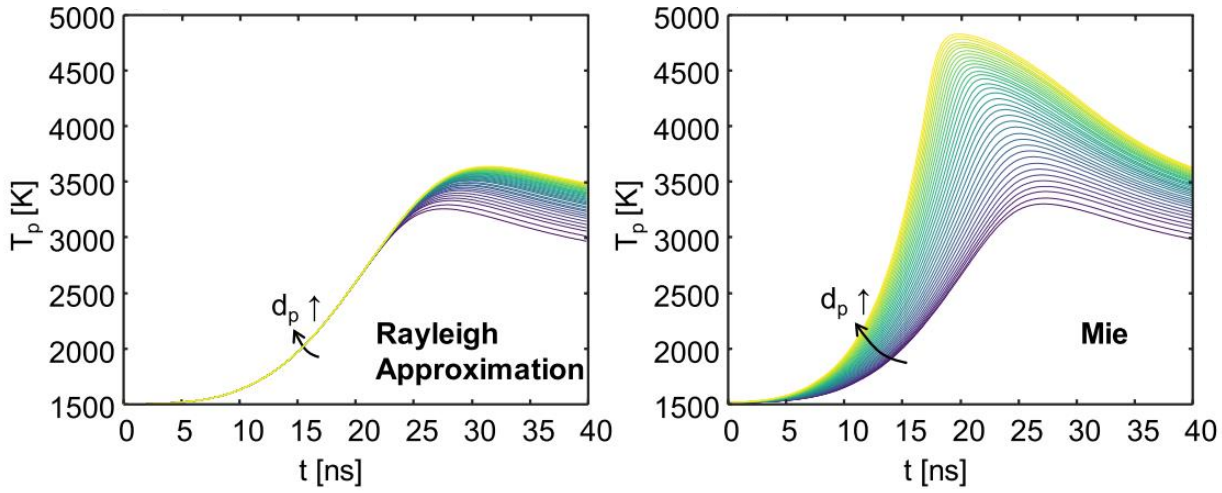

Figure 2-6: Simulated temperatures of Si nanoparticles obtained when absorption of the laser by nanoparticles is modelled with (a) Rayleigh approximation (b) Mie theory [59].

[5] Amount of energy from the laser per unit cross-sectional area.

2.2.3 Evaporative cooling

The evaporative cooling term, $q_{\text{evap}}(t,\ d_{\text{p}})$, removes energy from the nanoparticle through evaporative mass loss (*cf.* Figure 2-3). It is modelled as the product of the amount of energy required to evaporate a unit mass of the nanoparticle and the rate of mass change [71]

$$q_{\text{evap}}\left(T_{\text{p}}, d_{\text{p}}\right) = \frac{\Delta H_{\text{v}}\left(T\right)}{m_{\text{v}}} \frac{dm_{\text{p}}}{dt} \ , \tag{2.18}$$

where ΔH_{v} is the temperature-dependent molar enthalpy of evaporation found from Watson's equation [92],

$$\Delta H_{\text{v}} = H_{\text{ref}} \left[\frac{T_{\text{cr}} - T_{\text{p}}}{T_{\text{cr}} - T_{\text{ref}}} \right]^{0.38} \ , \tag{2.19}$$

and H_{ref} and T_{ref} are the molar enthalpy of evaporation and temperature of the nanoparticle, respectively, taken at a reference point of the saturated vapour, and T_{cr} is the critical temperature of the nanoparticle; m_{v} is the molar mass of the evaporated species, and dm_{p}/dt is the rate of mass change given by

$$\frac{dm_{\text{p}}}{dt} = \pi d_{\text{p}}^2 N_{\text{v}}^{''} \frac{m_{\text{v}}}{N_A} \ , \tag{2.20}$$

such that the mass loss is equal to the mass evaporated, and N_A is Avogadro's number. Transport occurs in the free molecular (Knudsen) regime because the size of the nanoparticle is much smaller than the evaporative mean free path of the evaporated species (*cf.* Refs. [93–95]). Consequently, $N_{\text{v}}^{''}$ is the molecular flux given by [96]

$$N_{\text{v}}^{''} = \frac{1}{4} \beta n_{\text{v}} c_{\text{v}} = \frac{1}{4} \beta \frac{p_{\text{v}}}{k_{\text{B}} T_{\text{p}}} \sqrt{\frac{8 k_{\text{B}} T_{\text{p}}}{\pi m_{\text{v}}}} \ , \tag{2.21}$$

where β is the evaporation coefficient that defines the fraction of evaporative species that condense after a collision [95], which is commonly taken to be unity [38][6] [29], n_v and c_v are the molecular number density and the mean thermal speed of the evaporative species respectively, k_B is the Boltzmann constant and p_v is the vapour pressure of the evaporative species. Assuming quasi-equilibrium of the nanoparticle at the liquid-vapour interface, p_v, can be determined by the Clausius-Clapeyron equation [97,98]

$$p_v = p_{ref} \exp\left[\frac{\Delta H_v \left(T_p - T_{ref}\right)}{R T_p T_{ref}}\right], \tag{2.22}$$

where R is the universal gas constant, p_{ref} and T_{ref} are the pressure and temperature, respectively, taken at a reference point for the saturated vapour. However, some uncertainties have been reported when using the Clausius-Clapeyron equation to model the vapour pressure as a function of temperature [28]. The vapour pressure needs to be adjusted to account for the increase in surface energy induced by the curvature of the nanoparticle. This is accounted for by the Kelvin equation [99]

$$p_v = p_{v,o} \exp\left[\frac{4\gamma_s\left(T_p\right)}{d_p \rho\left(T_p\right) R_s T_p}\right] \tag{2.23}$$

where $p_{v,o}$ is the unadjusted vapour pressure of Eq. (2.22), $\gamma_s(T_p)$ is the temperature-dependent surface tension of the nanoparticle, and R_s is the specific gas constant of the surrounding gas.

Having defined the evaporation model, $\dot{m}_{evap}(T_p, d_p)$ from Eq. (2.14) can now be defined as

$$\dot{m}_{evap}(T_p, d_p) = m_v \frac{q_{evap}\ \ t, T_p}{\Delta H_v}\ , \tag{2.24}$$

[6] This reference referred to the evaporation coefficient as a mass accommodation coefficient.

which connects the change in mass to the mass loss from evaporation. The instantaneous diameter is solved for by rearranging Eq. (2.16) for d_p.

The values of all evaporative related cooling for both Ni and Fe nanoparticles are listed in Table 2-2 below.

Table 2-2: Evaporation model related properties of Ni and Fe.

Property	**Ni**	**Fe***
T_{ref} [K]	3186.15[86]	3134 [100]
H_{ref} [J/mol]	378×10^6 [101]	340×10^6 [100]
P_{ref} [Pa]	101325	101325
T_{cr} [K]	3186.15 [102]	9340 [102]
$\gamma_s(T_p)$ [N/m]	$(1826 - 0.346(T_p - T_m)).(10^{-3})$ [103]	$1.826 - (T_p - T_m).(0.35).(10^{-3})$ [104]
m_v [kg]	9.7462×10^{-26}	9.2733×10^{-26}

*all properties are as cited by [29].

2.2.4 Conductive cooling

The conductive cooling term, $q_{cond}(t, d_p)$, models the removal of energy from the nanoparticle through motive gas molecule collisions with the nanoparticle (*cf.* Figure 2-3); consequently, at this scale, the conductive cooling is modelled in the free molecular (Knudsen) regime. In the Knudsen regime, the nanoparticle, with a characteristic length, L, taken as the radius of the nanoparticle, is much smaller than the conductive mean free path, λ_{MFP} (*cf.* Appendix D.1), of the motive gas, i.e., the Knudsen number, $Kn = \lambda_{MFP}/L >> 1$ [91], in which case the gas molecules conduct heat from the nanoparticle by colliding and scattering off the surface of the nanoparticle. (When $Kn \approx 1$, or $Kn << 1$, conduction occurs in the transition and continuum regime, respectively [91]). A rigorous thermodynamic derivation of the free molecular conduction model is provided by Filippov and Rosner [79] and further detailed by Liu *et al*. [91] and is presented as

$$q_{cond}\ T_p(t), d_p\ = \alpha\pi d_p^2 N_g^{''}\left[2k_B\ T_p(t) - T_g\ + U\ T_p\ - U\ T_g\ \right], \tag{2.25}$$

where k_B is Boltzmann's constant, $T_p(t)$ is the time-dependent nanoparticle temperature, T_g is the temperature of the motive gas, d_p is the diameter of the nanoparticle, $U(T)$ is the internal energy of the incident and scattered gas molecule, α is the thermal accommodation coefficient that defines the efficiency of energy transfer when an incident gas molecule scatters from the heated nanoparticle, and $N_g^{''}$ is the molecular number flux of the ambient gas molecules given by

$$N_g^{''} = \frac{1}{4} n_g c_g = \frac{1}{4} \frac{p_g}{k_B T_g} \sqrt{\frac{8 k_B T_g}{\pi m_g}}, \tag{2.26}$$

where n_g and c_g are the molecular number density and the mean thermal speed of the motive gas molecules, respectively, k_B is the Boltzmann constant and p_g is the partial pressure of the motive gas.

The quantity $[2k_B(T_p(t) - T_g) + U(T_p) - U(T_g)]$ in Eq. (2.25) is the maximum average energy that can be transferred from a heated nanoparticle with energy, E_o, to an incident gas molecule with energy, E_i, [91], i.e. $\langle E_o - E_i \rangle_{max}$, that is adjusted by α, which takes into account the imperfect energy transfer between the nanoparticle surface and a scattering gas molecule. Daun [43] calculated this term via molecular dynamic (MD) simulations, noting that the gas molecule can accommodate the energy of the nanoparticle in the normal-translational and tangential-translational directions, as well as in its rotational degrees-of-freedom (*cf.* Figure 2-7); the total maximum energy transfer is then the sum of the maximum energy transfer accommodated into each of the three modes. The normal- and tangential-translational modes both maximally accommodate $k_B(T_p - T_g)$ and the rotational mode maximally accommodates $(\zeta_{rot}/2)k_B(T_p - T_g)$, where ζ_{rot} is the number of rotational degrees-of-freedom with $\zeta_{rot} = 0$ for monoatomic gases such as Ar, He and Ne; $\zeta_{rot} = 2$ for linear polyatomic gases such as CO, N_2, and CO_2; and $\zeta_{rot} = 3$ for non-linear polyatomic gases such as CH_4 and C_2H_6.

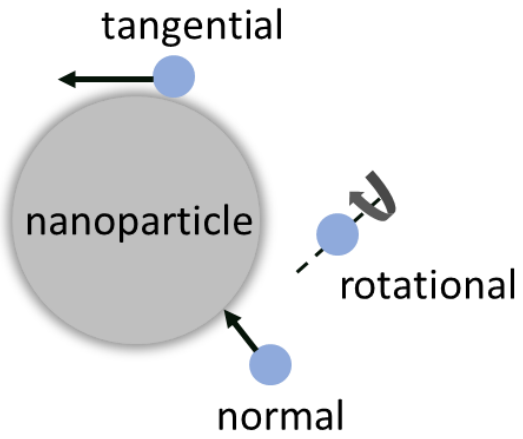

Figure 2-7: Gas molecules collisional degrees-of-freedom (DOF).

Although the gas molecules have an internal vibrational degree-of-freedom, the molecules were modelled as rigid bodies, and MD results showed that the vibrational accommodation is indeed insignificant when the results closely agreed with experimental data in the absence of tuning or heuristics, as shown in Figure 2-8.

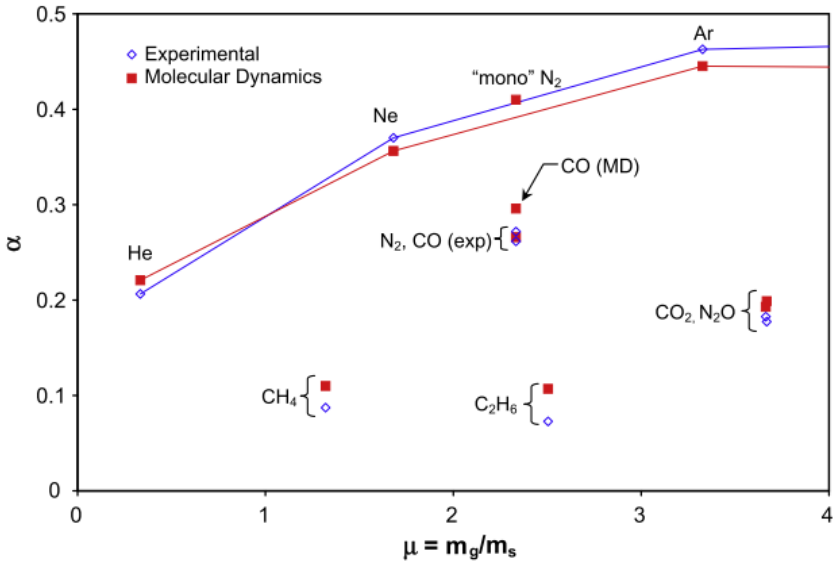

Figure 2-8: Molecular dynamics simulation results for the thermal accommodation coefficient of soot in different motive gases [43].

Note from Figure 2-8 that the general trend for the TACs shows an increase with specific mass, μ (the ratio of the mass of the gas molecule to the molar mass of the nanoparticle material), and

the more complex the gas molecule is, the lower the TAC. This reveals that energy is more readily accommodated into the translational modes of gas molecules compared to the internal modes of polyatomic molecules. These trends have also been observed for metal nanoparticles [47]. Therefore, the maximum energy transfer is defined as

$$\left\langle E_o - E_i \right\rangle_{\max} = 2k_{\mathrm{B}}\left(T_{\mathrm{p}} - T_{\mathrm{g}}\right) + \frac{\zeta_{\mathrm{rot}}}{2}\left(k_{\mathrm{B}}\left(T_{\mathrm{p}} - T_{\mathrm{g}}\right)\right) = \left(2 + \frac{\zeta_{\mathrm{rot}}}{2}\right)k_{\mathrm{B}}\left(T_{\mathrm{p}} - T_{\mathrm{g}}\right). \tag{2.27}$$

The conduction model then becomes

$$q_{\mathrm{cond}}\left(T_{\mathrm{p}}, d_{\mathrm{p}}\right) = \alpha\pi d_{\mathrm{p}}^2 N_{\mathrm{g}}^{''}\left\langle E_o - E_i \right\rangle_{\max}. \tag{2.28}$$

The differential equations of the heat transfer model can then be numerically solved with various methods, including Eulers' method, Runga-Kutta, implicit methods [105], or variable-step, variable-order method [106], the latter of which is used in this work and implemented in MATLAB© [107] with the "*ode113*" function, with initial conditions defined as the state of the probe volume at an initial temperature which could be either the gas temperature when simulating the laser heating, or the nanoparticle ensemble peak temperature when simulating only cooling.

The evaporation and conduction heat transfer rates from the nanoparticle vary in magnitude depending on laser fluence used for particle heating. Sipkens *et al*. [108] defined three fluence regimes that occur during the laser heating: the low fluence regime where the temperature of the nanoparticle increases linearly with laser energy, with conduction being the dominant cooling mechanism; the high fluence regime where the evaporative cooling balances the laser heating; and the moderate fluence regime that is a transition between the low and high fluence regimes. In all cases, other known and unknown phenomena of non-incandescent origins maybe be occurring during laser heating [24,28,109]. Additionally, at higher fluences, the effects of sublimation and evaporation can complicate results; for this reason, some LII studies avoid investigations in the

high fluence regime when sizing nanoparticles [21,38,70]. However, high fluence experiments have been carried to construct fluence curves for the laser-heated nanoparticles, where a plateau regime is expected in the vicinity of the boiling point of the material [61,110]. Although some degree of superheating is expected because heat is being added to the nanoparticle by the laser faster than it can be removed by evaporation under such non-equilibrium conditions [28], as seen in Figure 2-9. The evaporation from the nanoparticle is limited by Clausius-Clapeyron equation (*cf.* Eq. (2.22)) [29] and the extent of superheating depends on the temporal width of the laser pulse. A plateau regime starts to appear above the boiling point, T_b, of the material.

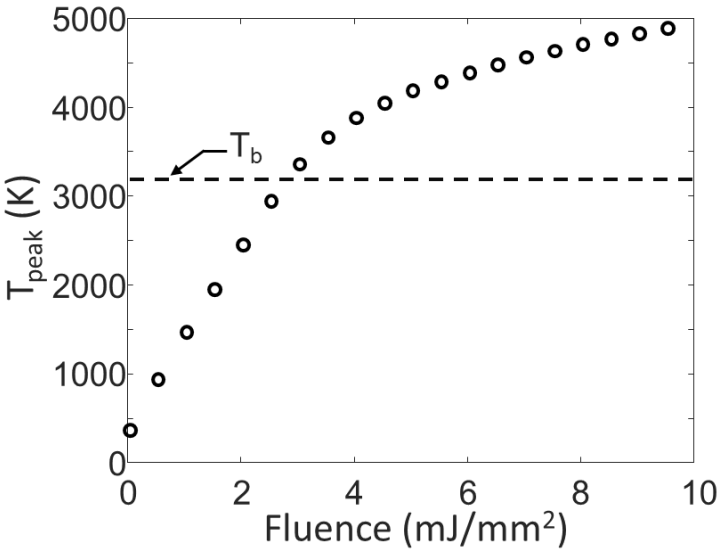

Figure 2-9: Simulated fluence curve for 25 nm Ni nanoparticle. Excessive absorption at the laser wavelength was accounted for during simulation (*cf.* §5.2.1).

2.3 Summary

This chapter described the TiRe-LII model, which included the spectroscopic and heat transfer submodels. Both Rayleigh and Mie theories were presented for determining the absorption efficiencies of the nanoparticles, although the Rayleigh approximation is not usually applicable for metal nanoparticles. The two-colour pyrometry method was also presented. The optical

properties for Ni and Fe nanoparticles were plotted and the data showed some variability in the literature for the refractive indices of the metals.

The description of the heat transfer submodel showed that cooling was mostly due to conduction and evaporation, which both take place in the free molecular regime due to the small length scale of the nanoparticle. The conductive cooling occurs as gas molecules scatter off the surface of the nanoparticle with an efficiency defined by the thermal accommodation coefficient. The results from the literature showed that the TAC increases with the mass of the gas molecule, with energy being more readily accommodated into the translational modes, causing a lesser TAC for systems of complex gas molecules. It was noted that evaporation from the nanoparticle dominates cooling at higher fluences, where non-equilibrium conditions are present, causing the superheating of the nanoparticle by the laser. In this work, these phenomena and other trends presented in this chapter are discussed in context with the TiRe-LII analysis of the experimental data that is collected by a modified TiRe-LII system discussed in the next chapter.

Chapter 3

TiRe-LII experimental apparatus

The experimental apparatus used in this work includes a two-colour TiRe-LII system obtained from the National Research Council (NRC) that was modified into a three-colour system and calibrated, and an aerosol generation system that aerosolized nanocolloids of Ni, Fe, Ag, and Au nanoparticles synthesized through wet chemical synthesis. This chapter presents the modification process of the TiRe-LII system, and a description of its operation and that of the nanoaerosol generator used to aerosolize the synthesized nanocolloids discussed in Chapter 4.

3.1 The TiRe-LII laser excitation and detection system

A two-colour TiRe-LII system (*cf.* Figure 3-1) was acquired from the National Research Council (NRC) and modified to a three-colour system and calibrated. It consists of a mobile optical breadboard with an optical network arrangement. The optical network broadly consists of a laser propagation pathway (or optical chain), the sample cell (or aerosol chamber) and the detection system. The various optical components arranged to make up the optical network are shown in Figure 3-2.

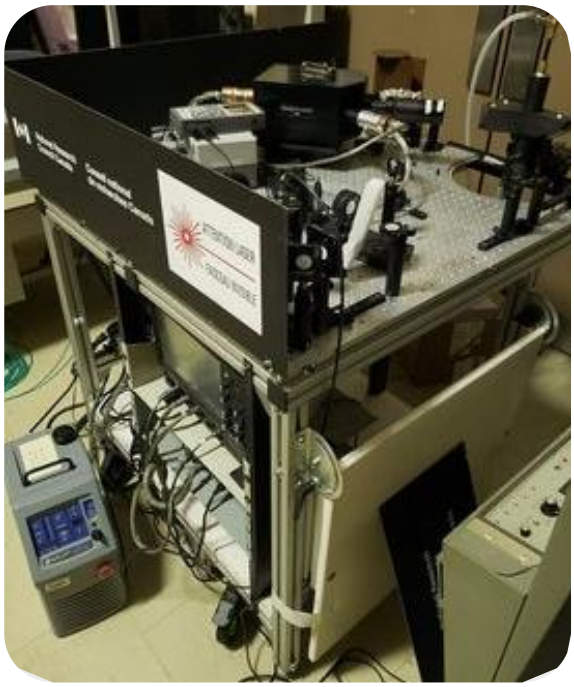

Figure 3-1: The TiRe-LII system acquired from NRC.

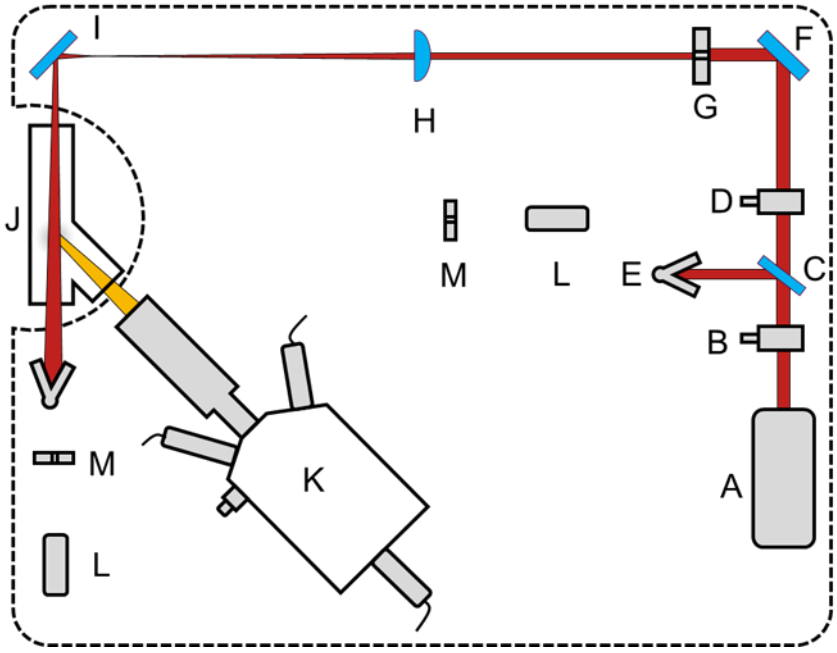

Figure 3-2: The optical network of the TiRe-LII system. Labels are shown in Table 3-1.

Table 3-1: Components of the optical network.

Part	Component Identity
A	1064 nm Nd: YAG laser
B	Half-wave plate #1
C	Polarizer
D	Half-wave plate #2
E	Beam dump
F	1064 nm mirror #1
G	2.4 mm ×1.5 mm ceramic slit
H	250 mm focal length plano-convex lens
I	1064 nm mirror #2
J	Sample cell (*cf.* §3.1.2)
K	Detector system (*cf.* §3.1.3)
L	670 nm laser diode
M	Iris diaphragm

The following subsections provide a detailed description of the function of each optical component in the optical network.

3.1.1 Laser beam propagation

The 1064 nm neodymium-doped yttrium aluminum garnet (Nd:YAG) laser (Big Sky Ultra CFR laser system) consists of a laser head and an integrated cooling and electronics (ICE) unit. The Nd: YAG laser works by flashing a noble gas-filled lamp (flashlamp) at a set pulse repetition frequency (PRF) in the proximity of an Nd: YAG crystal laser rod. The rod is pumped by absorbing the broadband graybody radiation from the flashlamp, which momentarily excites the neodymium ions that have a radiative lifetime of about 250 μs. Photons are then extracted from the rod in its laser resonator through a controlled stimulated emission (Q-switching). Q-switching produces a pulsed population inversion by allowing the rod in the laser resonator to acquire a sufficient gain to

overcome oscillation losses. Operating the Q-switch at a prescribed time delay after the flashlamp flashing controls the output laser energy by lasing within a specific time (delay) of the neodymium half-life [111].

The ICE unit controls the Q-switch delay and PRF, and provides cooling water to the laser head. The Q-switch is set at a nominal value of 135 μs, and the PRF is set to 20 Hz. This results in a 20 Hz lasing frequency with a maximum output energy of approximately 7.5 mJ, at the position of particle heating (probe volume) and a laser time profile, $f(t)$, with an FWHM of 8 ns, as shown in Figure 3-3, measured by a photodiode (PDA50B2 Amplified detector – Thorlabs).

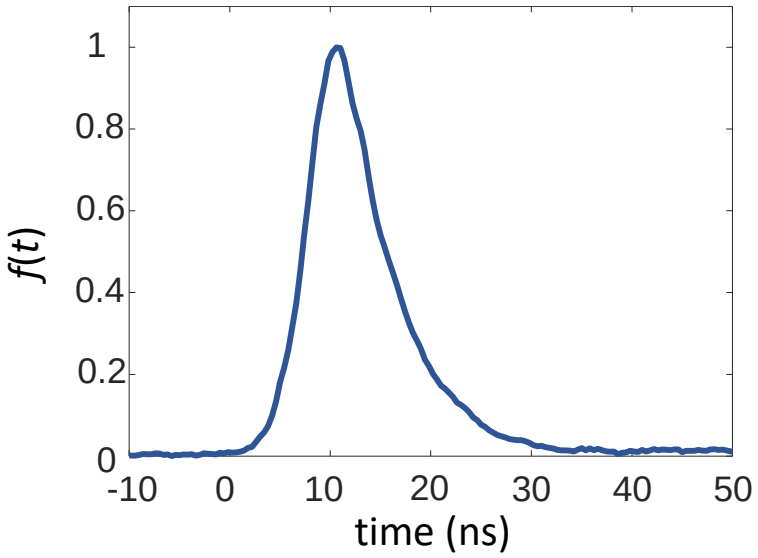

Figure 3-3: Laser temporal profile.

The ICE unit settings are maintained during experiments, and the maximum laser energy is controlled by an adjustable half-wave plate and polarizer arrangement (parts B, C, and D in Figure 3-2). The first half-wave plate converts the vertical polarization of the laser output beam into a polarization consisting of both vertical and horizontal components. The relative magnitudes of these components are defined by the half-wave plate control knob (*cf.* Figure 3-4). The beam then passes through the angled polarizer (Figure 3-2, part C) that dumps the vertically polarized

Figure 3-4: Adjustable half-wave plate.

component and transmits the horizontal component. The second half-wave plate was set to vertically polarize the experimental laser beam (i.e. the beam that heats up the nanoparticles). Although the second half-wave plate is unnecessary, the windows of the sample cell were designed to minimize the reflectivity of vertically polarized light[7] (*cf.* §3.1.2).

The first mirror (Figure 3-2, part F) is angled to deflect the laser beam by 90^{o} through a 2 mm tall by 1.5 mm wide ceramic slit (Figure 3-2, part G). The slit prevents diffraction around the beam edges to promote a spatially-uniform beam fluence by transmitting only the central, more uniform portion of the laser beam. This prevents non-uniform heating of particles at the probe volume defined within the sample cell (*cf.* §3.1.2), which can affect the TiRe-LII technique [112]. The laser beam is relay-imaged from the ceramic slit to the probe volume by a plano-convex lens with a focal length of 250 mm (Figure 3-2, part H). The plano-convex lens is placed half-way between the ceramic slit and the probe volume to achieve an approximate 1:1 magnification at the probe volume. The resulting beam cross-section at the probe volume was approximately 2 mm by 1.2

[7] This was done to ensure maximum scattering from vertically polarized light [72] for the Rayleigh scattering measurements that were previously performed with this setup.

mm, and the energy distribution in the vicinity of the probe volume, measured with a coherent beam laser-cam, is shown in Figure 3-5[8]. Some non-uniformities can be observed in the top right corner of the laser profile. The second mirror (Figure 3-2, part I) is used to deflect the laser beam by 90^{o} into the sample cell where the nanoaerosol is heated up. During experiments, the laser energy per pulse was measured with a pyrometric sensor connected to a laser energy meter (J-25MB-IR Feildmax II Coherent).

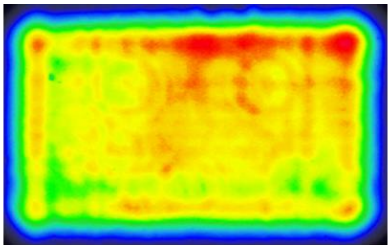

Figure 3-5: Laser beam profile measured at the probe volume.

3.1.2 Sample cell

The semicircle notch on the optical breadboard, shown in Figure 3-2, accommodates the sample cell. The cell encloses the probe volume from where incandescence is detected when the nanoaerosol is heated. The probe volume is defined by the intersection focal point of the collection optics (detection solid angle) and the laser (*cf.* Appendix C.3). The cell has three ports (*cf.* Figure 3-2, part J); all ports are equipped with fused silica glass windows. The glass windows over the laser entrance and exit apertures are positioned at Brewster's angle to minimize laser beam reflection and maximize transmitted laser energy to the probe volume. The detection glass window is normal to the angle of incidence, and the port has been angled by 35^{o} forward scattering angle[9],

[8] This image data was measured at NRC where the position of the plano-convex lens was slightly different.
[9] The scattering of light by a small particle is angle dependent [72].

with respect to the direction of laser propagation, to face the collection optics of the detection system. The cell was equipped with two additional ports: the aerosol entrance, at the top of the cell, and the exit, at the bottom of the cell. Figure 3-6 shows the sample cell installed on the optical table. Due to the small size of the sample cell, laser energy measurements could not be taken directly at the probe volume within the sample cell. Rather, energy measurements were taken at an earlier point in the optical chain and energy losses of up to 10%, due to optical components, are included when calculating the laser energy at the probe volume.

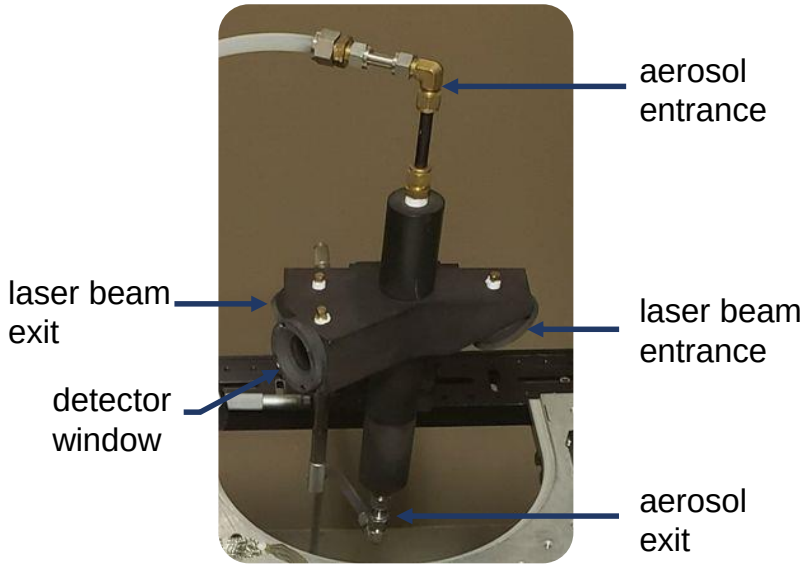

Figure 3-6: Aerosol sample cell.

3.1.3 Detection system

The detection system captures the incandescence emitted by the heated particles in the probe volume. It demultiplexes the broadband incandescence radiation into spectral widths defined by the optical components and their arrangement within the system. The detection system is a metal box consisting of five ports for positioning the collection optics, a laser diode, and three PMTs, as shown in Figure 3-7. Within the metal box are two dichroic mirrors and bandpass filters that selectively demultiplex the light entering the metal box through the collection optics.

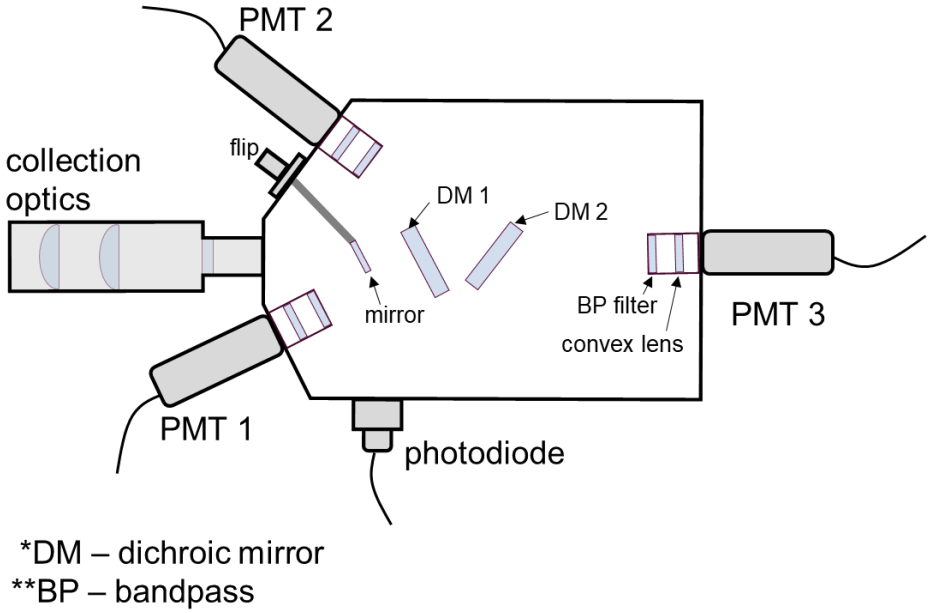

Figure 3-7: Detection system optics.

The collection optics assembly was configured for a 2X magnification of a 1 mm diameter aperture using a pair of 50 mm diameter achromatic[10] lenses of focal lengths 210 mm and 100 mm. Light entering the detection system through the optics is magnified, focused onto a 40 mm diameter lens, and collimated and imaged onto optical components within the system. The collection optics were operated at infinite conjugates, i.e., objects within the probe volume and their image produced within the demultiplexer box are at conjugate planes.

[10] This was to ensure that all the wavelengths were focused at the same distances.

3.1.3.1 Photomultiplier tube detectors

The detection system detects incandescence with photomultiplier tubes (PMTs), arranged as shown in Figure 3-7. PMTs amplify incident light based on the principle of the photoelectric effect and secondary emissions. Photons of light that enter the tube excite electrons in a photocathode, emitting photoelectrons through the photoelectric effect. The emitted photoelectron beam is focused and accelerated by electrodes onto a series of dynode stages; at each stage, each photoelectron excites more electrons (secondary emissions), resulting in an amplification effect. After the last dynode stage, the electrons are collected at an anode that induces a detectible current [113]. A schematic of the process is shown in Figure 3-8.

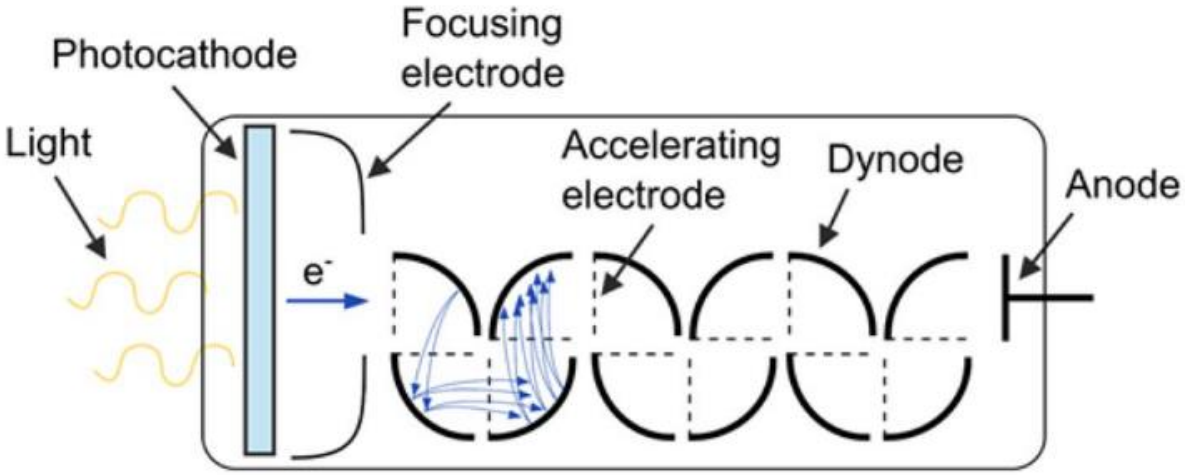

Figure 3-8: Schematic of a photomultiplier tube [66].

While the induced current output by the PMTs should ideally be proportional to the intensity of the incident light, this is not always the case. PMTs are prone to non-linear behaviour due to several phenomena: Photocathode resistivity increases with incident photon flux, resulting in less emitted photoelectrons [66]. In some cases, when the electron multiplier gain is too high, space-charge effects at the last dynode stage can limit the anode current [66]. There is sometimes a high photon flux at peak incandescence and non-linear behaviour at lower light levels [114]. For these

reasons, care must be taken when operating the PMTs during experiments by ensuring high-intensity signals are attenuated by neutral density (ND) filters and avoiding high PMT gains. Appendix C.2.1 provides the manufacturer-specified operating conditions for PMTs. The PMTs used in the detection system have a built-in high-voltage power supply and a voltage divider circuit. A voltage box is used to adjust the PMT electron gains by controlling the voltage supplied to the voltage divider circuit. An oscilloscope (HDO6104 1 GHz High Definition Oscilloscope – Teledyne) with a 50 Ω coupling converts the induced currents in the PMTs into digitized voltage readings.

The detector system initially consisted of two PMTs equipped with bandpass filters that defined the detection wavelengths. This was later modified to three detection wavelengths. The following paragraphs describe the demultiplexing mechanics of the two-colour system and the modified three-colour system.

3.1.3.2 Two-colour detection system

The two-colour detection system consists of PMTs 1 and 2 installed, as shown in Figure 3-7, and Figure 3-9 shows a schematic of radiation demultiplexing in the two-colour system. The collimated radiation entering the detection system through the collection optics is incident on the first dichroic mirror (angled at 15^{o} CCW), which is a long pass filter with a cut-off wavelength at 486 nm. The short wavelength radiation is reflected onto a bandpass filter with a center wavelength of 419.9 nm and a spectral width of 14.5 nm and is focused by a plano-convex lens, with a 50 mm focal length, onto the first PMT (Hamamatsu H5783-03 bialkali photosensor module). The long wavelength radiation is transmitted through the mirror and imaged onto the second dichroic mirror

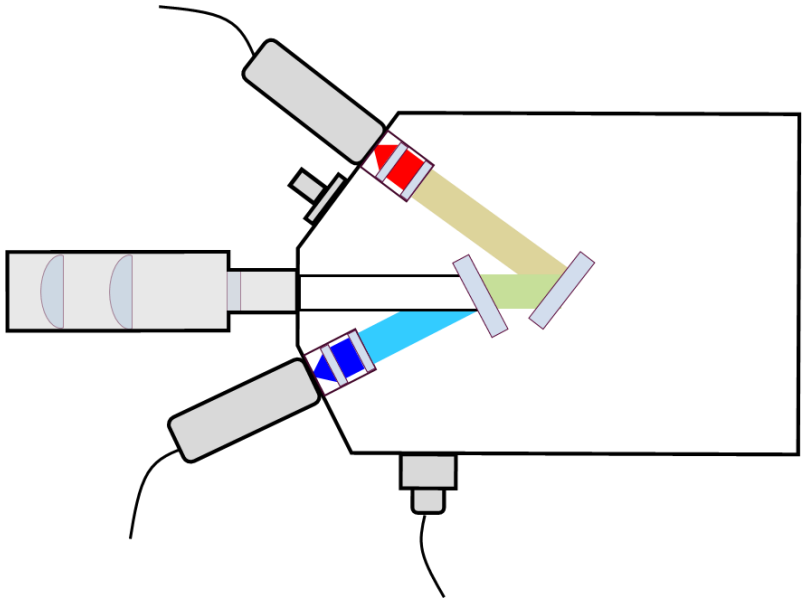

Figure 3-9: Two-colour LII detection system (*cf.* Figure 3-7 for part labels).

(angled at 15° CW) that is a long pass filter[11] that reflects radiation onto a second bandpass filter with a center wavelength of 750 nm and a spectral width of 50 nm. The radiation is then focused by a plano-convex lens with a 50 mm focal length onto the second PMT (Hamamatsu H5783-20 bialkali photosensor module).

3.1.3.3 Three-colour detection system

The three-colour detection system consists of all three PMTs in Figure 3-7. The choice of detection wavelengths during the modification process considered the following:

I. Liu *et al*. [115] showed, through sensitivity and shot noise analyses, that more accurate LII results are achieved when selected detection wavelengths are as far apart as possible.

II. Since the excitation wavelength (i.e. the laser wavelength) is at 1064 nm, none of the selected detection wavelengths should be within the spectral vicinity of 1064 nm or its

[11] Information of the cut-off wavelength was not available.

harmonics to avoid the excitation laser from contaminating the detected incandescence signal.

Considering the above points, the shortest detection wavelength was chosen as 445 nm, and the longest detection wavelength was chosen as 747 nm[12]. A third detection wavelength should be chosen to be equidistant between the shortest and longest detection wavelength and out of the vicinity of 532 nm (the second harmonic of the 1064 nm laser pulse). A 597 nm detection wavelength fits both criteria; however, limited by choice of available bandpass filters, an effective center wavelength of 625 nm was achieved by combining a long pass dichroic mirror with a cut-off wavelength at 640 nm and a bandpass with a center wavelength at 650 nm. Note that all optical components are spectrally characterized before installation to ensure proper calibration (*cf.* Appendix C.1.2).

Figure 3-10 shows a schematic of radiation demultiplexing in the three-colour system. Collimated radiation entering the detector system through the collection optics is incident on the dichroic mirror (angled at 15^{o} CCW), which is a long pass filter with a cut-off wavelength at 486 nm. The short wavelength radiation is reflected onto a bandpass filter with a center wavelength of 445 nm and a spectral width of 32 nm and then focused by a plano-convex lens with a 50 mm focal length onto the first PMT (Hamamatsu H5783-03 bialkali photosensor module). The longer wavelength radiation is transmitted and incident on the dichroic mirror (angled at 15^{o} CW) that is a long pass filter with a cut-off wavelength at 640 nm. The reflected radiation is incident onto a second bandpass filter with a center wavelength of 650 nm and a spectral width of 70 nm and then focused by a plano-convex lens with a 50 mm focal length onto the second PMT (Hamamatsu

[12] These choices were limited by the available bandpass filters.

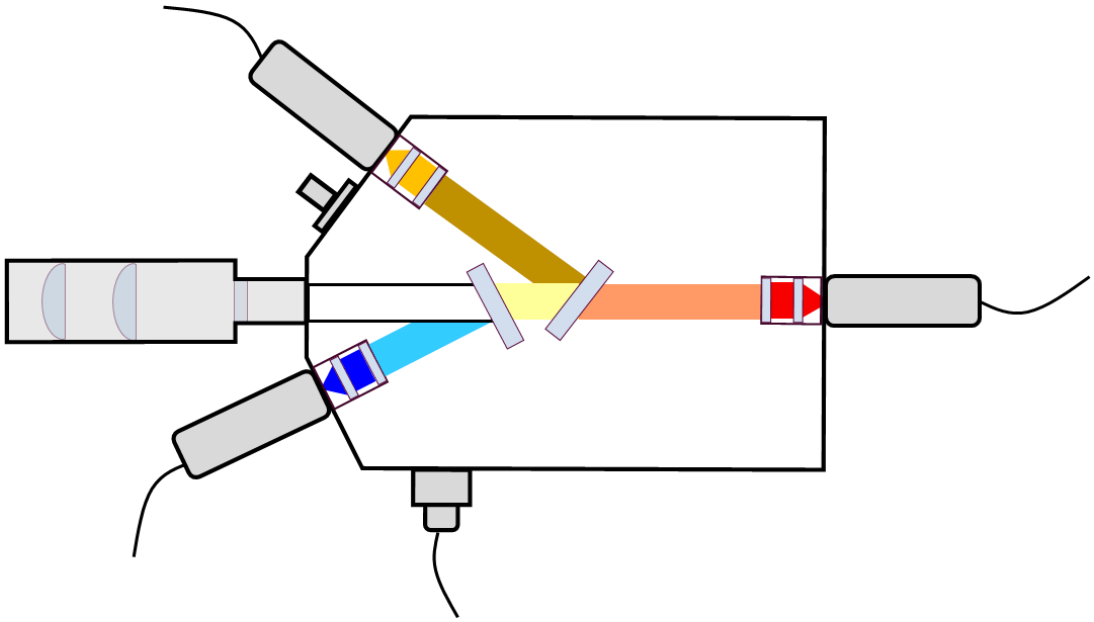

Figure 3-10: Three-colour LII detection system (cf. Figure 3-7 for part labels).

H5783-01 bialkali photosensor module). The longest wavelength radiation (beyond the 640 nm cut-off wavelength of the second dichroic mirror) is transmitted and incident on a third bandpass filter with a center wavelength of 650 nm and a spectral width of 70 nm and then focused by a plano-convex lens onto the third PMT (Hamamatsu H5783-01 bialkali photosensor module).

The three-colour detection system was calibrated following the procedure of Mansmann *et al.* [66]. The transmittance of the optical components within the detector system and the details of the calibration process are described in Appendix C.1.2. Calibration results suggested that the 650 nm PMT channel did not have a reliable calibration factor. After all troubleshooting efforts, it was concluded that quantitative analysis would be conducted with only two colours with detection wavelengths at 445 nm and 747 nm[13]. The laser propagation path was aligned to ensure that the laser and the focal point of the collection optics intersected. This defined the probe volume from

[13] A calibrated spectrometer was used to accurately determine the center wavelengths of the bandpass filters (*cf.* Appendix C.1.1).

which incandescence information was captured. The alignment process is discussed in Appendix C.3.

3.2 Aerosol generation system

The metal nanoaerosols were generated by aerosolizing a metal nanocolloid with a pneumatic atomizer (TSI Model 3076) and drying the nanoparticle with a diffusion dryer, as seen in Figure 3-11. The nanocolloid was aerosolized by passing a motive gas, at a pressure of 25 psi, through the atomizer. As the gas expands through an orifice to form a high-velocity jet, the nanocolloid is driven upstream and atomized by the jet. Large droplets are removed by impaction on the wall opposite the jet (*cf.* Figure 3-11). Excess liquid is drained at the bottom of the atomizer back into the nanocolloid, and small droplets, with a mean droplet diameter of 0.35 μm (for an aqueous nanocolloid), flow upstream [116]. The nanocolloid critical concentration, $conc_{cr}$, in mg of nanoparticle per volume of solvent is calculated from

$$conc_{cr} = \rho_p \left(\frac{d_p}{d_s} \right)^3 , \tag{3.1}$$

where ρ_p and d_p are the nanoparticle's density and diameter, respectively, and d_s is the diameter of the nanocolloid solvent droplet. This produces, on average, one nanoparticle per droplet. However, the drainage of excess fluid dilutes the nanocolloids overtime during the aerosolization process.

The wet aerosol[14] passes through a diffusion dryer filled with desiccant surrounding the aerosol flow path to evaporate the solvent surrounding the nanoparticles before flowing into the sample cell. It should be noted that the motive gas used to aerosolize the nanocolloid can affect the final volume fraction within the sample cell due to the nature of the aerosolization process. The heavier

[14] The wet aerosol refers to the aerosolized nanoparticles within solvent droplets.

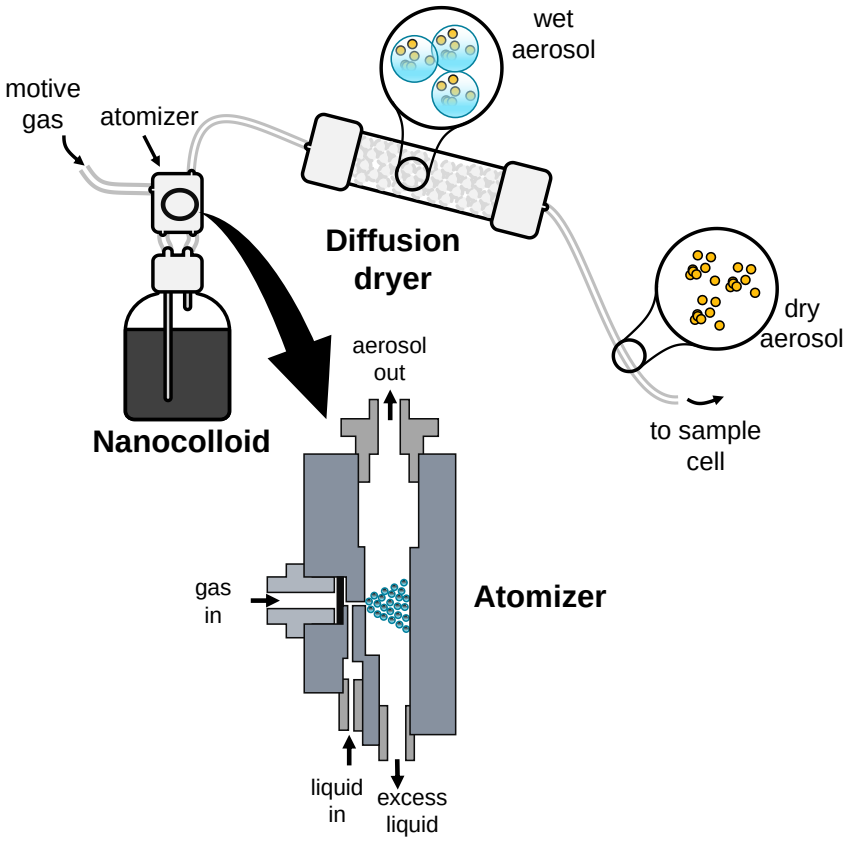

Figure 3-11: Aerosolization setup.

the gas molecule, the more nanocolloids are drawn upstream as the gas expands due to viscous effects.

After the sample cell, the nanoaerosol is bubbled through water to extract most of the aerosolized nanoparticles. An exhaust vent is operated over the bubbled water to exhaust any nanoparticles that escape from the water. The bubbling water also acts as an indication that the system is gas-tight during experiments. Note that although the motive gas is passed through the atomizer at 25 psi, the sample cell is at atmospheric pressure.

3.3 Summary

This chapter outlined the different components that make up the TiRe-LII apparatus. The optical network was described, including the Q-switching mode of the laser head and its energy-

controlling optics. Each optical component and its function in the laser optical chain were discussed. The architecture of the sample cell that encloses the LII probe volume was also presented. The optical network within the detection system and its components, including the PMTs, dichroic mirrors and bandpass filters, were described. The considerations during the modification process from a two-colour to three-colour LII system were described, and the calibration and validation of the detection system are presented in Appendix C.4.

The operation of the aerosol generator was presented along with considerations of the required nanocolloid concentration. Following the preparation and validation of the TiRe-LII apparatus, the nanocolloids were synthesized through wet chemical synthesis, and LII experiments were conducted as described in Chapter 4.

Chapter 4

Experimental procedure and data collection

The LII apparatus presented in the previous chapter is used to characterize laser-induced emissions from aerosolized metal nanoparticles. These include aerosols of Ni and Fe nanoparticles to infer the size distribution and thermal accommodation coefficient (TAC) in various motive gases and laser fluences, and aerosols of Ag and Au nanoparticles to investigate LII signal corruption. The aerosol generator produced nanoaerosols from nanocolloids synthesized by reducing an appropriate precursor, usually a salt of the metal, and capped with a polymer or surfactant material to prevent agglomeration or aggregation[15]. This chapter describes the synthesis procedure of the nanocolloids, presents *ex situ* characterization measurements, and describes the LII data collection procedure.

4.1 Synthesis of nanoparticles

4.1.1 Synthesis of Ni nanoparticles

The Ni nanocolloid was synthesized using a customized synthesis procedure, based on Refs. [117–122], by considering the effect of solution medium, reaction temperature, surfactant, and molar ratios. The precursors used included Ni (II) chloride ($NiCl_2$), hydrazine monohydrate ($N_2H_4.H_2O$), sodium hydroxide (NaOH), and polyvinylpyrrolidone (PVP-K30). The reaction took place as follows [120].

$$2Ni^{2+} + N_2H_4 + 4OH^- \rightarrow 2Ni + N_2 + 4H_2O\,. \tag{4.1}$$

[15] Agglomeration refers to particles loosely attached by weak forces such as Van der Waals forces and aggregates refers to particles tightly held together by strong forces such as covalent or metallic bonds [181].

Upon the addition of each precursor, the solution changed colour, as shown in Figure 4-1.

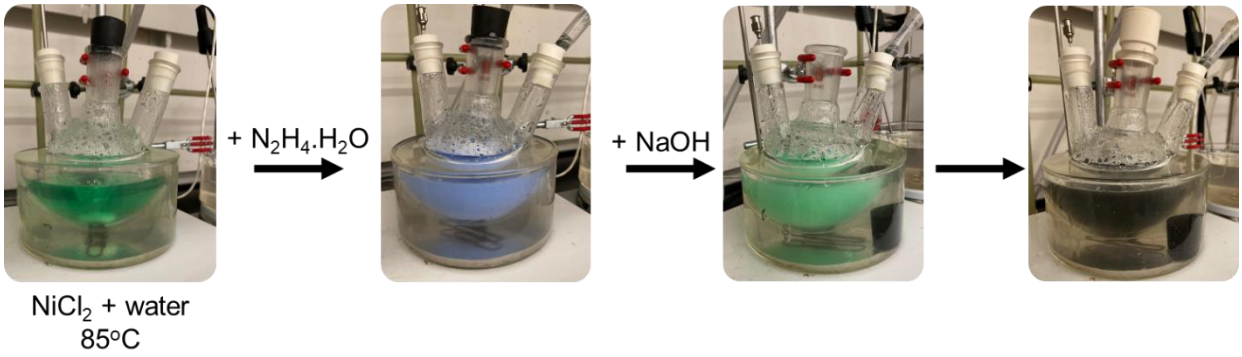

Figure 4-1: Solution colour change during the synthesis of Ni nanoparticles.

A 50 ml aqueous solution[16] of 0.16 M of $NiCl_2$ was prepared under vigorous mechanical stirring and heated to 85°C under reflux, resulting in a clear green solution (*cf.* Figure 4-1 (a)). $NiCl_2$ was reduced by gradually adding (dropwise) $N_2H_4.H_2O$ to the solution resulting in a N_2H_4/Ni^{2+} molar ratio of 7 (this results in excess[17] N_2H_4) and producing a cloudy blue solution (*cf.* Figure 4-1(b)). An aqueous solution of NaOH, which acts as a catalyst, was added to the solution resulting in a $NaOH/Ni^{2+}$ molar ratio of 5 and producing a cloudy green solution (*cf.* Figure 4-1 (c)). (A minimal amount of ultrapure water (Millipore) was used in preparing aqueous NaOH). The solution was stirred and heated until it turned black, indicating the formation of zero-valent Ni nanoparticles (*cf.* Figure 4-1 (d)). A 5 ml solution of PVP-K30 with a $PVP\text{-}K30/Ni^{2+}$ molar ratio of 8, was prepared and added to the solution to stop the reaction and suppress sintering. The resulting nanocolloid was washed twice with ultrapure water using a centrifuge and finally dispersed in ultrapure water. The Ni nanocolloid was sampled onto TEM copper grids for *ex situ* characterization.

[16] The aqueous solutions were prepared by dissolving the solutes in ultrapure water (Millipore) unless otherwise mentioned.
[17] All reducing agents for the nanoparticle synthesis are added in excess to ensure a complete reduction of the metal salt precursor.

It was not necessary to perform the synthesis under an inert atmosphere to prevent oxidation as the reduction reaction produced nitrogen gas, as seen from Eq. (4.1), which acts as an inert reaction atmosphere.

4.1.2 Synthesis of Fe nanoparticles

The Fe nanocolloid was synthesized using a customized procedure based on Refs. [123–128]. The precursors included iron (II) sulphate heptahydrate ($FeSO_4.H_2O$), sodium borohydride ($NaBH_4$), and carboxymethylcellulose (CMC). The reaction took place as follows [126].

$$2Fe^{2+} + BH_4 + 4H_2O \rightarrow 2Fe + B\ OH\ {}^{-}_{4} + 2H_2 \qquad (4.2)$$

A solution of 8.29 g of $FeSO_4.H_2O$ and 70 ml of ultrapure water was prepared under an inert atmosphere and magnetic stirring. Carboxymethylcellulose (CMC) was added to the solution (1.1 wt% of the total solution weight) to prevent agglomeration and/or aggregation. Separately, a 30 mL solution of $NaBH_4$ was prepared for a molar ratio of $BH_4^+/Fe^{2+} = 5$; this resulted in excess of $NaBH_4$. This solution was gradually added (dropwise) to the $FeSO_4.H_2O$ + CMC solution to reduce $FeSO_4.H_2O$. The reaction was allowed to continue under magnetic stirring until it turned black (*cf.* Figure 4-2), indicating the formation of zero-valent Fe nanoparticles.

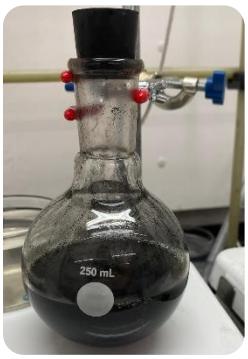

Figure 4-2: Fe nanocolloid

The resulting nanocolloid was washed twice with ultrapure water using a centrifuge and finally dispersed in ultrapure water. The Fe nanocolloid was sampled onto TEM copper grids for *ex situ* characterization.

4.1.3 Synthesis of Ag nanoparticles

Positively- and negatively-charged Ag nanoparticles were synthesized to investigate LII signal corruption from non-incandescent sources since some of these, such as Bremsstrahlung, are expected to be charge-dependent [58]. Negatively-charged Ag nanoparticles were synthesized according to Ref. [129]. An aqueous solution of silver nitrate, $AgNO_3$, was prepared by dissolving 170 mg of $AgNO_3$ in 170 mL of deionized (DI) water. More DI water was then added to yield a final volume of 1000 mL. The solution was put under magnetic stirring, heated to 90°C and brought to a boil. A solution of 1% trisodium citrate, $Na_3C_6H_5O_7$, was prepared by dissolving 200 mg of $Na_3C_6H_5O_7$ in 20 mL of DI water and added to the boiling $AgNO_3$ solution. The $Na_3C_6H_5O_7$ solution acted as reducing agent and anionic surfactant/capping agent. The chemical reaction was allowed to continue under magnetic stirring and heating for 1 hr resulting in a milky yellow solution, as seen in Figure 4-3(a), indicating the presence of Ag nanoparticles. The solution was allowed to cool to room temperature and the negatively-charged Ag nanocolloid was sampled onto TEM copper grids for *ex situ* characterization.

Positively-charged Ag nanoparticles were synthesized using a customized procedure based on Refs. [130–135]. A 25 mL aqueous solution[18] of 5 mM $AgNO_3$ and a 25 mL of 1 mM of cetrimonium bromide, CTAB (acting as a cationic surfactant/capping agent), were prepared separately and mixed under magnetic stirring (Solution A). A 25 mL solution of 15 mM $NaBH_4$

[18] The aqueous solutions in this synthesis were made with DI water.

(acting as a reducing agent) and another 25 mL of 1 mM CTAB were prepared separately and mixed under magnetic stirring (Solution B). Solution A and B were then mixed under magnetic stirring for 100 min resulting in a clear brown solution, as seen in b. The negatively-charged Ag nanocolloid was sampled onto TEM copper grids for *ex situ* characterization.

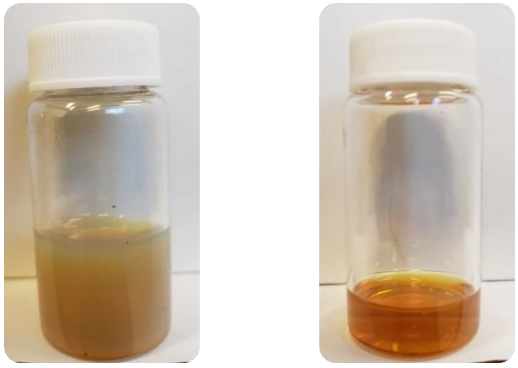

a b

Figure 4-3: (a) Negatively- and (b) Positively-charged Ag nanocolloids. The colour difference is due to the different sizes of the Ag nanoparticles (*cf.* §4.2.2).

4.1.4 Synthesis of Au nanoparticles

Only negatively-charged Au nanoparticles were synthesized. Negatively-charged Au nanoparticles were synthesized according to Ref. [136]. A 50 mL aqueous solution of Chloroauric acid, $HAuCl_4$, (0.1 % by weight of solution) and a 0.5 mL aqueous solution of trisodium citrate, $Na_3C_6H_5O_7$, (1 % by weight of solution) were prepared using ultrapure water. The $HAuCl_4$ solution was heated to boiling, and the $Na_3C_6H_5O_7$ solution was added. After 25 s the boiling solution turned faint blue, indicating nucleation had begun, and after approximately 70 s the solution turned dark red (turns brilliant red upon dilution), as seen in Figure 4-4, indicating the formation of Au nanoparticles. The solution was allowed to cool to room temperature and washed twice with ultrapure water using a centrifuge and finally dispersed in ultrapure water. The Au nanocolloid was sampled onto TEM copper grids for *ex situ* characterization.

Figure 4-4: Negatively-charged Au nanocolloid.

4.2 *Ex situ* characterization of nanoparticles

The synthesized nanoparticles were characterized using four *ex situ* characterization techniques, including transmission electron microscopy (TEM), dynamic light scattering (DLS), ultraviolet-visible (UV-Vis) spectroscopy, and zeta potential analysis.

In transmission electron microscopy (TEM) an electron beam is generated with an electron gun and focused onto a sufficiently thin sample to be imaged. Some of the electrons are scattered, absorbed, or transmitted. The transmitted electrons and their energies provide information about the sample since different parts of the sample transmit electrons with varying magnitudes. A 2D image is then generated as the transmitted electrons are imaged onto a detector [137].

Dynamic light scattering (DLS) is a technique used to measure the size distribution of suspended particles in a colloid. It operates on the principle of Brownian motion. Larger particles diffuse through the solution (i.e. undergo Brownian motion) slower than smaller particles. The hydrodynamic diameter[19] of the particles can be determined from the Stokes-Einstein equation,

$$d_{\mathrm{h}} = \frac{k_{\mathrm{B}}T}{3\pi\eta D}, \tag{4.3}$$

[19] The hydrodynamic diameter is the size of the sphere that diffuses at the same rate as the particle.

where d_h is the hydrodynamic diameter of the particle, k_B is Boltzmann's constant, η is the viscosity of the solvent, T is the temperature of the solution, and D is the diffusion coefficient of the particle. The diffusion coefficient is determined by the scattering of light by the particles. A laser is passed through a sample of the nanocolloid and the scattering intensities of the suspended particles are measured over time. Smaller particles cause more rapid fluctuations in the scattered light than larger particles. An auto-correlator quantifies the change in scattered light intensity over time to determine the diffusion coefficient [138–140]. Because DLS measures the hydrodynamic diameter of the particle, the core particle and any surface material cannot be differentiated.

Ultraviolet–visible (UV-Vis) spectroscopy is an optical diagnostic used to determine the spectral extinction efficiencies of particles suspended in solution. A beam of light with wavelengths in the ultraviolet–visible spectrum is passed through a sample nanocolloid and the spectral variation in intensity (extinction) caused by the particles is measured. Plasmonic nanoparticles couple to electromagnetic waves resulting in a surface plasmon resonance at specific wavelengths (plasmonic peak)[20], depending on their size [141]. The extinction of the light intensity is size-dependent and can be modelled by Mie theory. Since the spectral extinction efficiencies and plasmonic peaks of Ag and Au nanoparticles are well known in the literature, UV-Vis spectroscopy data can provide information about the purity (contaminants can shift the plasmonic peaks or introduce artifacts in the UV-Vis spectrum) and the size distribution of the nanoparticles (the broader the plasmonic peaks, the more polydisperse the nanoparticles).

Zeta potential analysis is a technique used to quantify the charge of a particle. The zeta potential is related to the number of electrical charges on the surface of a particle. In this technique, the nanocolloid is placed in a cell with two oppositely charged electrodes. An electric field is

[20] It is for this reason that plasmonic nanoparticles suspended in solution have distinct colours depending on their size.

applied to the nanocolloid and charged particles undergo translational motion (electrophoresis) towards an electrode that has a charge opposite to that of the particle. The faster the motion, the larger the magnitude of the charge. The velocity of the particle is determined through laser Doppler velocimetry and the zeta potential is determined through Henry's equation,

$$U_{\mathrm{E}} = \frac{2\varepsilon\zeta F(\kappa a)}{3\eta}, \tag{4.4}$$

where U_{E} is the electrophoretic mobility, ε is the dielectric constant of the solvent, η is the viscosity, ζ is the zeta potential and $F(\kappa a)$ is the Henry function. More detail of the technique can be found in Refs. [140,142,143].

4.2.1 *Ex situ* characterization of Ni and Fe nanoparticles

Ex-situ characterization of Ni and Fe nanoparticles was performed with TEM and DLS (VASCO Particle Size Analyzer) to determine their size distribution. Figure 4-5 shows the TEM micrograph and size distribution of the Ni and Fe nanoparticles. The micrographs were analyzed with ImageJ open source software that determines the diameter of each individual nanoparticle on the micrograph relative to the scale bar. The samples of particle diameters were fit to appropriate distributions using the "*histfit*" and "*fitdist*" functions in MATLAB® [107]. The size distribution of the Ni nanoparticles was fit to a normal distribution with a mean of 105.6 nm and a standard deviation of 22.7 nm, and the size distribution for Fe nanoparticles was fit to a lognormal distribution with a geometric mean of 71.8 nm and a geometric standard deviation of 1.3. The Fe nanoparticles were more aggregated compared to the Ni nanoparticles.

The DLS results suggested that the Ni and Fe nanoparticles had mean diameters between 300 nm – 500 nm, which were inconsistent with TEM analysis. These results could be either due to the DLS technique measuring the hydrodynamic diameter of the nanoparticles with the capping

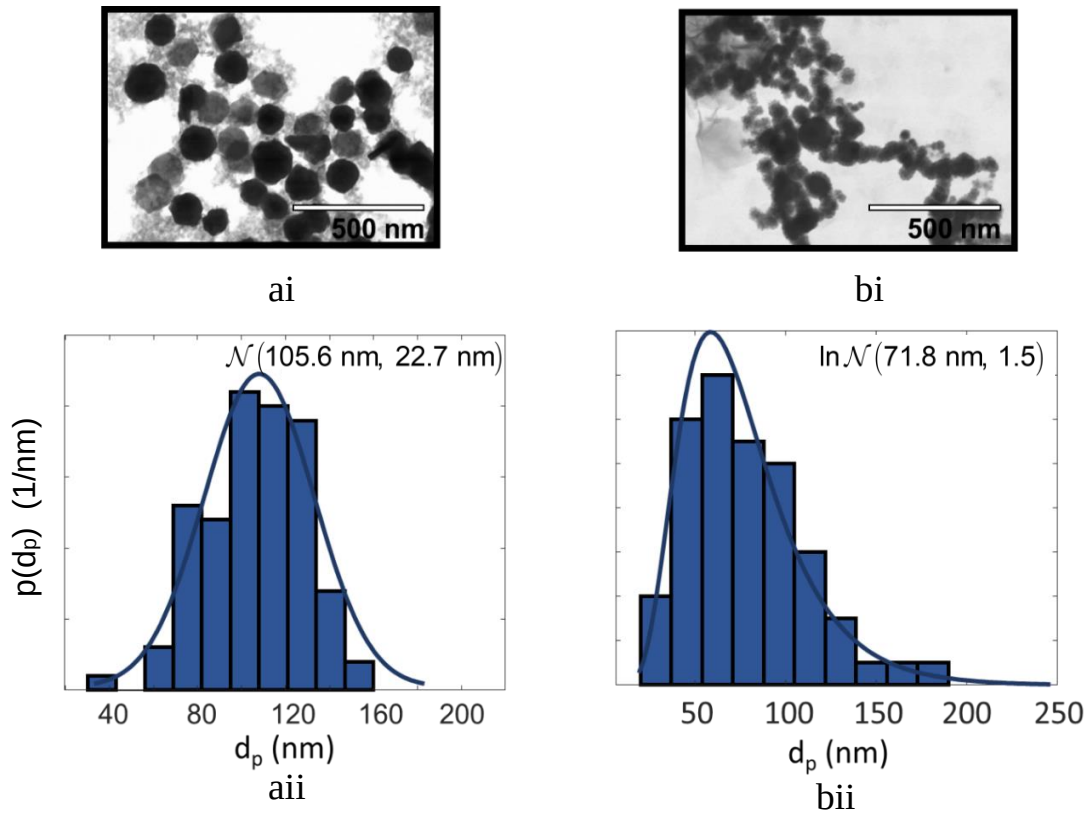

Figure 4-5: TEM micrographs of (ai) Ni nanoparticles and (aii) Ni size distribution, and (bi) Fe nanoparticles and (bii) Fe size distribution.

polymers attached to the surface of the nanoparticle or because the DLS measurements were carried out about three days after synthesis, allowing time for agglomeration and/or aggregation. Measurements carried out by DLS a week later showed that nanoparticles were significantly aggregated to sizes of about 1000 nm, and ultrasonication did not change the results. The Fe nanoparticles were also observed to have significantly oxidized over time, indicated by the rusty colour of the nanocolloid. This result suggests that there might be some aggregation of the nanoparticles particles during experiments.

4.2.2 *Ex situ* characterization of Ag and Au nanoparticles

Ex-situ characterization of Ag and Au nanoparticles was performed with TEM, DLS (VASCO Particle Size Analyzer), UV-Vis spectroscopy, and zeta potential analysis (Wallis Zeta potential analyzer).

Figure 4-6 shows the TEM micrograph and size distribution of the Ag and Au nanoparticles. The size distribution for negatively- and positively-charged Ag and negatively-charged Au nanoparticles obey a lognormal distribution with geometric means of 43.1 nm, 29.1, and 19.7 nm, respectively, with a geometric standard deviation of 1.31, 1,36, and 1.36, respectively. DLS results for these nanoparticles were inconclusive as results varied with each trial.

Zeta potential analysis results showed that the negatively-charged Ag and Au nanoparticles had zeta potentials of -11.66 mV and -17.82 mV, respectively. Zeta potential analysis measurements for positively-charged Ag nanoparticles were inconclusive because different batches of the nanocolloid produced different signs of the zeta potential. This could be because the net surface charge might not be strongly polarized and therefore to weak to produce reliable zeta potential measurements.

Figure 4-7 shows the UV-Vis spectrum of the positively-charged Ag and negatively-charged Au nanoparticles. The size-dependent plasmonic peaks of Ag nanoparticles occur between 400 nm – 500 nm [133], and that of Au nanoparticles occurs between 500 nm – 600 nm [144]. The UV-Vis measurements fall within these ranges, with no additional peaks or artifacts suggesting the presence of pure Ag and Au nanoparticles with no contaminants.

The UV-Vis spectrum obtained from the negatively-charged Ag nanoparticles is broader than that of the positively-charged Ag nanoparticles, suggesting that the negatively-charged Ag nanoparticles are more polydisperse. This result is inconsistent with the TEM analysis since the geometric standard deviation of the negatively-charged Ag nanoparticles is slightly narrower than that of the positively-charged Ag nanoparticles. This could be because of outliers, in the TEM sample of diameters, at larger size classes that broaden the geometric standard deviation for the positively-charged Ag nanoparticles, which could also be happening of the Au nanoparticles.

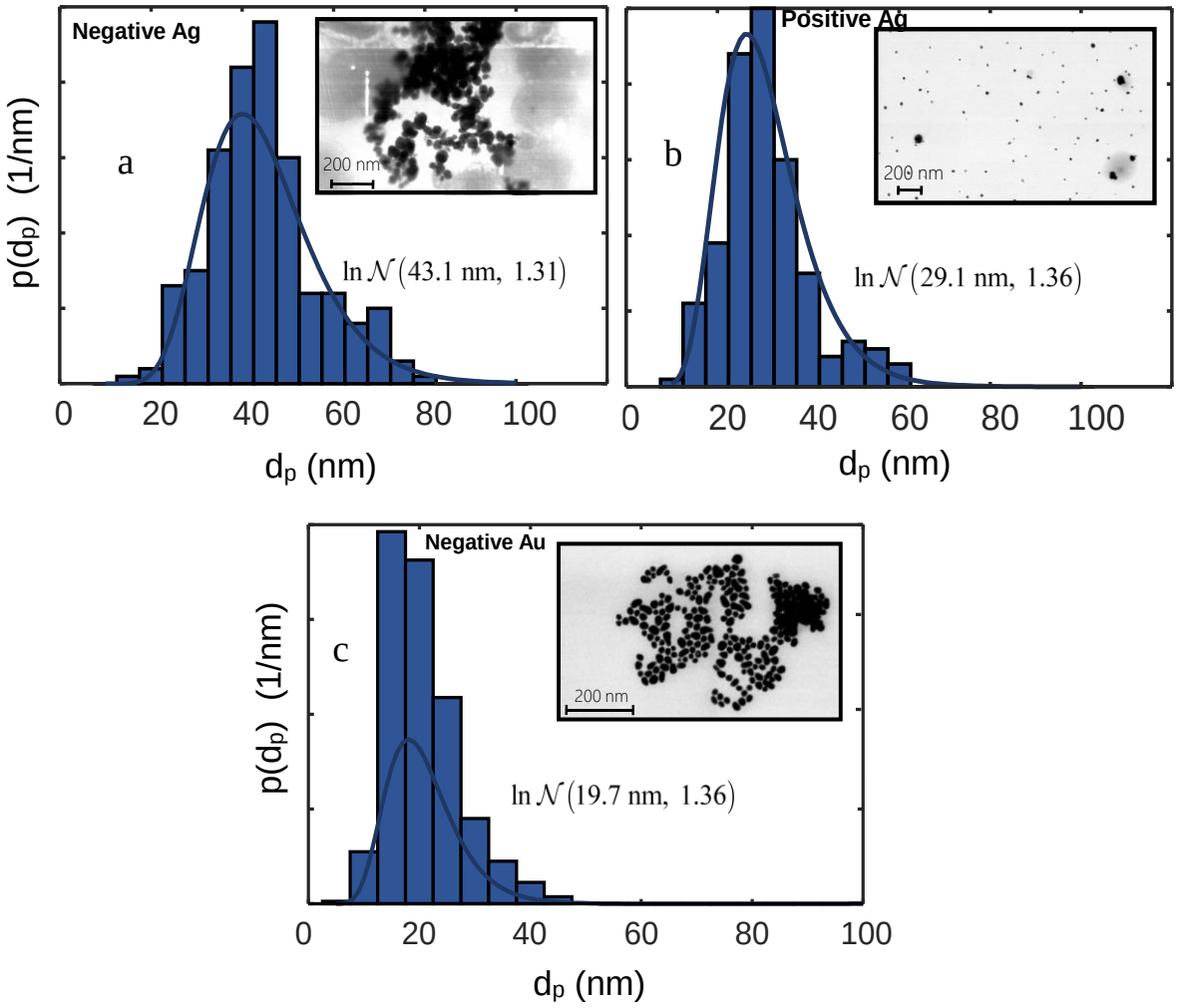

Figure 4-6: Size distribution of (a) negatively- (b) positively-charged Ag nanoparticles and (c) negatively-charged Au nanoparticles and thier respective TEM micrographs (insets).

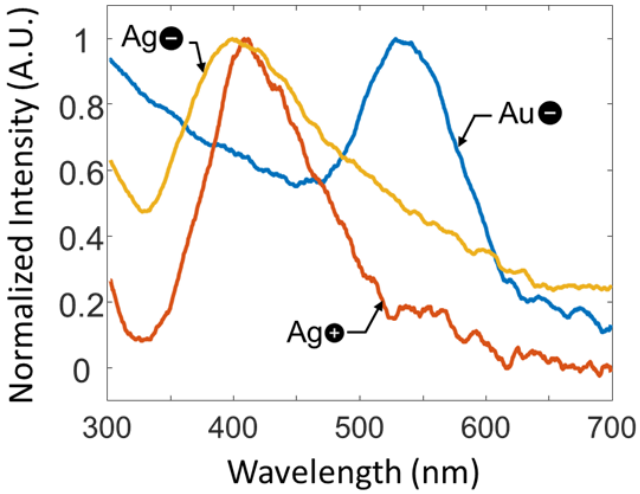

Figure 4-7: UV-Vis data of synthesized plasmonic nanoparticles.

4.3 TiRe-LII data collection

The nanoaerosols were generated with five motive gases, including He, N_2, Ar, CO, and CO_2, which were all supplied to the atomizer at 25 psi. Upon generating and flowing the nanoaerosols into the sample cell, incandescence data from the laser-heated nanoparticles were captured at 445 nm, 557 nm, and 747 nm. The oscilloscope recorded the incandescence signals from the PMTs at a 2.5 GHz sampling rate; a LabVIEW program was used to automate the data collection and saving process from the oscilloscope.

For Ni nanoparticles, data were collected at five different fluences for the He, N_2, CO, and CO_2 aerosols and ten fluences for the Ar aerosol. For each set of data, forty runs were captured, with each run being an average of fifty shots to improve the signal-to-noise ratio.

For Fe nanoparticles, data were collected at one fluence for the He, N_2, CO, and CO_2 aerosols and at five fluences for the Ar aerosol. For each set of data, 150 runs were captured, with each run being an average of ten shots. Only ten shots were averaged because the LII measurements carried out on the Fe nanoparticles had a better signal-to-noise ratio.

For the positively- and negatively-charged Ag nanoparticles, data were collected at five fluences, each for the He, N_2, and CO_2 aerosols. For each set of data, 150 runs were captured, with each run being an average of ten shots.

For Au nanoparticles, data were collected at three fluences, each for the He, N_2, and CO_2 aerosols. The concentration of the nanocolloid was not sufficient to collect reliable data at lower fluences. For each set of data, 150 runs were captured, with each run being an average of ten shots.

LII data for Ni and Fe nanocolloids were collected one day after the nanocolloids were synthesized to minimize the effects of aggregation and oxidation that became increasingly

significant days after synthesis. The Ag and Au nanocolloids remained stable for a longer period of time. The concentration of the nanocolloids were greater than the estimated critical concentration, as determined by Eq. (3.1), to improve the signal-to-noise ratio at lower fluences. Since the atomizer dilutes the nanocolloids overtime during the aerosolization process, the nanocolloid concentrations were increased at regular intervals during data collection and were also agitated regularly to prevent any settling that may have occurred. The laser energies used varied from 1.3 mJ/mm^2 – 3.1 mJ/mm^2. Although data were captured at all three detection wavelengths, data from only the shortest (445 nm) and longest (747 nm) detection wavelengths were used for quantitative analysis.

To further improve the data quality, at each data set, noise from the laser Q-switch was captured by the PMTs and subtracted from the incandescence data. This could be done because the Q-switch noise was stable and unchanging during the data collection (*cf.* Appendix E.2).

For each gas dataset, the data were collected at one set gain at each PMT for all fluences to allow for one gain calibration factor to be applied across each motive gas dataset; however, for one of the fluence datasets, data were collected at three different sets of gains to ensure there was no non-linearity. Pyrometric temperature profiles showed that there were no non-linearities during the experiments (*cf.* Appendix E.3).

4.4 Summary

This chapter described the wet chemical synthesis procedure for synthesizing Ni, Fe, Ag (positively- and negatively-charged), and negatively-charged Au nanocolloids that were aerosolized by a pneumatic atomizer. The *ex situ* measurements and results by TEM, DLS, UV-Vis, and zeta potential analysis were presented.

The TEM analysis showed that the Ni nanoparticles sampled from the colloid obeyed a normal distribution with a mean of 105.6 nm and a standard deviation of 22.7 nm, while the Fe nanoparticle sizes obeyed a lognormal distribution with a geometric mean of 71.8 nm and geometric standard deviation of 1.3. DLS results for both Ni and Fe nanoparticles were inconsistent with the TEM measurements due to either hydrodynamic diameter effects or aggregation.

The TEM analysis showed that the size distribution for negatively- and positively-charged Ag and negatively-charged Au nanoparticles obeyed a lognormal distribution with geometric means of 43.1 nm, 29.1, and 19.7 nm, respectively, with a geometric standard deviation of 1.31, 1.36, and 1.36, respectively. DLS results for these nanoparticles were inconclusive as results varied with each trial. Zeta potential analysis showed that the negatively-charged Au and Ag nanoparticles were indeed negatively-charged; however, results were inconclusive for the positively-charged Ag. The UV-Vis results showed that the plasmonic nanoparticles were present in the nanocolloids with no impurities; however, the results suggested a broader size distribution for positively-charged Ag nanoparticles compared to negatively-charged Ag nanoparticles, which was inconsistent with TEM analysis which could be due to an insufficient sample size being used for TEM analysis.

The TiRe-LII data collection procedure was described, and datasets collected during the experiments were discussed. Quantitative analyses of LII data obtained from the Ni and Fe nanoaerosols are discussed in the following chapter.

Chapter 5

TiRe-LII results and analysis of LII data of nickel and iron nanoparticles

The data collected using the apparatus described in Chapter 3, from the nanocolloids synthesized following the procedure described in Chapter 4, is analyzed within the TiRe-LII theoretical framework presented in Chapter 2. Figure 5-1 shows a single shot of the raw incandescence signals from the TiRe-LII experiments of Ni and Fe nanoparticles at detection wavelengths of 445 nm and 747 nm.

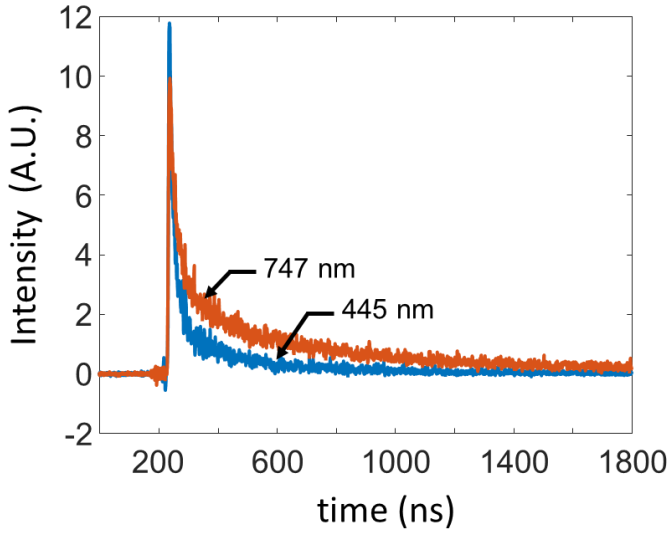

Figure 5-1: Calibrated signals from one shot of LII data. Typical of all data from Ni and Fe nanoparticles.

A fluence study is conducted to investigate the peak temperatures reached by the nanoparticles during laser excitation. Quantities-of-interest (QoIs), including the mean and standard deviation of the nanoparticle size distribution and the thermal accommodation coefficients (TACs) of the nanoaerosols, are inferred from the LII data. The results from the inference method are compared to trends in the literature.

5.1 Fluence study

The variation of the peak temperature of the laser-energized nanoparticles as a function of fluence is investigated by pyrometry. Although it has been established in §2.1.1 that polydisperse sizes in a metal nanoaerosol can complicate the interpretation of the pyrometrically-inferred effective temperatures, this technique can still provide some information about the peak temperature variation as a function of fluence. The pyrometric temperatures were determined with $E(\mathbf{m})_r = 2$ for Ni nanoparticles and $E(\mathbf{m})_r = 1.8$ for Fe nanoparticles as informed from ellipsometry measurements by Krishnan *et al*. [76], which are presented in Figure 2-1. Since the instantaneous incandescence data is a random variable that can be affected by shot noise or low signal-to-noise ratio (particularly towards the end of the signal), outliers are expected in the datasets. A Thompson-Tau outlier removal method [145] was applied to the determined pyrometric temperatures from each shot dataset. Figure 5-2 shows the peak pyrometric temperatures as they vary with fluence. When the prompt signal (0 ns after peak observed incandescence) is used to determine the peak temperatures, the results show that the nanoparticles reach temperatures higher than their boiling point with no visible plateau regime. Although some degree of superheating is expected because the laser heating rate is higher than the evaporation cooling rate (which is dominant at higher temperatures and consequently higher fluences), one would still expect the rate at which the peak temperatures increase with fluence to plateau (*cf.* Figure 2-9). On the contrary, however, the peak temperatures appear to increase linearly with fluence. This suggests a possible corruption of the prompt signal that inflates the observed incandescence and consequently results in high temperatures that do not plateau above the boiling point with increasing fluence. This inflation of incandescence is similar to the excessive absorption phenomenon reported in the literature [24,28,54,55].

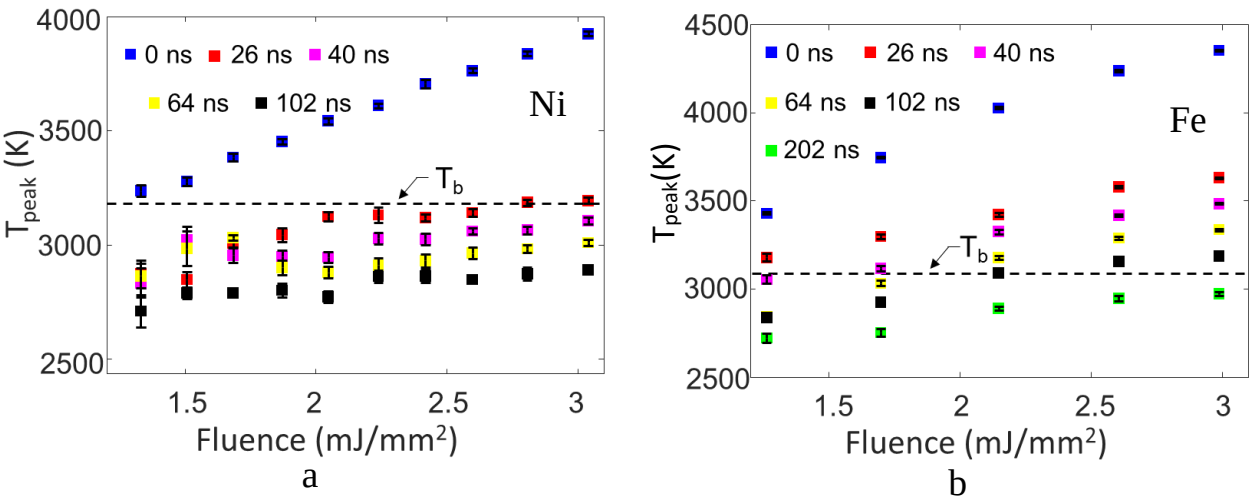

Figure 5-2: Pyrometric peak temperatures of (a) Ni and (b) Fe nanoparticles, aerosolized in Ar, computed using $E(\mathbf{m})_r$ from ellipsometry. Error bars represent 90% confidence intervals**.**

On the other hand, the pyrometrically-inferred temperatures evaluated at various times after the peak signal exhibit the expected behaviour as a visible plateau regime, in the vicinity of the boiling point of the metal, begins to appear. This occurs after a 26 ns delay for Ni nanoparticles and a weak plateau regime at a 102 ns delay for Fe nanoparticles. A similar trend in peak temperatures was observed by Menser *et al*. [28] for Si nanoparticles when the pyrometrically-inferred temperatures versus fluence plateaued at the boiling point of silicon 50 ns after the peak signal.

Using an $E(\mathbf{m})_r$ of unity [26], or close to unity [29], as has been assumed when analyzing previous TiRe-LII measurements on Fe nanoparticles, produces the same trend but, the plateau occurs at much later times after the prompt signal, as shown in Figure 5-3. Since the pyrometric temperatures are supposed to indicate the average internal energy of the nanoparticles, temperatures that exceed 5,000 K, in the case of Fe nanoparticles, are non-physical. It is worth noting that these results for Fe nanoparticles are not consistent with results in the literature, where

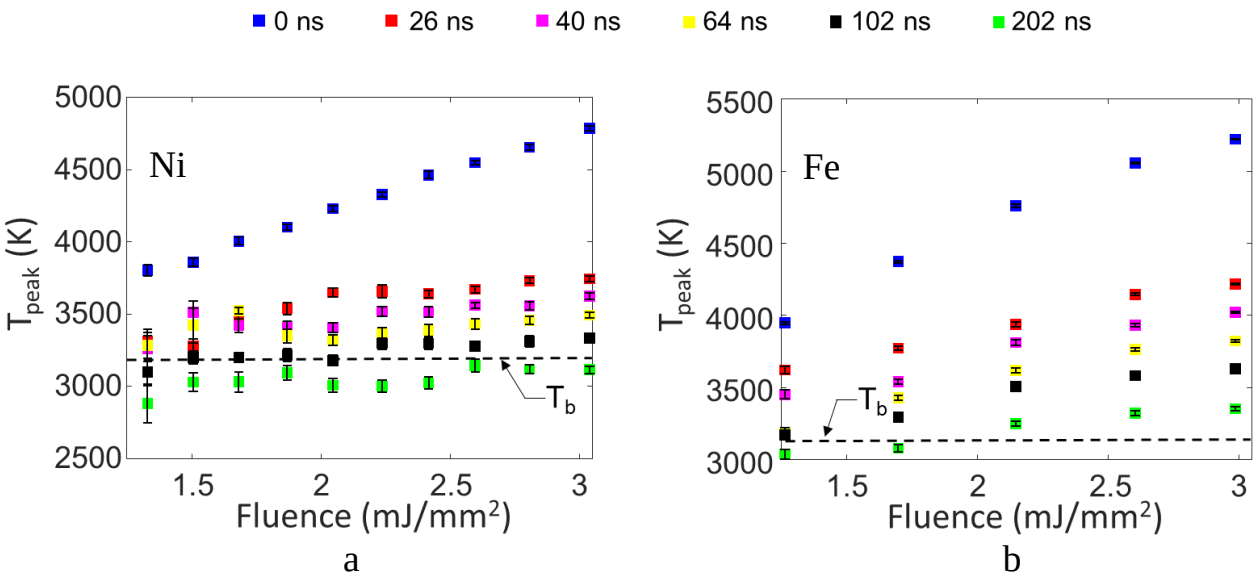

Figure 5-3: Pyrometric peak temperatures of (a) Ni and (b) Fe nanoparticles, aerosolized in Ar, computed using $E(\mathbf{m})_r$ = 1.1. Error bars represent 90% confidence intervals.

pyrometrically-inferred peak temperatures for Fe nanoparticles have been reported below 3,500 K, even when defining $E(\mathbf{m})_r$ = 1 or 1.1 [26,29,42]. One possible reason for the discrepancy with results in the literature is variation in the nanoparticle morphology. Previous studies [26,29,42] performed LII studies on Fe nanoparticles, less than 40 nm in diameter, while in this study, the means of the nanoparticle diameter distribution are greater than 100 nm and 70 nm for Ni and Fe nanoparticles, respectively, with some aggregation present. Although improper calibration can result in erroneously high temperatures, the extensive and rigorous calibration procedure performed in this work, validated by soot data (*cf.* Appendix C.4), suggests that this is not a cause for concern.

It is complicated to compare these absolute temperatures to those computed with $E(\mathbf{m})_r$ from ellipsometry data because the invalidity of pyrometry to determine the effective temperatures of polydisperse metal nanoparticle ensembles renders the concept of an appropriate $E(\mathbf{m})_r$ impracticable.

It is expected that evaporation would be the dominant mode of cooling at higher fluences, which would cause nanoparticle mass loss [24,26], while conductive cooling would be dominant at lower fluences, as discussed in §2.2. Plotting the normalized incandescence signals, from peak incandescence, at various fluences, as shown in Figure 5-4, shows that at short cooling times, there is a rapid signal decay rate with increasing fluence. A similar trend was observed by Kock *et al*. [26] when they irradiated Fe nanoparticles with a 1064 nm laser with fluences ranging from 1.9 mJ/mm^2 – 6.9 mJ/mm^2; they attributed the trend to evaporation at the higher fluences.

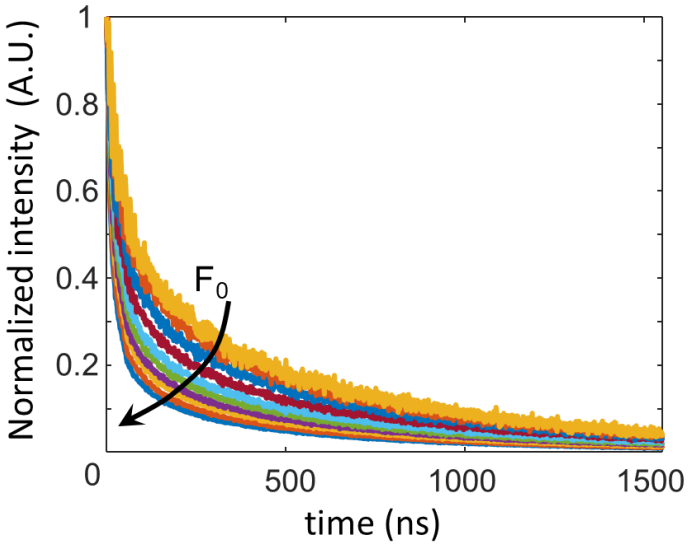

Figure 5-4: Incandescence signals of different fluences at the 747 nm detection wavelength.

The evaporation causes mass loss from the nanoparticle, which reduces the total volume fraction and consequently, should cause a rapid drop in intensity (the observed intensity is proportional to the volume fraction; *cf.* Eq. (2.1)) at higher fluences; note, however, that peak temperature is independent of volume fraction. This finding contrasts with the present results since Figure 5-5(a) shows that the intensity increases with fluence. Integrating the signals at each fluence over time allows for the comparison of the total change in sensitivity to intensity at each fluence [146]. Figure 5-5(b) shows that the integrated intensity does not decrease as expected if there is

mass loss due to evaporation; instead, it increases with fluence. This indicates that the nanoparticle volume fraction is likely not changing and the observed trend in Figure 5-4 is possibly due to another phenomenon of unknown origins that might be corrupting the signal (*cf.* Chapter 6). The additional non-incandescent laser-induced emission seems to affect the prompt signals more significantly at higher fluences, which causes the observed apparent evaporation, and consequently, high pyrometrically-inferred temperatures. The artifacts that affect the prompt signals affect the inference of the QoIs at higher fluences, as discussed in §5.3.

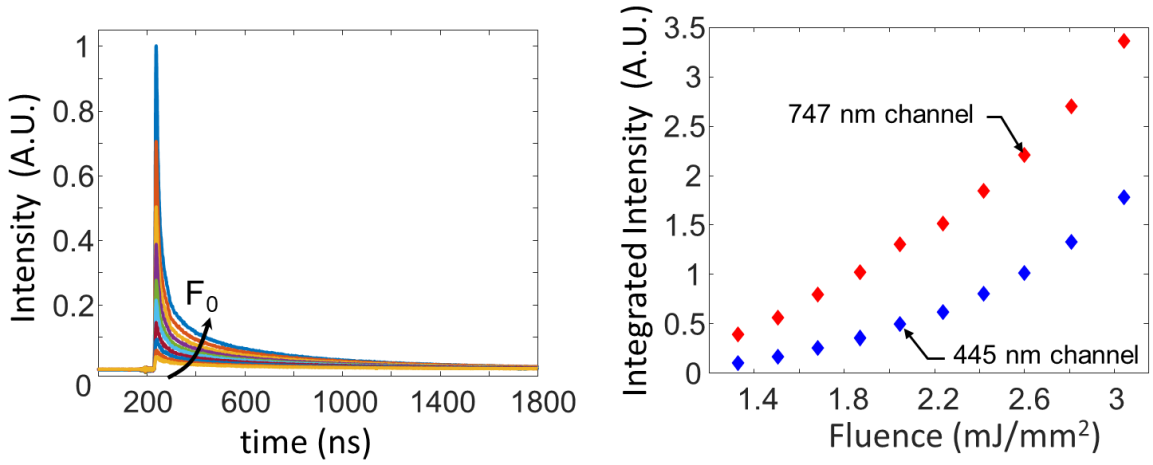

Figure 5-5: (a) Signal intensity profiles at each fluence on the 747 channel (b) Total intensity at each fluence at both detection wavelengths.

5.2 Inferring QoIs from TiRe-LII data

The analysis aims to infer the QoIs from experimental data using the Bayesian framework (*cf.* §5.2.2). The QoIs in this work are the nanoparticle size distribution parameters (mean and standard deviation) and the TACs, α, of the nanoaerosols. The following subsections describe the analysis and inference procedure.

5.2.1 TiRe-LII model modification

In the LII literature, QoIs are commonly inferred by regressing the modelled pyrometric temperature history to the experimentally-inferred pyrometric temperature history [26,28,29,147]. However, the effective temperature inferred from pyrometry is likely not representative of the temperature of the nanoparticle ensemble (*cf.* §2.1.1 and §2.2.2) and consequently does not provide accurate and physically significant information about the internal energy of the nanoparticle ensemble. Although it has been suggested that the temperatures can still be regressed as long as the pyrometric temperatures are inferred from both experimental and modelled incandescence [59], a more robust alternative is to regress the modelled incandescence signal to the experimental incandescence data since it avoids pyrometry entirely. This involves modelling the temperature history (both laser heating and subsequent cooling) of the nanoparticle ensemble with the full heat transfer submodel, and then determining the incandescent emission with the spectroscopic submodel. However, modelling the temperature history of the nanoparticles, as shown in Figure 5-6, with similar values of experimental fluences and a Gaussian laser profile (*cf.* Figure 3-3), shows that the nanoparticles do not reach a sufficient temperature to produce the detected LII signals.

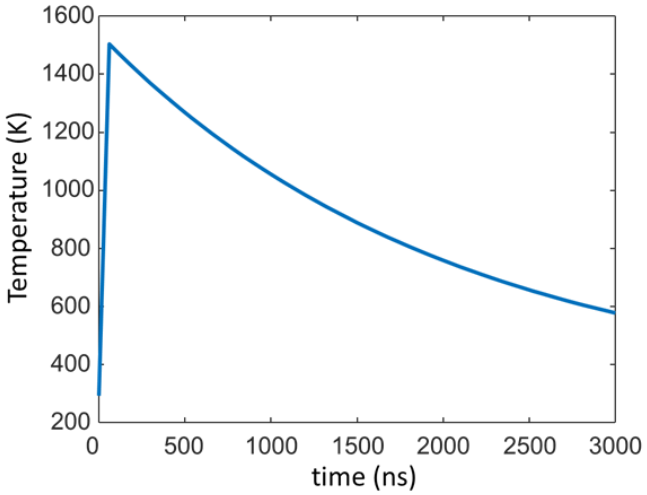

Figure 5-6: Modelled temperature profile of Ni nanoparticles.

This indicates that there is some mechanism that enhances the absorption cross-section of the nanoparticles at the laser fluence beyond what is expected based on Mie theory and the refractive index of the bulk material. A similar result was found by Talebi Moghaddam *et al*. [59] when they simulated the laser heating of Fe nanoparticles [59]. To overcome the uncertainty introduced by unknown sources of excessive absorption, only the cooling of the nanoparticles is modelled, following Refs. [28,29]. Because the peak temperature from which the nanoparticles cool is unknown, it was included as an additional parameter to infer (i.e. a nuisance parameter[21], *cf.* Appendix A.1.2) during the inference procedure. However, this treatment assumes that all nanoparticles reach the same peak temperature from where they cool, which is not the case (*cf.* § 2.2.2), and will, consequently, introduce inaccuracies when interpreting results for a polydisperse aerosol [59]. The spatially non-uniform laser profile (*cf.* Figure 3-3) will also cause temperature non-uniformities within the probe volume due to the non-uniform heating of the nanoparticles. Regressing the incandescence data reduces the uncertainty in inferred quantities introduced by noise, compared to regressing the pyrometric temperature history because noise, present in the raw incandescence data, is amplified through pyrometry due to the dependency on the ratio of the noisy signals.

It is computationally-intensive to infer four QoIs (mean, standard deviation, TAC, and peak temperature) from the data by dynamically solving the incandescence model of a polydisperse nanoaerosol with the heat transfer and spectroscopic submodels, while evaluating absorption efficiencies with Mie theory. A 4D lookup table of the modelled incandescence at each time step was generated to overcome this challenge, which reduced modelling time by a factor of five. The lookup table was generated by solving the spectroscopic and heat transfer submodels at each time

[21] Nuisance parameters are unknown model parameters that are not of interest and hence need to be inferred along with the QoIs.

step, for a variety of nanoparticle diameters, TACs, and peak temperatures. All material properties used in the model are temperature-dependent (*cf.* Chapter 2).

5.2.2 Inference procedure and considerations

The Bayesian inference method is used to infer the QoIs. In the Bayesian framework, the unknown solution vector of QoIs , **x**, nuisance parameters, **θ**, and the data vector, **b** (incandescence signals) are visualized as random variables that obey probability density functions (pdfs) related by the Bayes' equation [148]

$$p(\mathbf{x},\boldsymbol{\theta}\,|\,\mathbf{b}) = \frac{p(\mathbf{b}\,|\,\mathbf{x},\boldsymbol{\theta})\,p_{\mathrm{pr}}(\mathbf{x})\,p_{\mathrm{pr}}(\boldsymbol{\theta})}{p(\mathbf{b})}, \tag{5.1}$$

where $p(\mathbf{b}|\mathbf{x},\boldsymbol{\theta})$ is the joint likelihood pdf of the observed data, **b**, occurring for a hypothetical set of model and nuisance parameters, **x** and **θ** respectively, $p(\mathbf{x},\boldsymbol{\theta}|\mathbf{b})$ is the joint posterior pdf of **x** and **θ** being the model solutions given the data set **b**, $p_{\mathrm{pr}}(\mathbf{x})$ and $p_{\mathrm{pr}}(\boldsymbol{\theta})$ are the pdfs of the prior knowledge of **x** and **θ** respectively, and $p(\mathbf{b})$ is the evidence of all possible solutions occurring and is used to scale the posterior pdf to satisfy the Law of Total Probability. Details of the Bayesian framework are presented in Appendix A.

The priors for the mean and standard deviation of the nanoparticle size distribution were determined from *ex situ* TEM analysis. Gaussian priors, with a mean equal to the mean from *ex situ* analysis and a standard deviation that was 20% of the mean value, were used for μ, μ_{g}, σ, and σ_{g}. A normal and lognormal pdf were used to model the polydisperse size distribution of Ni and Fe nanoparticles, respectively, as informed from the *ex situ* TEM analysis. Arithmetic means, μ, and standard deviations, σ, are inferred for the diameters of Ni nanoparticles, and geometric means, μ_{g}, and standard deviations, σ_{g}, are inferred for the diameters of Fe nanoparticles. A uniform prior between zero and one was used for α. Priors for T_{peak} were chosen as Gaussian distributions with

a mean equal to the boiling point of the metal, and a standard deviation of 20% of the mean value (signal delay to the plateau at the boiling point was incorporated, *cf.* Figure 5-7). Table 5-1 summarizes priors used for inference.

The model fit to the data was carried out using the hybrid genetic algorithm minimization scheme implemented in MATLAB® [107] using the "*ga*" function (*cf.* Appendix B.3) and refined by an interior point minimization algorithm using the "*fmincon*" function. Upper and lower bounds were defined for each QoI to minimize the search space. This can be akin to adding a uniform prior to each QoI.

Table 5-1: Priors used in Bayesian inference.

QoI	**Priors**
μ_*	$\mathcal{N}\left(\mu_{\text{TEM}},\ 20\%\ \mu_{\text{TEM}}\right)$
σ_*	$\mathcal{N}\left(\sigma_{\text{TEM}},\ 20\%\ \sigma_{\text{TEM}}\right)$
α	$\mathcal{U}\left(0,\ 1\right)$
T_{peak}	$\mathcal{N}\left(T_{\text{b}},\ 20\%\ T_{\text{b}}\right)$

*same priors used for μ_{g} and σ_{g}.

The Thompson-Tau outlier removal method [145] was applied to the datasets at each time step. To estimate the covariance of the shot data, each removed outlier was resampled by bootstrapping with replacement resampling technique [149], implemented in MATLAB®[107] with the "*bootstrp*" function. The covariance matrix was diagonally dominant (i.e. high variances), which is expected since the noise is dominated by photonic shot noise introduced by the PMT detectors and affects each measurement independently (i.e. independently distributed data). Because there were high covariances close to the diagonal, which is possibly due to the Q-switch noise from the

laser head or shot-to-shot variation in laser fluence, the covariance matrix was approximated with ten covariances on either side of the variance diagonal (*cf.* Appendix E.4).

Considering the large pyrometrically inferred peak temperatures, which indicate prompt signal corruption by non-incandescent laser-induced emissions, all data before the delay time at which the plateau regime occurs are excluded from the inference process; consequently, the peak temperature determined at a specified time delay becomes a model peak temperature, $T_{\text{peak}}^{\text{mod}}$, that serves as an initial condition for the heat transfer model, from which the nanoparticles cool. Figure 5-7 compares the model estimate with and without the prompt signal.

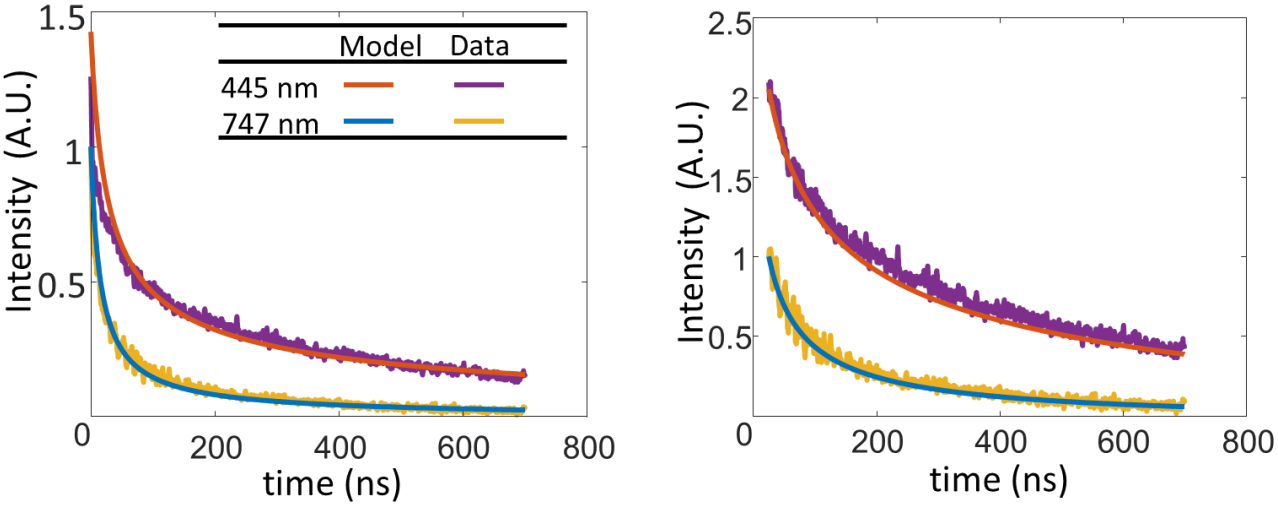

Figure 5-7: Comparing model fit to the (a)Prompt (b)Delayed signal.

The TiRe-LII model generally fitted better to LII datasets for Ni nanoaerosols than for Fe nanoaerosols, even after eliminating all data before the appropriate delay time. This occurred when $E(\mathbf{m})_r$ is assumed to be unity and also when it is calculated from ellipsometry-derived refractive indices for the liquid metals. The fit was particularly poor at later cooling times for possible reasons such as aggregation, which is discussed further in §5.3.3.

5.3 Results of inferred QoIs

5.3.1 Inferring the size distribution

After applying the model modifications and inference method, the QoIs were inferred from the LII data of all nanoaerosols. Although some of the prompt signals have been eliminated, the effects of unknown sources of non-incandescent laser-induced emission (LIE) may still persist (though at lower magnitudes) and will consequently affect the inference of the size distribution because of the regression that occurs towards the peak of the signal. In addition, the assumption of uniform initial temperature is likely to cause additional variation in inferred results. The combination of these effects may explain the discrepancy between inferred results and TEM analysis, shown in Figure 5-8. For both Ni and Fe nanoparticles, the trend shows that the means inferred at lower fluences, across all aerosols, closely agree with *ex situ* TEM measurements, while it deviates from *ex situ* measurements at higher fluences, with a greater spread in the results. The inferred standard deviations at lower fluences are larger than *ex situ* measurements in the case of Ni nanoparticles and smaller in the case of Fe nanoparticles, and generally decrease to a lower bound with a greater spread in the results in the case of Ni nanoparticles.

The discrepancy between the TEM results and inferred results, and the variability of the inferred results, increases at higher fluences, possibly due to signal corruption that affects the data at such fluences. The model does not capture the rapid drop in intensity caused by the signal corruption even after some of the prompt signals have been excluded from the inference. Some of the observed trends in the inferred results as a function of fluence can also be attributed to the apparent evaporation at higher fluences. At the lower fluences, the size distribution is expected to remain unchanged because there is no apparent mass loss due to evaporation, while the opposite is expected at higher fluences [150]. Additionally, the change in diameter is larger for much larger

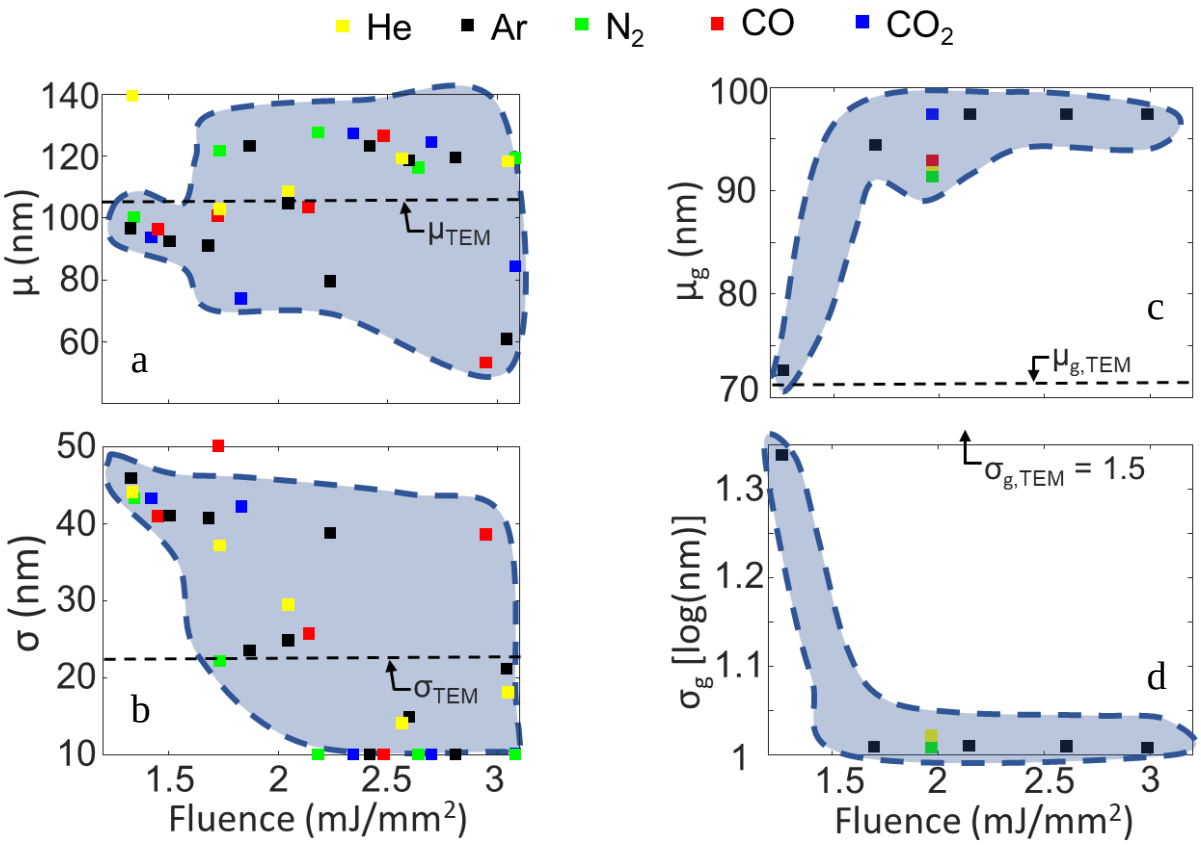

Figure 5-8: Inferred size distribution parameters. (a) The mean and (b) standard deviation for Ni nanoparticles, and (c) the geometric mean and (d) geometric standard deviation for Fe nanoparticles. Shaded areas are drawn to guide the eye.

nanoparticles than for smaller ones, resulting in a narrower size distribution towards the end of the laser pulse [150]. One other possibility for inferring a monodisperse nanoaerosol distribution (i.e. small standard deviations) is the effect of signal corruption that causes apparent evaporation at higher fluences. It could very well be that this phenomenon has a highly non-linear variation with diameter such that the emissions from a narrow diameter size class are responsible for most of the observed signals at higher fluences.

The mean of the particles in the nanoaerosol should reduce with increasing fluence due to mass loss as the pdf of the size distribution narrows. Therefore, the observed increase in estimated means with fluence for most of the Ni nanoparticles, which is more apparent for Fe nanoparticles, is likely

non-physical and could also be due to the unknown source of signal corruption that increases with fluence.

5.3.2 Inference of the model peak temperature

Figure 5-9 shows the inferred model peak temperatures. It should be noted that these temperatures are meant to indicate a mean temperature/internal energy of the nanoparticles in the probe volume, but increasing polydispersity reduces the physical relevance of this interpretation. Figure 5-9 shows that, although the prompt signals have been eliminated, the inferred model peak temperatures for the Ni nanoparticles remain above the boiling point of the metal with a general increase in temperature with some plateau appearing around 2.4 mJ/mm^2. In contrast, the inferred model peak temperatures for the Fe nanoparticles are below the boiling point of the metal with a similar increase in temperature with an apparent plateau around 2.6 mJ/mm^2. The inconsistency with the boiling point, which partly manifests as superheating, is expected since heat is being added to the nanoparticle by the laser faster than it can be removed by evaporation under such non-equilibrium conditions (*cf.* Figure 2-9). The results from Ni nanoaerosols suggest that there still some mechanism inflating the absorption cross-section of the nanoparticles at later cooling times, i.e. excessive absorption, or non-incandescent emissions are corrupting the signal, and the extent to which any of these affect the inference is reduced for Fe nanoparticles probably because more of the prompt signal was eliminated from the inference data. Furthermore, the inferred model peak temperatures for Ni-Ar nanoaerosol, computed at 26 ns after the peak, are higher than the pyrometrically-inferred peak temperatures at the same delay after the peak, and those of Fe-Ar nanoaerosol, computed at 102 ns after the peak, are lower than the pyrometrically-inferred peak temperatures at the same delay after the peak (*cf.* Figure 5-2 and Figure 5-3). This inconsistency provides additional evidence that the pyrometrically-inferred temperature does not provide a true

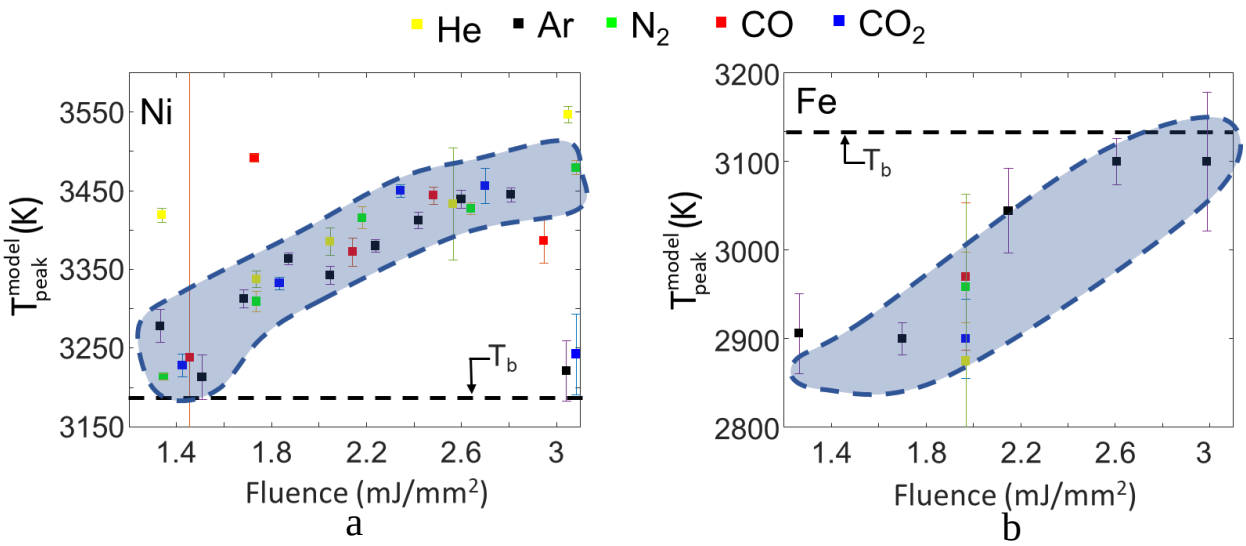

Figure 5-9: Inferred model peak temperatures of (a) Ni nanoparticles and (b) Fe nanoparticles. Error bars represent two standard deviations of the mean. Shaded areas are to guide the eyes.

indication of the internal energy of a polydisperse metal nanoparticle ensemble.

The inferred model peak temperatures are considered more accurate than the peak temperatures found from pyrometry because the spectroscopic submodel used to model the incandescence signals accounts for the effect of polydispersity and uses Mie theory (*cf.* §2.1), which is not the case for pyrometrically-inferred temperatures (*cf.* §2.1.1).

It is also worth noting that, although the inferred model peak temperatures of the different nanoaerosols follow the same general trend with fluence, there is some variability, which should not be the case because laser absorption by the nanoparticles is independent of the surrounding motive gas, hence, nanoparticles should reach the same peak temperature in all motive gases. The observed variability might be due to different levels of noise in the datasets, causing the minimization algorithm to produce different results for the model peak temperatures in different motive gases, which are mostly within the estimated uncertainties. In some cases, the displayed

error bars are small, while the inferred result seems to be an outlier; this occurrence is probably due to non-linear minimization concerns discussed further in §5.4.

Because higher pyrometric temperatures were inferred using an $E(\mathbf{m})_r$ of 1.1, as previous studies have done, but with similar trends as with $E(\mathbf{m})_r$ informed from ellipsometry, it is expected that the trends in these results will also be apparent but at higher temperatures when the absorption efficiencies are computed according to the Rayleigh approximation with $E(\mathbf{m})$ at 445 nm being 1.1 times greater than at 747 nm. However, the Rayleigh approximation would introduce modelling error (*cf.* §2.2.2), which is avoided in this inference method based on absorption efficiencies from Mie theory.

5.3.3 Inferring the Thermal Accommodation Coefficient

The inferred TACs provide an opportunity to directly compare the results of the modified inference method to results from literature because the TAC holds information about the physics of the nanoparticle-gas molecule interaction, as discussed in §2.2.4. Unlike the size distribution, which is mostly informed from the evaporation model/regime ($q_{\text{evap}}(t,\ d_{\text{p}}) \propto d_{\text{p}}^2$), the conduction model/regime provides information for both the size distribution and TAC ($q_{\text{cond}}(t,\ d_{\text{p}}) \propto \alpha d_{\text{p}}^2$); hence the TAC is inferred from data at later cooling times where conduction is the dominant mode of cooling modelled in the free molecular Knudsen regime, where $Kn >> 1$ (*cf.* §2.2.4).

As discussed in §2.2.4, conduction in the free molecular regime (FMR) occurs as gas molecules accommodate energy from the nanoparticle through normal- and tangential-translational, rotational, and vibrational modes, although with minimal accommodation in the vibrational modes. Most of the surface energy is accommodated into the normal-translational mode of the gas molecule, which increases with an increase in specific mass, $\mu = m_{\text{g}}/m_{\text{p}}$, followed by more

accommodation in the rotational mode of polyatomic gas molecules, which increases with an increase in structural-anisotropy, and least in the tangential-translational mode, which also increases with increase in structural-anisotropy but to a lesser extent [43]. Therefore, the average TAC should increase with specific mass, with more structurally-complex gas molecules having lower TACs, as seen in Figure 5-10, indicating less energy accommodation in the internal rotational and vibrational modes of polyatomic gas molecules. However, molecular dynamics (MD) simulations of the Ni-Ar nanoaerosol by Daun *et al*. [44,45] report a TAC that is unusually higher than other metal nanoparticle-gas molecule systems for reasons further discussed later in this section.

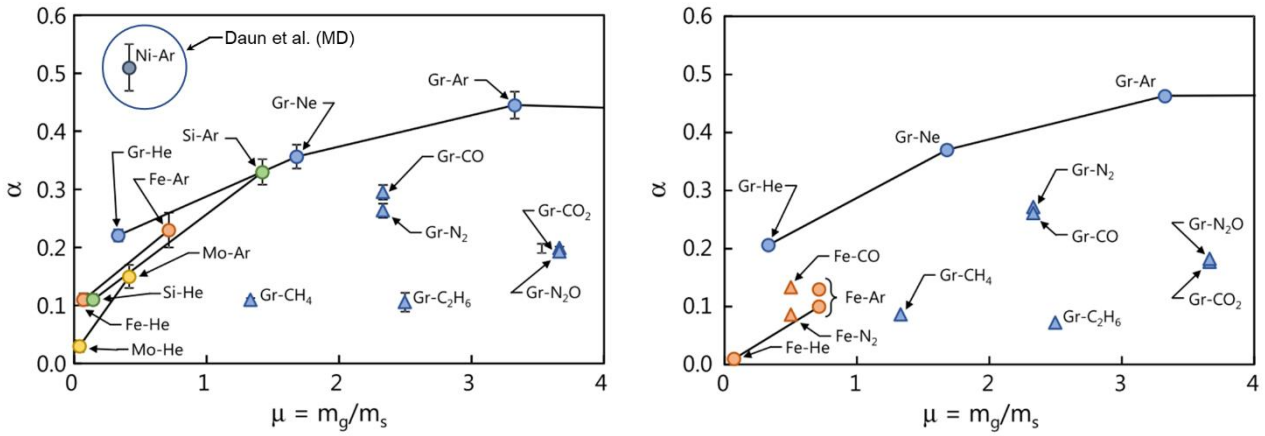

Figure 5-10: Trends of TACs from various nanoaerosols inferred from (a) MD simulations (Daun *et al*. [44,45] has been labeled) and (b) experiments. Modified from Ref. [47].

However, upon determining *Kn* for the size classes of the synthesized nanoparticles, based on the temperature and pressure of the motive gases and their mean free paths (MFP) [151], as shown in Table 5-2, conduction likely occurs within the transition regime, where $Kn \approx 1$, specifically ~ $0.01 < Kn < \sim 10$ [91]. In the transition regime, the rate of conduction heat transfer is controlled by both the nanoparticle-gas molecule intermolecular interactions and collisions, as in the free molecular regime, and the molecule-molecule collisions, governed by the macroscopic Fourier heat conduction law, as in the continuum regime [91]. Therefore, not accounting for conduction in

this regime by defining one parameter, α, to account for conduction efficiency from the combined effects of the continuum and free molecular regimes will introduce modelling error and will likely inflate the inferred results for TACs. It is worth noting, however, that practical results for TAC have been inferred with conduction modelled in the free molecular regime when the size classes of the nanoparticles suggested conduction in the transition regime [29].

Table 5-2: Knudsen number of the different motive gases used at T_g = 273 K and P_g = 101 kPa.

Gases	Knudsen number*	
	Ni (μ_p = 105.6 nm)	Fe (μ_p = 71.8 nm)
He	0.47	0.69
Ar/N_2/CO	0.23	0.34
CO_2	0.13	0.19

*refer to Appendix D.1 for evaluation.

Figure 5-11 (a) shows the inferred TACs for all Ni nanoaerosols, and Figure 5-11 (b) shows the inferred TACs for all Fe nanoaerosols and how they compare to results from the literature. The presented TACs are averaged from inferred results at low fluences, and the error bars are estimated from the uncertainties of the individual inferred results (*cf.* Appendix D.2). The results, as shown in Figure 5-11, follow the expected trend in specific mass but not in structural-complexity since the TAC from the Ar nanoaerosol is lower than the CO and CO_2 nanoaerosols.

When comparing with the TACs for Fe nanoaerosols from literature, the TAC for the Fe-He nanoaerosol lies at the lower end of the range of literature values, while the TAC for the Fe-Ar nanoaerosol lies well within the range, and TACs from the Fe-CO, Fe-CO_2, and Fe-N_2 nanoaerosols predict a significantly higher TAC than earlier experimental studies. This is an indication that the inferred TACs overestimate the true TACs for the polyatomic nanoaerosols, while estimates for monoatomic gases are generally consistent with MD and experimentally-derived results presented in the literature. The estimated TAC of 0.27 for the Ni-Ar nanoaerosol is

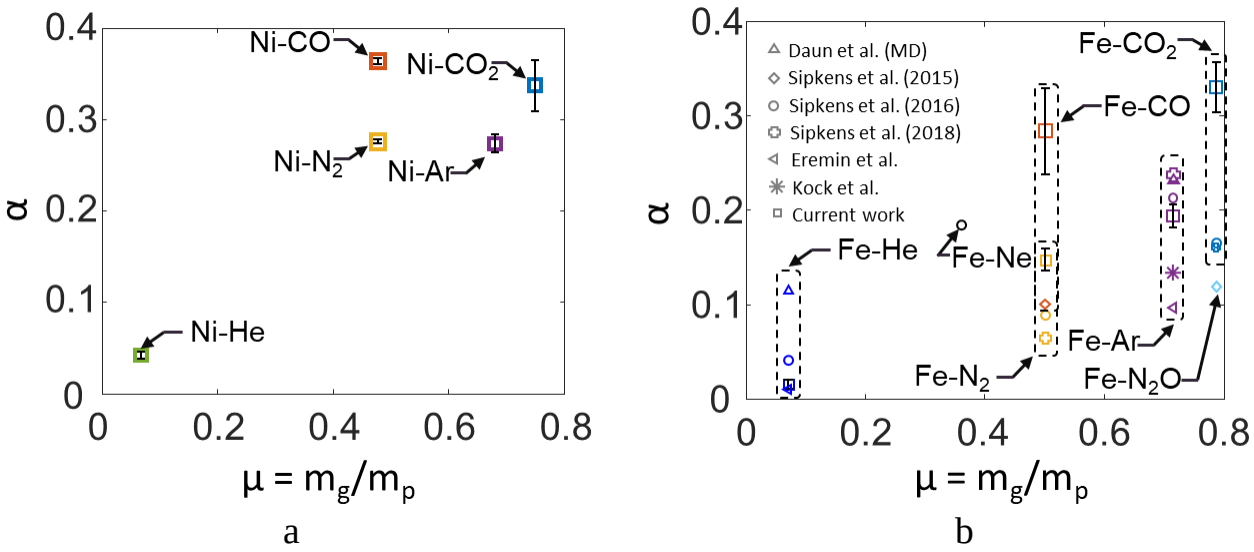

Figure 5-11: Inferred TACs (α) for (a) Ni and (b) Fe nanoparticles [26,29,42,46–48]. Error bars represent one standard deviation of the mean.

lower than the MD simulation estimate of 0.51 by Daun *et al*. [44,45] but comparable to literature results[22] for Fe-Ar nanoaerosols that report TACs between 0.1 – 0.24. One possible reason for the inconsistency with MD simulation results by Daun *et al*. [44,45] is the Casimir-Polder retardation effects employed in the ab initio density functional theory (DFT) calculations used to model the gas/surface interaction, which causes a much deeper potential well when compared to other gas/surface potentials that are mainly due to dispersive effects [46]. The Casimir-Polder effect is a predicted attractive force that results when the characteristic wavelength of an electric field, resulting from a dipole moment in a particle, is smaller than the spacing between the particle and an adjacent particle, which causes wave retardation. When there are more than two particles, multiple scattering occurs. The combination of wave retardation and multiple scattering in a system of many particles results in an attractive force [152,153]. The dispersive effect is an

[22] Note that the different literature studies made different assumptions and hence have different models for free molecular conduction.

attractive force (London dispersion force) that occurs between systems of transient electrons that induce a temporary dipole moment [154].

In the transition regime, heat conduction is controlled by both gas molecule-nanoparticle collisions, quantified by the averaged TAC from each accommodation mode, and macroscopic heat conduction by the gas molecules, quantified by the thermal conductivity of the gas. The TAC is expected to vary in the same way in the transition and free molecular heat conduction regime since it is still dependent on metal surface-gas molecule collision. However, modifying the heat conduction model to account for heat conduction in the continuum regime would require a transition regime conduction model that depends on the thermal conductivities and molecular mean free paths of the gases [91]. Consequently, not accounting for these dependencies and defining one parameter, α, to account for all such dependencies will result in model errors. Although it is not clear how this modelling error manifests in the inferred TACs, it could be responsible for the overestimation of TACs for the polyatomic nanoaerosols since the polyatomic gases generally have higher thermal conductivities [155]. Based on a plot of a Nusselt number, *Nu* (a dimensionless representation of the heat, *q*, conducted from the nanoparticle [156]) versus *Kn*, as shown in Figure 5-12, the modelling error is expected to be significant since there is as much as a 50% difference between *Nu* modelled in the transition regime compared to the free molecular regime at $Kn \approx 0.1$.

The effect of aggregation of the nanoparticles, which is more significant for Fe nanoparticles (*cf.* Figure 4-5), will cause the *Kn* to be even smaller, consequently causing conduction to occur closer to the continuum regime. This is a possible reason as to why the model does not fit well to the LII data from the Fe nanoaerosol at later times.

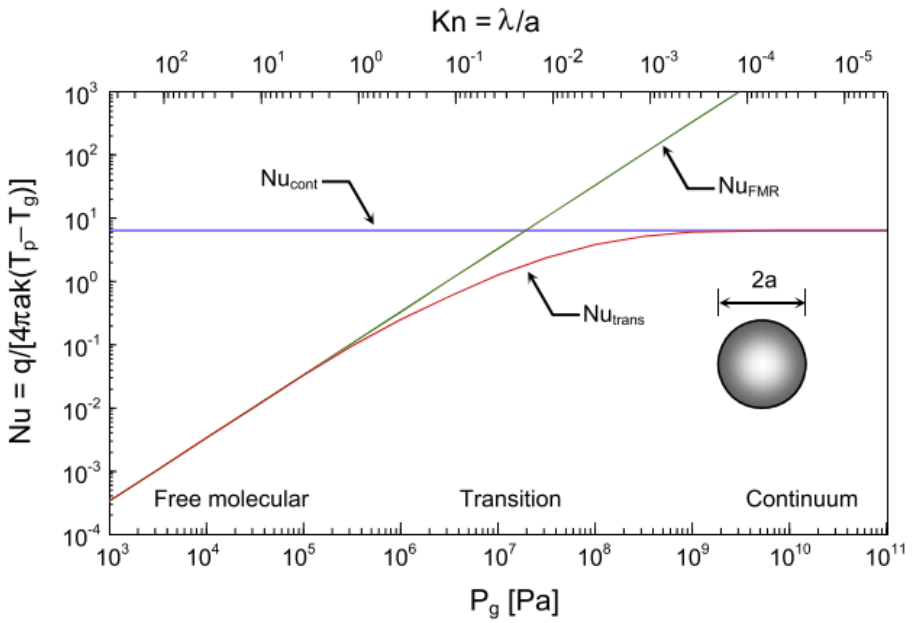

Figure 5-12: Regimes of heat conduction from a nanoparticle [156].

Another point worth noting is that polyatomic gas molecules with similar specific masses are expected to have similar TACs as determined from experimental data of soot aerosols [56] and Fe nanoaerosols [47] (*cf.* Figure 5-10), hence, TACs for CO and N_2 aerosols are expected to be approximately similar [47]. Both these motive gases have similar mean free paths [157] and thermal conductivities [155] and hence are expected to conduct heat in similar amounts even in the transition regime (i.e. same amount of model error introduced in the inference). However, as seen from Figure 5-11, the TACs for both CO and N_2 aerosols are different for both the Ni and Fe nanoaerosols. This discrepancy could be attributed to the strong affinity between the carbon and metal atoms, which manifests as a deeper potential well[23] [158], compared to other metal atom-gas atom systems [48]. Hence, this suggests that TACs do not depend on molecular mass and structure alone but also on constituent atoms.

[23] For this reason, both Fe and Ni nanoparticles have been used as catalysts for the fabrication of carbon nanotubes [182].

The aerosolization process might also add uncertainty to the data collected for different motive gases. Since the amount of nanocolloid aerosolized is dependent on the viscosity of the motive gas (*cf.* §3.2), there is a possibility that there are more nanoparticles per atomized droplet of solvent, which would aggregate during the drying process and skew the final size distribution of nanoparticles in the probe volume depending on the motive gas used.

Similar trends in the TACs are also observed when the inference method by Sipkens *et al*. [29] was replicated, although with different absolute values. In their inference method, the LII model was regressed to the pyrometrically-inferred temperature histories evaluated with $E(\mathbf{m})_r = 1.1$.

Liu *et al*. [91] assessed available methods for modelling the transition conduction regime and provided useful insights into the modelling considerations. Modelling aggregates becomes even more complicated since it is not clear what characteristic length can be used. Liu *et al*. [70] use the concept of an equivalent sphere, whose surface area is such that it has the same heat conduction rate with the surrounding gas as that of the aggregate, to determine the characteristic length. Incorporating the transition regime conduction model is recommended as future work.

Results, presented in Figure 5-13, from another TAC inference method, developed by Daun *et al*. [56], were compared to results from Figure 5-11. In this approach, they inferred the TAC of soot nanoaerosols from low fluence data, where conduction is the dominant cooling mechanism, by regressing the heat transfer model, which considered conduction cooling only, to the exponential pyrometric temperatures (*cf.* Appendix D.3 for details). While in this work the nanoparticles reach high temperatures with apparent evaporation occurring, this approach can be extended to this data set by regressing only the conduction cooling region (modelled in the free molecular regime) of the pyrometric temperature histories, which occurs at much later cooling times (details of this analysis procedure is provided in Appendix D.3). Using this approach to infer

the TACs, requires knowledge of the nanoparticle diameters. Although the nanoparticles have a wide size distribution, the nanoaerosol is approximated as monodisperse with a diameter equal to the mean from *ex situ* measurements. The TACs inferred from this approach, shown in Figure 5-13, show that the expected trend in the TACs when conduction occurs in the free molecular regime, where monoatomic gas molecules accommodate energies more efficiently than polyatomic gas molecules (i.e, TACs for Ar aerosols are higher than that of CO and CO_2 aerosols). However, Ni-CO and Ni-N_2 nanoaerosols still have dissimilar TACs.

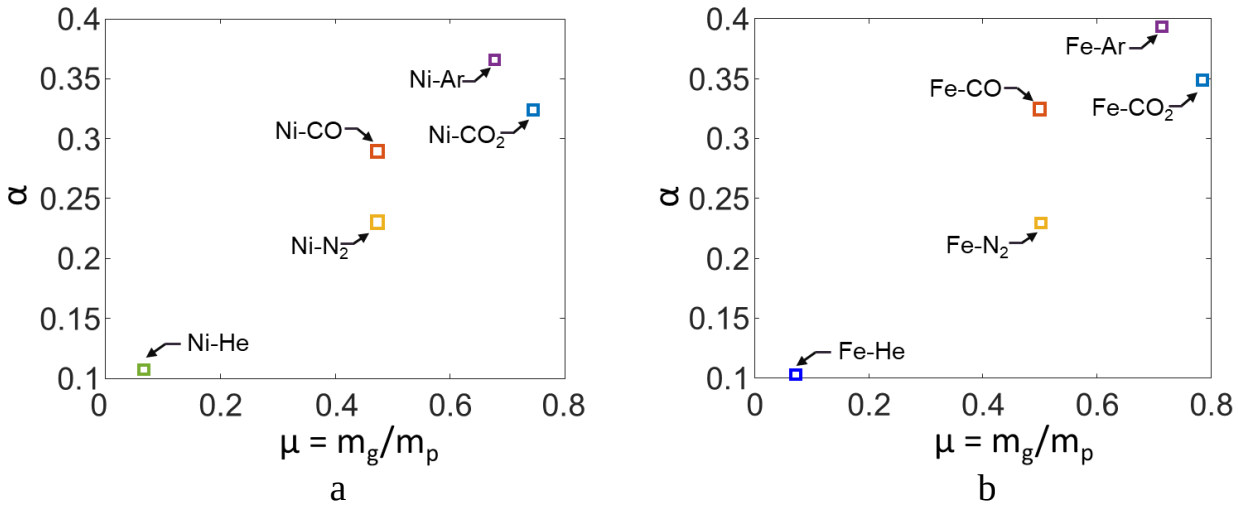

Figure 5-13: Inferred TACs (α), using conduction regime approximation, for (a) Ni and (b) Fe nanoparticles.

It should be noted that this approach is only used to show the trends in TACs; the modelling errors/approximations, which include the monodisperse approximation and the assumption that conduction occurs in the free molecular regime, are expected to affect the absolute values. Although the expected trend is achieved with this approach, its application to the current TiRe-LII data is subjective and sensitive to uncertainties in that it is not clear what section of the data is majorly conduction cooling without interference from evaporation or polydispersity effects (*cf.* Appendix D.3). Additionally, at lower fluences, the shot noise significantly affects the data due to

the low signal to noise ratio, which sometimes affected the inferred TACs, resulting in trends that were not consistent with Figure 5-13. An advantage of this approach, however, is that it is less sensitive to the uncertainties associated with the peak temperatures.

5.4 A note on non-linear minimization

The results have been inferred by regressing the TiRe-LII model to the LII data, within the Bayesian framework, using non-linear minimization algorithms, including genetic and interior point algorithms. The regression, using these minimization algorithms, is based on the assumption that the solution space is convex and, as such, would have one global minimum, which is a generally accepted assumption in the literature. However, the modifications and model errors introduced into the inference could cause several local minimums or a shallow global minimum (ill-posed), which could, at times, result in inferred outliers similar to those of Figure 5-9(a). Details of the non-linear minimization algorithms used in this work are presented in Appendix B. A Markov Chain Monte Carlo (MCMC) procedure [148] can sample the solution space to confirm that only the strongest global minimum parameters have been inferred.

5.5 Summary

This chapter analyzed the data from TiRe-LII experiments on Ni and Fe nanoaerosols. A fluence study showed that peak pyrometric temperatures calculated with the prompt LII signals were higher than the boiling point of the metal, and delayed signals produced temperatures that plateaued near the boiling point of the metal. The high temperatures were attributed to possible corruption of the prompt signals that inflate the observed incandescence, which was confirmed when the sensitivity to intensity did not drop, albeit a plot of the normalized incandescence signals at varying fluences showed apparent evaporation at higher fluences.

The inference procedure used involved regressing the heat transfer and spectroscopic submodels to the incandescence data from peak incandescence at a prescribed delay. The Bayesian inference framework was used to infer the QoIs, which included the mean and standard deviation of the nanoparticle size distribution, the thermal accommodation coefficient (TAC) of the nanoaerosols, and a model peak temperature that functioned as a nuisance parameter.

Results showed that QoIs of the size distribution inferred at lower fluences agreed closely with *ex situ* measurements for the size distribution. The inferred model peak temperatures for Ni nanoparticles were higher than the boiling point of the metal with an apparent plateau around 2.4 mJ/mm^2 and those of Fe nanoparticles were lower than the boiling point of the metal with an apparent plateau around 2.6 mJ/mm^2. Results for Ni nanoparticles were much higher than what is predicted by the heat transfer model even after eliminating some of the prompt signals, indicating the possibility of unknown sources of signal corruption, which were present to a lesser extent in the Fe nanoparticle data because more of the prompt signal was eliminated. The inferred results of the model peak temperatures were found to be inconsistent with the pyrometrically-inferred temperature, at the same delay, which provided additional evidence that pyrometrically-inferred temperatures do not provide a true indication of the internal energy of a polydisperse metal nanoparticle ensemble.

The inferred TAC for the Ni-Ar nanoaerosol was lower than MD simulation results from literature and comparable with TACs of the Fe-Ar nanoaerosol. However, trends in the results showed that the inference method overestimated the TACs for the polyatomic gas aerosols and was attributed to modelling conduction in the free molecular regime when conduction is most likely happening in the transition regime, based on the size classes of the synthesized nanoparticles. Similar trends in the TAC were observed when the inference method by Sipkens *et*

al. [29] was replicated. Another TAC inference method used by Daun *et al*. [56], produced the expected trend in TACs, although the application of this method to the current LII data was found to be subjective and sensitive to uncertainties. Some of the unknown sources of observed emissions that could be corrupting the prompt signals are investigated through qualitative analysis of LII data from Ag and Au nanoparticles and discussed in the following chapter.

Chapter 6

TiRe-LII measurements on aerosols of Silver and Gold nanoparticles

Results from the analysis of LII data of Ni and Fe nanoparticles presented in Chapter 5 indicate possible corruption of the prompt signal, which several other studies have also observed [24,29,52,54–57]. Sources of the corruption have been attributed to several phenomena, including anomalous incandescence behaviour, where radiation is emitted as nanoparticle clusters undergo micro explosions following thermal excitation by the laser pulse [52], and laser-induced Bremsstrahlung, where the incandescence signal is contaminated with emission from a vaporized plasma that surrounds the nanoparticle [53]. It is challenging to investigate the isolated effect of many of the potential sources of signal corruption since the observed signal is a combination of any possible sources of corruption masked within the incandescence emitted by the laser-heated particles. However, Ag and Au nanoparticles provide an opportunity to isolate some of these signal corruption because they should not heat up more than 100 K when irradiated with a 1064 nm laser, as predicted by the TiRe-LII heat transfer model [59] due to the low absorption at the laser wavelength [39], consequently, minimal to no incandescence should be observed. Hence, any observed LII signal from these nanoparticles must be of non-incandescent origins.

Other TiRe-LII studies have observed signals from Ag nanoparticles. Filipov *et al*. [39] carried out LII experiments on Ag nanoparticle synthesized from chemically pure silver in a tube furnace at an elevated temperature of 1100 K, which were aerosolized in Ar (99.999%). They showed that the absorption efficiencies of Ag nanoparticles at 1064 nm was orders of magnitude lower than the absorption efficiencies at 355 nm; consequently, they irradiated the Ag nanoparticles with a

355 nm laser (15 ns pulse duration), and signals were detected with a PMT equipped with bandpass filters centred at 500 nm. The observed signals exponentially decayed from the peak of the signal in less than 70 ns, which they treated as incandescence.

Sipkens *et al*. [29] also carried out LII experiments on Ag nanoparticles produced through wet chemical synthesis, which were aerosolized in different motive gases. They carried the experiments using an Artium 200 M LII system, which irradiated the nanoparticles with a 1064 nm laser and detected the signals with PMTs at detection wavelengths of 442 nm and 714 nm. The pyrometrically-inferred temperatures decayed after about 75 ns, which they treated as a consequence of incandescence.

In this chapter, the observed signals from Ag and Au nanoparticles are presented and qualitatively assessed. Potential phenomena that could be responsible for the signals are described.

6.1 Observed LII signals

The experiment was carried out with the apparatus described in Chapter 3 and the experimental procedure described in Chapter 4. Figure 6-1 shows a shot data typical of observed signals of both Ag and Au nanoparticles aerosolized in different motive gases, at all laser fluences[24]. The sharp drop of the signals is markedly different to those from Ni and Fe nanoparticles, as shown in Figure 6-2. Figure 6-2 also shows that the observed signal follows the temporal profile of the laser. Because incandescence is a thermal phenomenon, energy absorbed by the nanoparticles should persist long after the end of the laser pulse, as can be seen for Ni and Fe nanoparticles. While Filipov *et al*. [39]

[24] Although not previously discussed, synthesized positively-charged Au nanoparticles did not produce observable signals during preliminary experiments, which confirmed an initial hypothesis (*cf.* §6.1.1) [160]. However, these experiments need to be repeated for a definite conclusion.

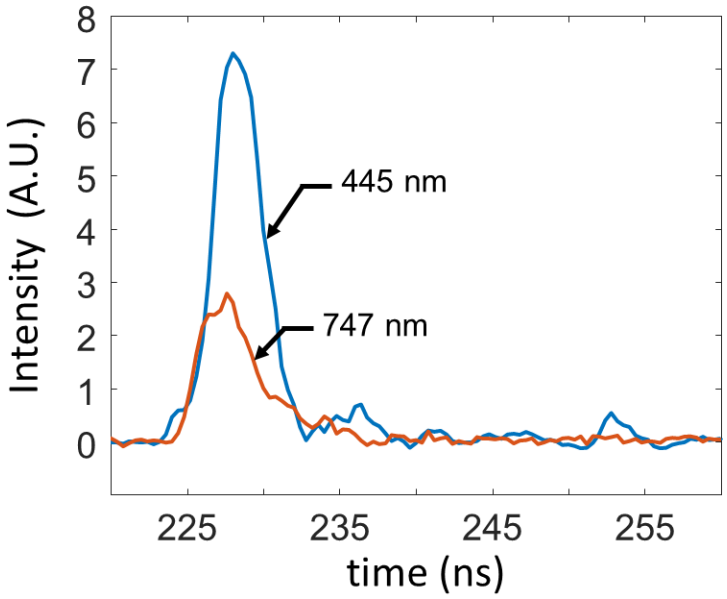

Figure 6-1: LII calibrated data from one shot of positively-charged Ag nanoparticle aerosolized in N_2 and irradiated with a 1064 nm wavelength with a fluence of 2.4 mJ/mm^2.

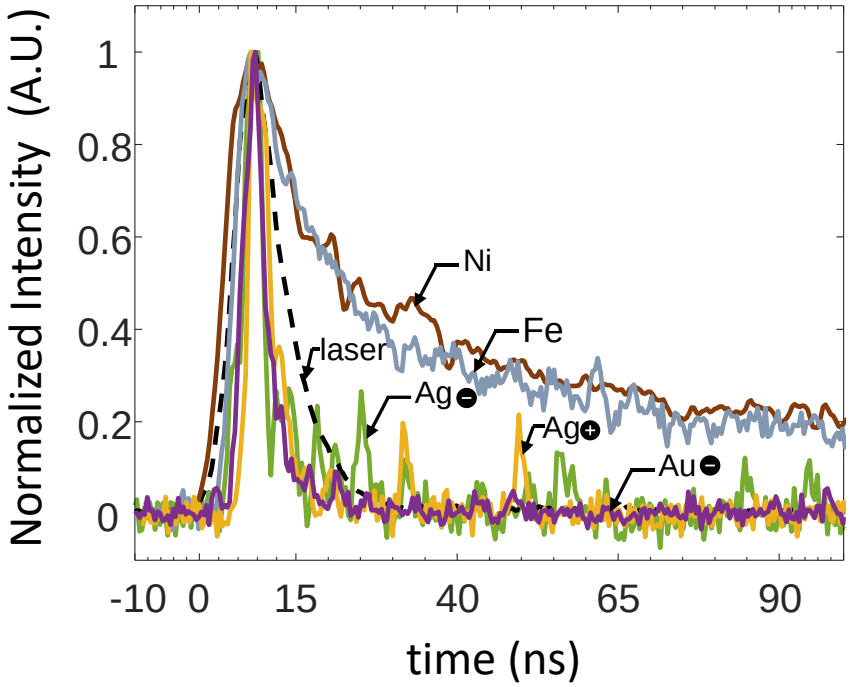

Figure 6-2: Comparing timescales of the laser pulse to observed signals, at 747 nm, from all synthesized nanoparticles. Signals were aligned at the peak.

and Sipkens *et al*. [29] observed signals that were longer than the laser pulse, their observations are likely a consequence of the experimental apparatus used in each case. Filipov *et al*. [39] used a 355 nm laser, so, in this case, the LII signals could be due to interference at the detection wavelength resulting from excitation of Ar and Ag electronic bands caused by the UV ionizing radiation. In the case of Sipkens *et al*. [29], the observed signals were most likely broadened by the amplifying electronics in the Artium 200 M system. LII experiments on the plasmonic nanoparticles were also carried out with the LII 300 (Artium technologies), which contains electronics similar to Artium 200 M system. These signals were not accurately captured because the unusually short signal duration was broadened to about 60 ns due to the amplifying electronics in the system (*cf.* Appendix E.5). Since there are no amplifying electronics in the PMTs used in this current work, the short signals are accurately captured owing to the fast response of the PMTs.

The pyrometrically-inferred peak temperatures suggest that the Ag and Au nanoparticles approach their boiling point of 2435 K and 3129 K, respectively [86] with increasing fluence (*cf.* Figure 6-3), implying that there is a heating process occurring despite the low absorption cross-section at the laser wavelength. Therefore, since no incandescence is expected, the signals are most likely due to another broadband phenomenon. The discrepancy in peak temperatures for the positively- and negatively-charged Ag nanoparticles is probably due to the interpreting of the unknown signal origin as incandescence. Additionally, this unknown signal could be dependent on the different capping agents (trisodium citrate and CTAB used for negatively- and positively-charged Ag nanoparticles, respectively) and morphology of the nanoparticles (*cf.* §6.1.2).

The hypothesis that the observed signals are of non-incandescent origins is further validated since the signal decay is independent of fluence, as shown in Figure 6-4, which is contrary to what

is expected from incandescent signals [26]. Furthermore, this suggests that there is no evaporation occurring even when the peak temperatures reach the boiling point of the metals.

Considering the identified anomalies in the observed signals, it is a plausible conclusion that the signals from Ag and Au nanoparticles are not due to laser-induced incandescence and another laser-induced phenomenon is needed to explain the observations.

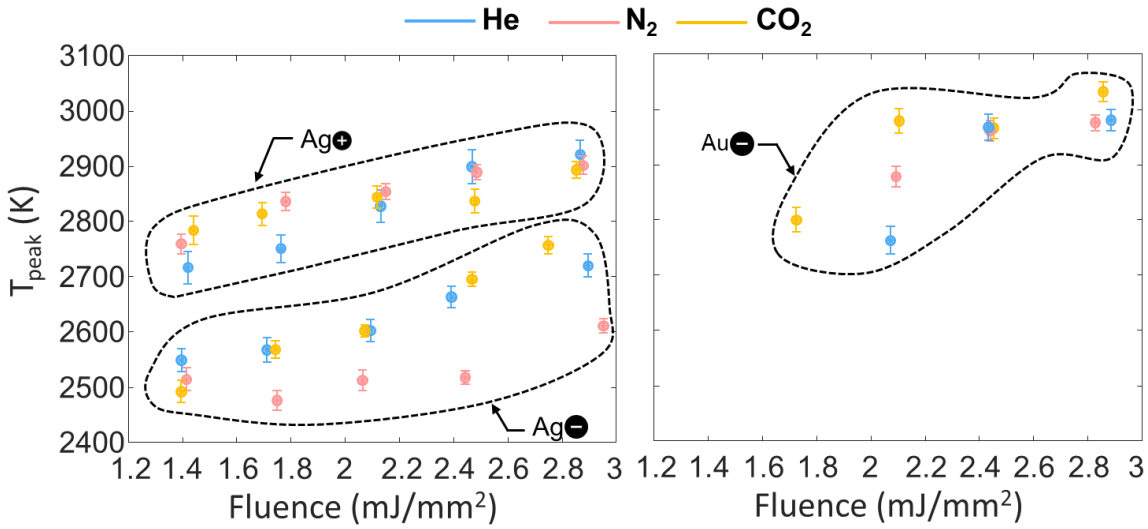

Figure 6-3: Pyrometrically-inferred peak temperatures of Ag and Au nanoparticles. CTAB is used as a capping agent for the positively-charged Ag nanoparticles and trisodium citrate is used for the negatively charged Ag and Au nanoparticles. Refractive indices of Ag (also used for Au) at the detection wavelengths are taken from Ref. [76].

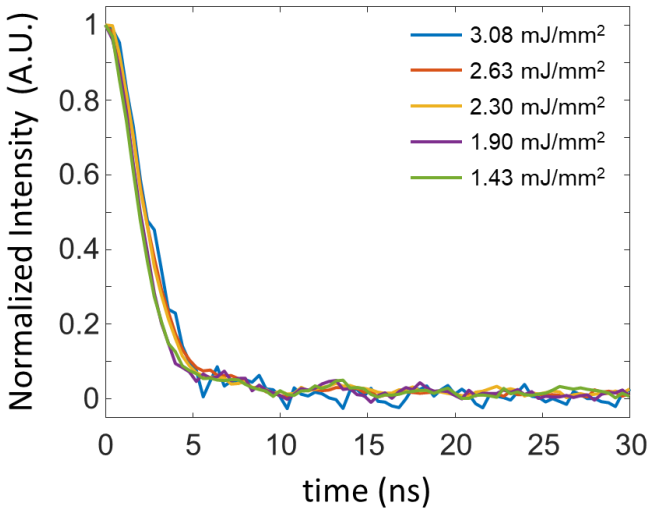

Figure 6-4: Observed signals at different fluences at the 747 nm detection wavelength from positively-charged Ag nanoparticles aerosolized in N_2.

6.2 Potential laser-induced emission phenomena

6.1.1 Electron-neutral Bremsstrahlung

Initial investigations into these results by Talebi Moghaddam *et al*. [58,159] suggested that electron-neutral Bremsstrahlung could be responsible for the observed signals. The proposed mechanism for this phenomena to occur during laser excitation of plasmonic nanoparticles is shown in Figure 6-5 and is described as follows: "Trigger" electrons from the nanoparticles are emitted through thermionic emission, a process in which thermally-excited electrons on the surface of the nanoparticle exceed the work function of the nanoparticle, as well as plasmonic decay photoemission, where electrons in the nanoparticle absorb laser photons and overcome the potential barrier of the nanoparticle. (The more positive the nanoparticle, the larger the potential barrier[25]). Emitted electrons then interact with gas molecules through inverse neutral Bremsstrahlung, where electrons increase in temperature by accelerating around the gas molecule and absorbing more photons, and through neutral Bremsstrahlung, where the hot electrons emit Bremsstrahlung emission as they decelerate around the gas molecules. Finally, after the laser pulse, electron temperatures decrease through neutral Bremsstrahlung, consequently decreasing the intensity of the observed signal. Observed signals from Bremsstrahlung will have a shorter duration than incandescence because the electron interaction with the nanoparticles occurs at shorter timescales compared to radiative cooling of the nanoparticle that occurs as vibrational energies of the atoms are dissipated as photons at longer timescales. Nevertheless, since Bremsstrahlung is also a thermal phenomenon, it is expected that signal decay should persist after

[25] It was hypothesized that the nanoparticle can be positive enough that no electrons would be emitted, hence no signals would be observed.

the end of the laser pulse, which is not the case for Ag and Au nanoparticles, as seen from Figure 6-2.

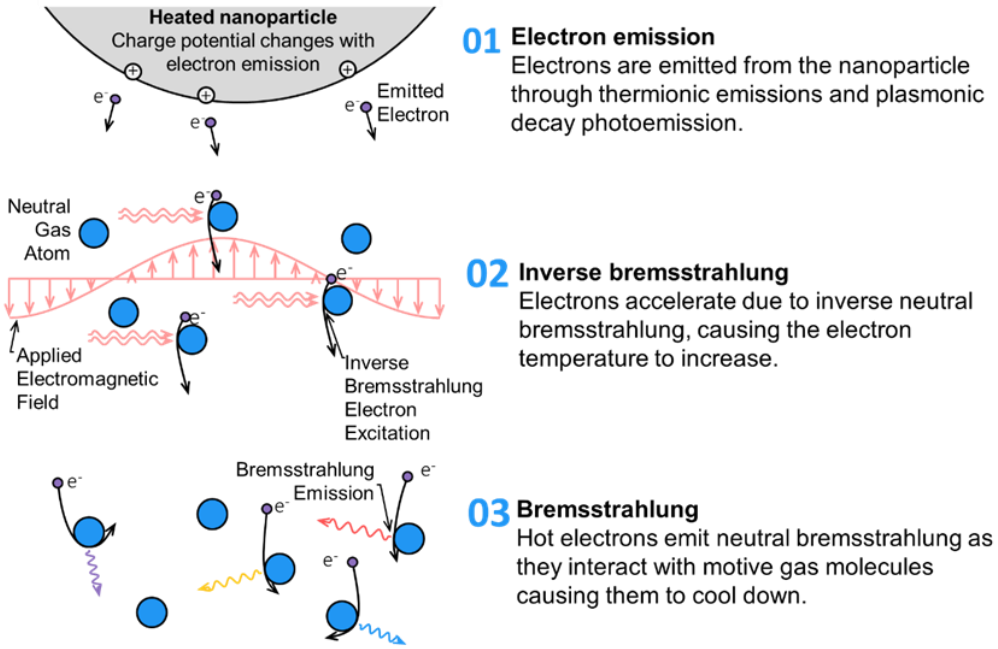

Figure 6-5: Schematic of electron neutral Bremsstrahlung phenomenon. Modified from Ref. [160].

Altman [50] has proposed that nanoparticle charging due to the thermionically emitted electrons causes a drop in the TAC at high temperatures, which could be affecting LII data analysis.

6.1.2 Multi-photon induced photoluminescence

A photoluminescence phenomenon might explain the observed signals because the associated timescales can be on the order of nanoseconds [137] and hence would follow the temporal profile of the laser pulse. Recent work by Talebi Moghaddam *et al.* [161] proposes multi-photon emission as the phenomenon responsible for observed signals from the plasmonic nanoparticles. A schematic of the phenomenon is shown in Figure 6-6.

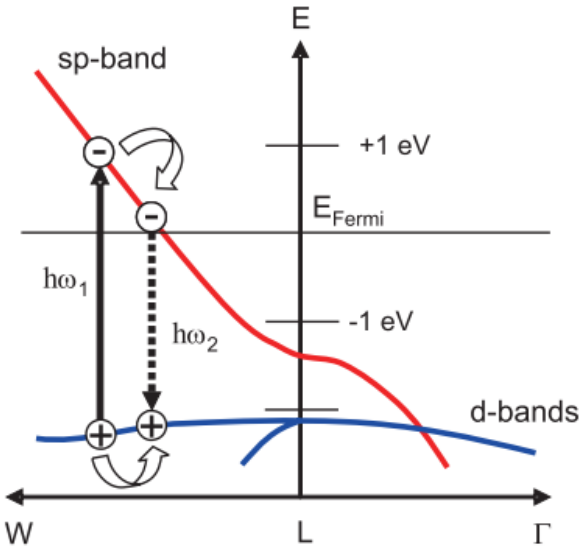

Figure 6-6: Schematic representation of the partial band structure of gold at the L symmetry point of the first Brillouin zone. The band energies are relative to the Fermi level [162].

For this phenomenon to occur, laser photons having energies, $h\omega_1$, of a characteristic wavelength, λ_1, excite electrons from the d-band into the sp-band of the metal, well above the Fermi level. After radiationless intraband relaxation of the hole in the d-band and the excited electron in the sp-band, interband recombination occurs, resulting in the emission of a photon with energy, $h\omega_2$, of a different characteristic wavelength, λ_2 [162,163]. The observed spectral intensity, J_λ, is expected to vary as a function of laser intensity, I_{laser}, through a power-law [162,163],

$$J_\lambda = A_0 \left(I_{\text{laser}} \right)^n, \tag{6.1}$$

where A_0 is a constant, and n is the power-exponent. Preliminary results, as shown in Figure 6-7, support this proposed phenomenon since the observed signals do vary with the laser intensity through the expected power-law. Additionally, the magnitude and nature (which constitutes features such as shape and peak position) of the observed photoluminescence depends on the capping agent/surfactant (or ligand) on the surface of the nanoparticles [164,165], consequently, because the negative and positive net charges on the nanoparticles were achieved by capping the

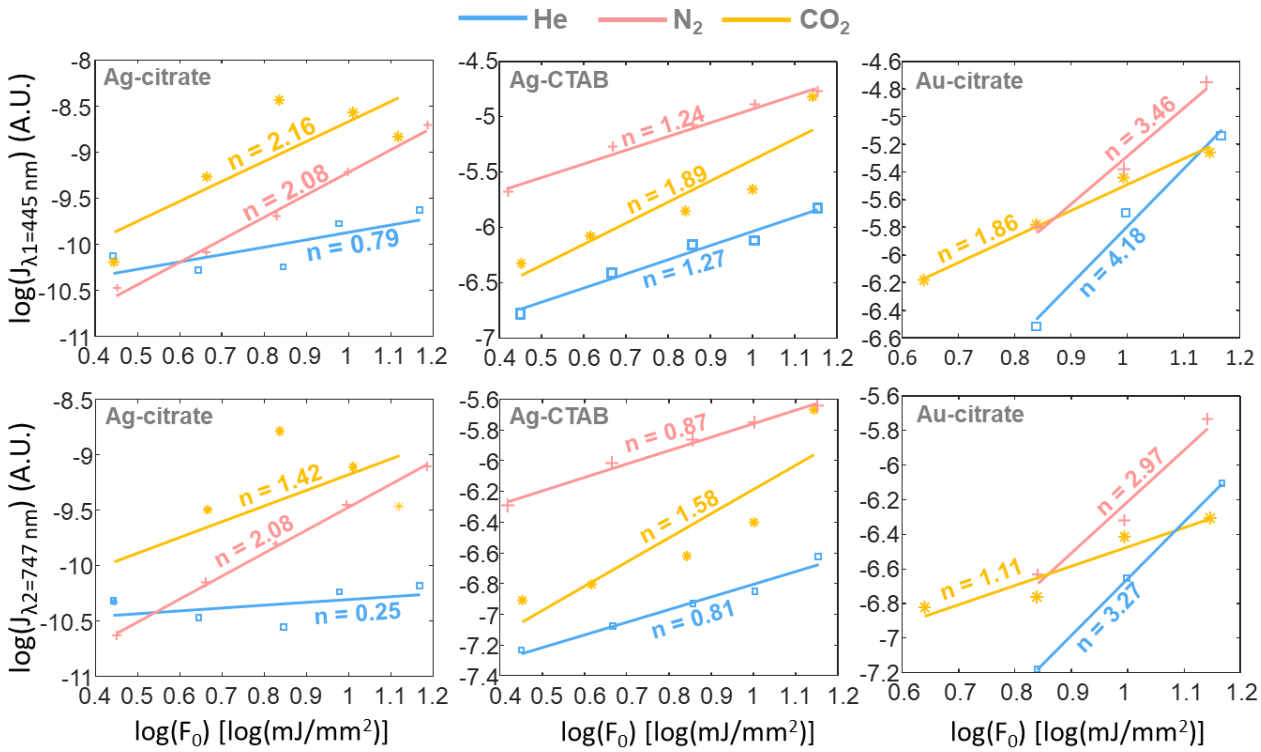

Figure 6-7: Power-law relationship data from the plasmonic nanoparticles. The laser intensity, I_{laser} is proportional to laser fluence, F_0. Modified from Ref. [161].

synthesized nanoparticles with different capping agents (*cf.* Chapter 4), the power-exponent, *n*, differed between the plasmonic particles.

Detailed quantitative assessment of the results is beyond the scope of this work; however, more investigation and analysis of the experimental data is currently underway.

Other photoluminescence phenomena such as fluorescence or chemiluminescence that have a short characteristic timescale could be occurring; however, they do not entirely account for the observed signals because they are spectral phenomena that occur within a narrowband, while the observed signals are broadband since there are observed intensities at both the 445 nm and 747 nm detection wavelengths, although lower at the 747 nm detection wavelength (*cf.*), as well as the 559 nm detection wavelength (though not used for analysis). Van der Wal *et al*. [24], Maffi *et al*. [54], Di Iuliis *et al*. [55], and Menser *et al*. [109] have observed non-incandescent LIE from non-

plasmonic nanoparticles of non-incandescent origin due to electronic excitation of the nanoparticles. Some of these have short durations, such as fluorescence [55], while some are delayed emissions with longer durations, for example, the atomic emissions from Si nanoparticles [109]. Further investigation into these possible spectral emissions that could also be occurring during experiments on plasmonic nanoparticles can be carried out with a broadband detector such as a streak camera.

6.2 Summary

This chapter provided the background and motivation for carrying out LII experiments on plasmonic nanoparticles along with a discussion of previous work by Filipov *et al*. [39] and Sipkens *et al*. [29] on Ag nanoparticles. It was concluded that the observed signals were not incandescence because of several anomalies that were identified, including short signal duration that followed the temporal profile of the laser pulse compared to the long signal duration of Ni and Fe nanoparticles, which generally show incandescence, high peak temperatures reached despite the low absorption cross-section of the Ag nanoparticles at the laser wavelength, and fluence-independent signal decay.

Inverse neutral and neutral Bremsstrahlung, which depended on the charge of the nanoparticles, was initially considered as a potential phenomenon to describe the process, but the mechanism of this phenomenon required signal decay to persist at later cooling times longer than the timescale of the laser. Multi-photon photoluminescence, which depends on the surface chemistry (including capping agent and morphology) of the plasmonic nanoparticles, is currently the more likely candidate phenomenon responsible for the observed signals due to the short characteristic timescales of the LII data and the identified power-law relationship between the observed spectral intensity and laser intensity, which varied with capping agent. Although the

observed signals are due to a broadband phenomenon, other narrowband phenomena could be occurring as well, as observed in the literature, which can be further investigated with a broadband detector.

Chapter 7

Conclusions and Future work

Time-resolved laser-induced incandescence (TiRe-LII) is an established diagnostic for characterizing soot-laden gases and is quickly becoming a standard for *in situ* characterization of non-carbonaceous nanoaerosols, including metal nanoaerosols. This thesis used a modified model of the TiRe-LII framework to investigate laser interactions with metal nanoparticles to improve the physical understanding of the various phenomena that affect the diagnostic. This chapter summarizes and concludes the major key points from this thesis work and recommends future work that can be explored. The chapter closes with the impacts that this work and future work provide for the advancement of the technique and other applications.

7.1 Summary and conclusion

This work was motivated to address a number of uncertainties in the TiRe-LII technique that have been reported in the literature. Chapter 1 surveyed the literature and showed that many researchers identified the potential of the diagnostic and extended its application from soot-laden flows (the pioneering application of LII) to metal nanoaerosols. However, they found that several phenomena of known origin (for example, atomic emissions from the nanoparticle [109]) and unknown origin (for example, excessive absorption [24,28,54,55]) corrupt the LII data and complicate the interpretation of the results. Others also found that the experimental absorption properties, including the refractive indices, were unable to explain the data. Recently, it was found that some of the observed anomalies were accounted for by modifying the absorption model by replacing the Rayleigh approximation with Mie theory [59], but others remain unexplained.

The goal of the thesis was to further develop the TiRe-LII technique for metal nanoparticles by regressing the TiRe-LII model to the spectral incandescence data while solving for the absorption efficiencies of the nanoparticles using Mie theory, temperature-dependent properties, and accounting for the polydispersity of the nanoparticles, thereby improving existing TiRe-LII analysis techniques in the literature. The investigation was carried out with experiments on Ni, Fe, Ag and Au nanoparticles in the gas-phase.

The details of the measurement model were explored in Chapter 2 through an extensive discussion of the heat transfer and spectroscopic submodels. Model-relevant properties for Ni and Fe nanoparticles were presented. The TiRe-LII apparatus was discussed in Chapter 3, which included a description of the operation of both the optical setup and aerosol generator. The wet chemical synthesis, and *ex situ* characterization techniques and results for Ni, Fe, Ag, and Au nanoparticles were presented in Chapter 4, including an outline and description of the LII experimental data acquisition.

Analysis of the experimental data from Ni and Fe nanoaerosols was conducted in Chapter 5 to examine the performance of the modified TiRe-LII model, to further investigate the underlying phenomena occurring during the experiments, and to compare results to the literature. It was found that the normalized incandescence signals decreased rapidly with increasing fluence, which is generally attributed to evaporation at higher fluences [26] but the integrated intensities, which are expected to also decrease due to mass loss at high fluences, increased with increasing fluence. This observation was attributed to corruption of the LII signals that consequently caused high peak temperatures that did not plateau with fluence. The results and simulations showed that excessive absorption was occurring at the laser wavelength. It was determined that the size classes of the nanoparticles suggested conduction was happening in the transition regime, and consequently, a

transition regime conduction model was needed to accurately infer the thermal accommodation coefficients (TACs) of the metal nanoaerosols, particularly for the polyatomic gas molecules. The inferred TAC of 0.27 for the Ni-Ar nanoaerosol was smaller than the TAC of 0.51, inferred from molecular dynamics simulations.

A qualitative analysis of the LII data from Ag and Au nanoparticles, performed in Chapter 6, supported the hypothesis that multi-photon photoluminescence is responsible for the short-duration, non-incandescent signal observed for the plasmonic nanoparticles, which could be present, as a corruption, in the LII data of incandescent origins.

7.2 Future work

The recommended future work is divided into the following sections.

7.2.1 Transition regime modelling

Considering that the LII data of Ni and Fe nanoaerosols are cooling by conduction in the transition regime, which could be responsible for the inflation of the inflated TACs of the polyatomic gas nanoaerosols, a transition regime model should be used to reanalyze the data. This will allow for a more accurate inference of the TACs and provide more insight into the conduction physics in this regime. Liu *et al*. [91] recommend the Fuchs transition regime model as it is in good agreement with the results of the direct simulation Monte Carlo (DSMC) method in the entire transition regime.

7.2.2 Explore the solution space

As with any optimization problem, it is necessary to determine that the estimated set of parameters that supposedly minimize the problem are at the global minimum. This becomes even more important with the addition of more QoIs or nuisance parameters as the solution space might lose

convexity or become more ill-posed (priors can help reduce ill-posedness). In this work, the model was assumed to be locally linear, consequently, the posterior distribution was approximated as Gaussian, which might not be the case, as seen in Figure 7-1. A Markov Chain Monte Carlo (MCMC) procedure should be utilized to sample the solution space to obtain the most accurate posterior distribution by accounting for model non-linearities and capturing multiple local minima to ensure that only the strongest global minimum parameters are being inferred from the model.

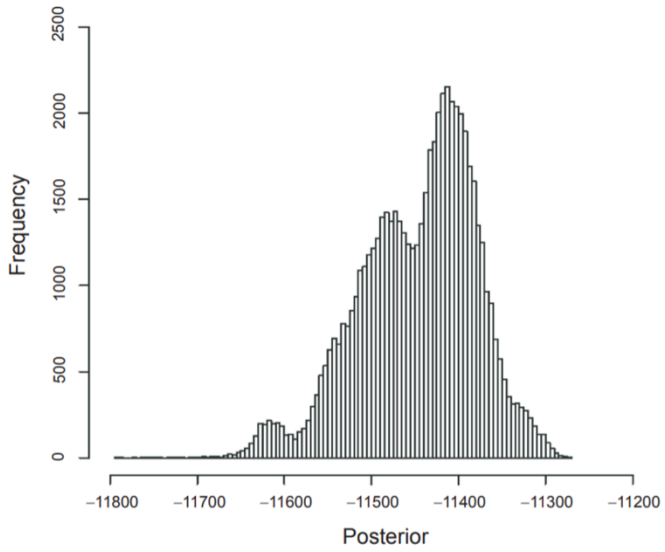

Figure 7-1: A non-Gaussian MCMC posterior distribution with multiple peaks [166].

7.2.3 Molecular Dynamics simulations

Molecular dynamics simulations of the collisions and interactions between metal nanoparticles and carbon-containing gas molecules should be carried out to investigate how factors that include the attractive potential between the metal and gas molecules and the structure of the gas molecule affect the TACs. This would help understand why the polyatomic gas molecules considered in this study might not be accommodating energy as expected from results in the literature where TACs are lower with increasing gas molecule complexity. The MD simulations will also help with investigating whether or not the TACs for polyatomic nanoaerosols depends on the constituent elements of the polyatomic gas molecule.

7.2.4 Alternative aerosol generation

The aerosol generation process used in this work involved chemically synthesizing nanocolloids and aerosolizing the nanoparticles in a motive gas using an atomizer. This method of aerosol generation provides the flexibility of chemically synthesizing any material and aerosolizing in any motive gas. Additionally, nanoparticles in colloidal form are less likely to aggregate compared to colloids formed by dissolving commercially available nanopowders in solvents. However, mastering the wet chemical synthesis of a new nanoparticle material can be time-intensive and even more so when the size of the nanoparticles needs to be controlled. This is mostly a trial-and-error procedure, and any slight variation, such as the presence of minuscule impurities, can drastically affect the results. Furthermore, the performance of the atomizer can introduce uncertainties in data collection, such as producing aggregated nanoparticles during the atomization and drying process. An extensive evaluation and characterization of the TSI pneumatic atomizer will be beneficial.

It would also be good to explore other alternatives to producing nanoparticles in the gas-phase. One alternative is a spark discharge generator, which will also provide the flexibility of using any motive gas and nanoparticle material while also producing unaggregated particles of small size classes in a consistent way. A pin-to-plate spark discharge generator has been built according to Ref [167] to explore this alternative. Other alternatives are the hot-wall flow reactor used in Ref [26] and photolysis used in Refs [25,83]. These alternatives commonly produce gas-phase nanoparticles of ~ 10 nm in diameter, which would ensure heat conduction in the FMR and avoid ambiguities with the conduction model in the transition regime. It would also make it possible to determine the absorption efficiencies with the Rayleigh approximation, which would simplify the absorption model and allow for pyrometry.

7.2.5 Experiments on other types of nanoparticles

The LII data from Ag and Au nanoparticles provided insight into some of the other phenomena that may be occurring during the laser heating process, which can inform researchers on how to improve experiments or the LII model. Additionally, the analysis of the first-ever extensive LII data of Ni nanoparticles, presented in this work, helped evaluate results from MD simulations in the literature. More TiRe-LII experiments on other novel nanoparticles can continue to provide insight that would help advance the TiRe-LII technique. For example, metal oxides such as titania (TiO_2) can shed light on how the various non-incandescent signals produced in the presence of the oxide [55] can affect parameter inference by the TiRe-LII model. Additionally, LIE signals from other nanoparticles (plasmonic or otherwise) that may not heat up, as predicted by the heat transfer model, could continue to inform the LII community of more potential LII signal corruptions that should be taken into account.

7.2.6 Upgrade the detection system

Although the detection system used in this work had three detection wavelengths, only two of them were used for analysis. Discussion in §1.2.2 showed that analysis with data from more detection wavelengths could make the analysis and, consequently, the results more robust. Additionally, the discussion in Chapter 6 highlighted the possibility of other narrow band spectral phenomena that may be occurring along with multi-photon photoluminescence. Therefore, experiments with more detection wavelengths, like that of Figure 7-2(a) with four PMTs or a streak camera that measures time-resolved signals at continuous broadbands, as seen from Figure 7-2(b), would be greatly beneficial to TiRe-LII analysis and investigation.

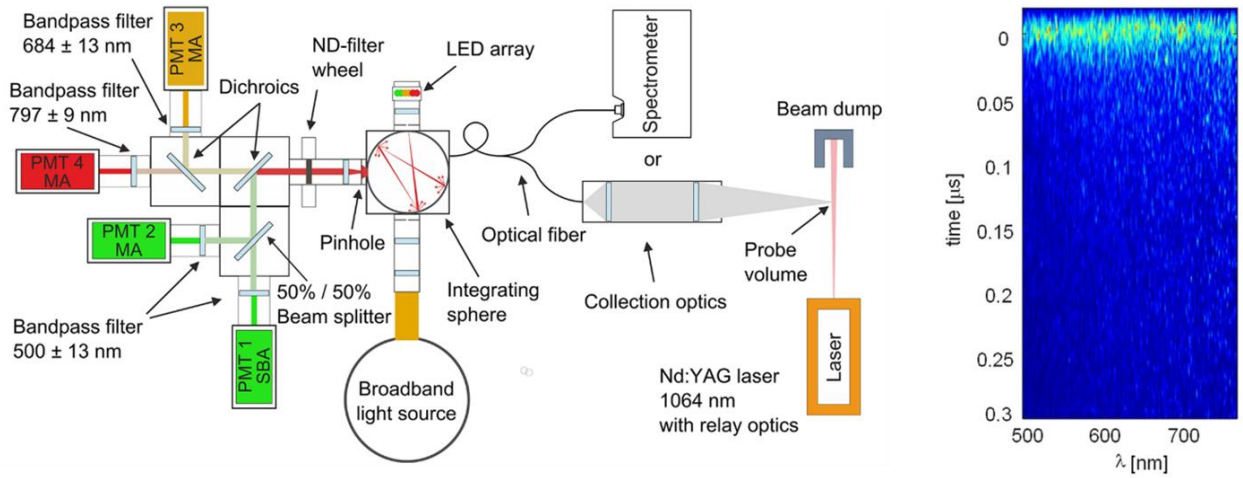

Figure 7-2: (a) A 4-colour LII setup [66] and (b) continuous broadband LII signal from a streak camera between 500 nm and 770 nm [65].

7.3 Impacts

This work has developed new tools and insights into investigating results from TiRe-LII data. Further exploration will provide practical impacts by obtaining information to develop more accurate measurement models that correctly account for any possible LII corruption, and help explain and correct known deficiencies in the general LII model, for example, the anomalous cooling phenomena observed for soot [29,56,57] or the excessive absorption phenomenon observed for metal nanoparticles [29], as well as shed light on certain hypotheses that might be occurring at the nanoscale, such as a size-dependent complex index of refraction [51] or the decrease in TAC at high temperatures [50]. This will improve the reliability of LII-derived aerosol properties and extend the range of aerosols that can be measured by this technique. Fundamental insights will also be provided into the understanding of laser-nanoparticle interactions and other physical processes that occur at the nanoscale that could be exploited in other scientific and engineering applications.

Appendices

This section of the thesis document features the various supplemental information that were referred to in the thesis chapters. Appendix A discusses the details of the Bayesian framework used in Chapter 5. Appendix B presents the mathematical framework of the non-linear minimization algorithms that were used in this work. Appendix C provides a detailed description of the calibration procedure used for the TiRe-LII apparatus. Appendix D presents supplemental information that relate to the conduction heat transfer from the nanoparticle. Appendix E provides all other miscellaneous supplemental information.

Appendix A

The Bayesian framework

The Bayesian framework quantifies the degree of uncertainty of the inferred results while allowing for a certain degree of ground truth (priors), which can take different forms and nuisance parameters (*cf.* §A.1) to be incorporated into the inference procedure. The framework is becoming prominent in LII analysis for the inference and uncertainty quantification of a variety of QoIs [20,22,28,29,168].

In the Bayesian framework, QoIs are not deterministic, rather, the unknown solution vector of parameters, **x**, and the data vector **b**, are visualized as random variables that obey probability density functions (pdfs) that are related by the Bayes' equation [148],

$$p(\mathbf{x}\,|\,\mathbf{b}) = \frac{p(\mathbf{b}\,|\,\mathbf{x})\,p_{\mathrm{pr}}(\mathbf{x})}{p(\mathbf{b})}\,, \tag{A.1}$$

where $p(\mathbf{b}|\mathbf{x})$ is the likelihood pdf of the observed data, **b**, occurring for a hypothetical set of model parameters, **x**, $p(\mathbf{x}|\mathbf{b})$ is the posterior pdf of **x** being the model solution given the data set **b**, $p_{\mathrm{pr}}(\mathbf{x})$ is the pdf of the prior knowledge of **x**, and $p(\mathbf{b})$ is the evidence of all possible solutions occurring, which is used to scale the posterior pdf to satisfy the Law of Total Probability.

Because it is often cumbersome and unnecessary to calculate $p(\mathbf{b})$, the proportionality,

$$p\left(\mathbf{x}\,|\,\mathbf{b}\right) \;\propto\; p\left(\mathbf{b}\,|\,\mathbf{x}\right) p_{\mathrm{pr}}\left(\mathbf{x}\right), \tag{A.2}$$

is usually computed since only the distribution around the most probable solution is typically of interest. When all set of solutions are equally credible, $p_{\mathrm{pr}}(\mathbf{x}) = 1$ and $p(\mathbf{x}|\mathbf{b}) \propto p(\mathbf{b}|\mathbf{x})$.

When the data is independent and normally distributed, the likelihood takes the form [148],

$$p(b_i \mid \mathbf{x}) = \frac{1}{\sigma\sqrt{2\pi}} \exp\left[-\frac{1}{2} \frac{b_i - M_i(\mathbf{x})^{\,2}}{\sigma^2} \right], \tag{A.3}$$

where σ is the standard deviation of the normal distribution, $M_i(\mathbf{x})$ and b_i are the model and data points, respectively. Maximizing Eq. (A.3) produces the most likely set of model parameters and is equivalent to minimizing the exponential argument in Eq. (A.3), converting it into a weighted least-squares problem. Considering covariance in the data, $\mathbf{\Gamma}_\mathrm{b}$, the vector $\mathbf{x}$, that maximizes the posterior, i.e. the maximum likelihood estimate (MLE), is then expressed as

$$\mathbf{x}_{\mathrm{MLE}} = \arg\max\left(p(\mathbf{x} \mid \mathbf{b}) \right) = \arg\min \left\| \mathbf{\Gamma}_\mathrm{b}^{-1/2} \left[\mathbf{b} - \mathbf{M}(\mathbf{x}) \right] \right\|_2^2 . \tag{A.4}$$

When prior knowledge, $p_{pr}(\mathbf{x})$, is incorporated into the inference in the form of gaussian distributions, it is akin to adding more equations to the minimization problem and the resulting solution is known as the *maximum a posteriori* (MAP) estimate,

$$\mathbf{x}_{\mathrm{MAP}} = \arg\max\left(p(\mathbf{x} \mid \mathbf{b}) p_{\mathrm{pr}}(\mathbf{x}) \right) . \tag{A.5}$$

When Gaussian priors are used, Eq. (A.5) can be computed by,

$$\mathbf{x}_{\mathrm{MAP}} = \arg\min \left\| \begin{bmatrix} \mathbf{\Gamma}_\mathrm{b}^{-1/2} \mathbf{M}(\mathbf{x}) \\ \mathbf{C}_\mathrm{x}^{-1/2} \mathbf{x} \end{bmatrix} - \begin{bmatrix} \mathbf{\Gamma}_\mathrm{b}^{-1/2} \mathbf{b} \\ \mathbf{C}_\mathrm{x}^{-1/2} \mathbf{x}_{\mathrm{prior}} \end{bmatrix} \right\|_2^2 \tag{A.6}$$

where $\mathbf{x}_{\mathrm{prior}}$ is a vector of the means of the prior distributions, and $\mathbf{C}_\mathrm{x}$ is the covariance of the prior distributions. Cholesky factorization can be used to simplify the square root of the inverted covariance matrix to an upper triangular matrix [148].

A.1 Bayesian Priors and Nuisance Parameters

Incorporating Bayesian priors into the inference procedure allows for available knowledge of some parameters to be used, which reduces the ill-posedness that occurs due to information deficit. However, care should be taken to ensure the optimal choice of priors that would both reflect the

available information as well as the uncertainty of the information. Hadwin *et al*. [20] showed that the choice of priors is a significant step during inference as the accuracy and posterior distribution can be significantly affected. An uninformative prior, $p_{\mathrm{pr}}(\mathbf{x}) = \mathbf{1}$, is used when no information is available *a priori*. Depending on the nature and certainty of the *a priori* knowledge, a variety of priors (or a combination of priors), as shown in Figure A-1, can be used.

In a limiting case where model input parameters that are not of interest are unknown or known with little certainty, the Bayesian framework allows for the inference of such parameters, called nuisance parameters. Bayes' equation becomes

$$p(\mathbf{x},\boldsymbol{\theta}\,|\,\mathbf{b}) = \frac{p(\mathbf{b}\,|\,\mathbf{x})\,p_{pr}(\mathbf{x})\,p_{pr}(\boldsymbol{\theta})}{p(\mathbf{b})}, \tag{A.7}$$

where $\boldsymbol{\theta}$ is the vector of nuisance parameters, and $p_{pr}(\boldsymbol{\theta})$ is the prior distribution. The nuisance parameters are also inferred along with the QoIs.

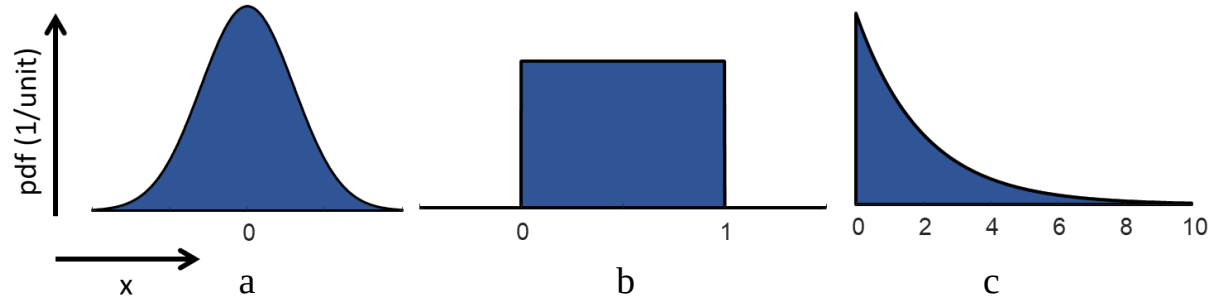

Figure A-1: (a) Gaussian, (b) uniform, and (c) exponential pdfs of sample prior distributions. The Gaussian distribution is used when the prior knowledge is normally distributed about a mean, the uniform distribution is derived from a bounded maximum entropy prior, and the exponential distribution is used when prior knowledge suggests that the parameters are more likely to occur at a bound and exponentially less likely to occur away from that bound.

A.2 Marginalization and Uncertainty Quantification

The Bayesian framework quantifies the uncertainty of the inferred parameters as a pdf, which is maximum at the MLE (in the case of the likelihood) or MAP (in the case of the posterior distribution). If the number of parameters to be inferred is two, the covarying posterior can be visualized by plotting the negative log-likelihood contours, $-\log[p(\mathbf{x}\,|\,\mathbf{b})] \propto -\log[p(\mathbf{b}\,|\,\mathbf{x})]$ as seen in Figure A-2(a), and a credibility interval can be defined using chi-squared statistics [169]. The unique uncertainty of each QoI is obtained by marginalizing the posterior probability density, which involves the integration of the product of the likelihood and prior probability densities over the nuisance parameters

$$p(x_j\,|\,\mathbf{b}) = \iint_{\mathbf{x}\neq x_j,\boldsymbol{\theta}} p(\mathbf{x},\boldsymbol{\theta}\,|\,\mathbf{b})\, p_{pr}(\mathbf{x},\boldsymbol{\theta})\mathrm{d}\boldsymbol{\theta}\mathrm{d}\mathbf{x}\,. \tag{A.8}$$

However, carrying out this integration analytically can be computationally intensive [170]; instead, a Markov chain Monte Carlo (MCMC) integration can reduce the computation effort required. The MCMC integration produces a sequence of random samples and evaluates the forward model; each sample is accepted or rejected based on the sampled location in the posterior distribution. Although each subsequent sample only depends on the preceding sample, the accepted random samples map the posterior distribution ergodically [20].

When gaussian priors are used, and the data is normally distributed, the marginalized posteriors, from a non-linear model, can be approximated to also follow a normal distribution (*cf.* Figure A-2(b) and (c)) with covariances computed by linearizing the posterior around the MAP,

$$\mathbf{C}_{\mathrm{x}'} = \left(\mathbf{J}(\mathbf{x})^{\mathrm{T}}\boldsymbol{\Gamma}_{\mathrm{b}}^{-1}\mathbf{J}(\mathbf{x}) + \mathbf{C}_{\mathrm{x}}^{-1}\right)^{-1}, \tag{A.9}$$

where $\mathbf{C}_{x'}$ is a diagonal matrix of covariances of the inferred parameters, and $\mathbf{J}(\mathbf{x})$ is the Jacobian evaluated at the solution $\mathbf{x}$ (MLE or MAP).

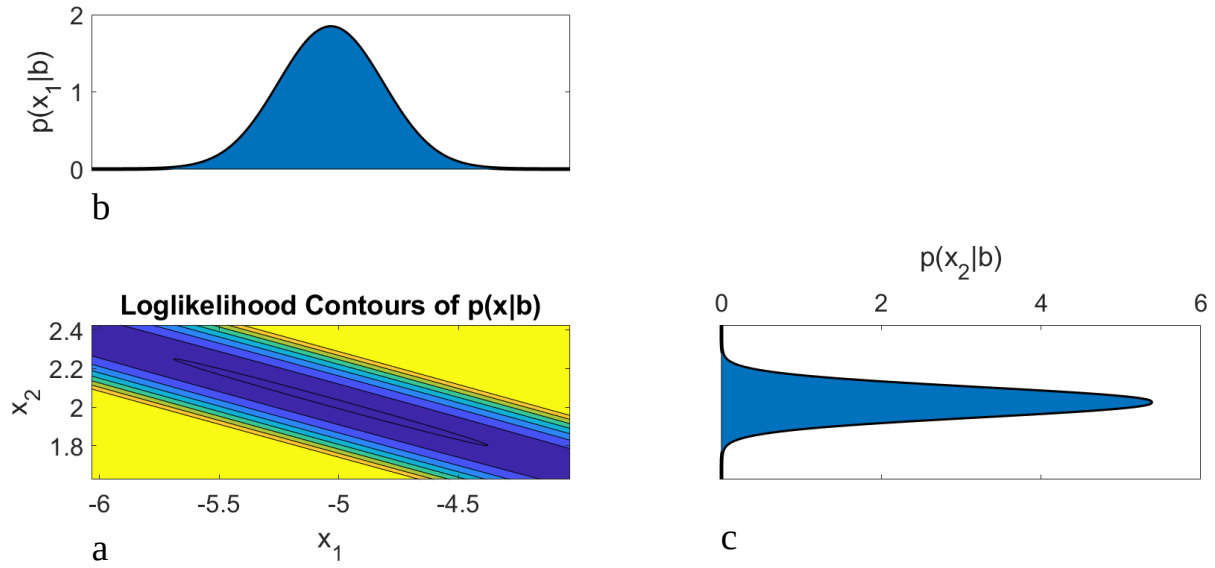

Figure A-2: (a) the covarying posterior pdf (b) the marginalized posterior pdf of variable 1 (c) the marginalized posterior pdf of variable 2.

Appendix B

Non-linear minimization algorithms

The equations derived from the Bayesian framework discussed in Appendix A are minimized by non-linear minimization algorithms to find x_{MLE} and x_{MAP}. These algorithms are also used for minimization procedures in later sections of the appendices. Minimization involves solving a problem, where a vector, **x**, of defined QoIs minimizes an objective function $f(\mathbf{x})$; the vector, $\mathbf{x}^*$, that minimizes $f(\mathbf{x})$ is defined as $\mathbf{x}^* = \text{argmin}_x[F(\mathbf{x})]$. If $f(\mathbf{x})$ is envisioned as a 3D surface plot as shown in Figure B-1, then the minimization algorithm is searching for the lowest possible point on the surface, i.e. the global minimum. For inference problems, the objective function, $f(\mathbf{x})$, is typically defined as the 2-norm of the residual vector, $\mathbf{r}(\mathbf{x}) = \mathbf{D} - \mathbf{M}(\mathbf{x})$, where **D** is the data and $\mathbf{M}(\mathbf{x})$ is the model and $f(\mathbf{x})$ is expressed as

$$f(\mathbf{x}) = \left\| \mathbf{D} - \mathbf{M}(\mathbf{x}) \right\|_2^2 , \tag{B.1}$$

and the vector, $\mathbf{x}^*$, that minimizes $f(\mathbf{x})$ is the least-squares solution [148]. When the statistical data are collected, the residual is scaled by the covariance of the data, $\boldsymbol{\Gamma}$, to place more confidence on the more reliable data points and less on the less reliable data points (i.e. weighted least-squares),

$$f(\mathbf{x}) = \left\| \left[\mathbf{D} - \mathbf{M}(\mathbf{x}) \right]^T \boldsymbol{\Gamma}^{-1} \left[\mathbf{D} - \mathbf{M}(\mathbf{x}) \right] \right\|_2 , \tag{B.2}$$

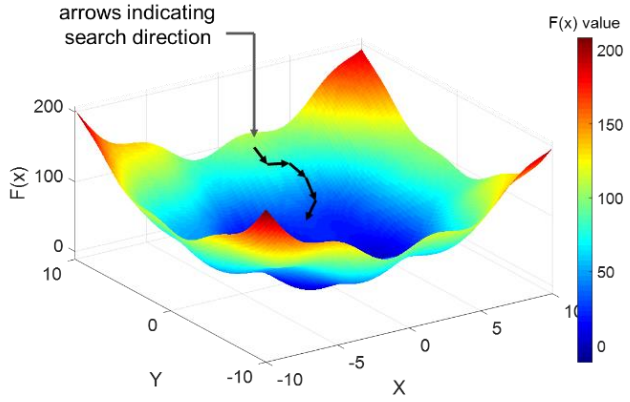

Figure B-1: An objective function map with arrows searching for the function minimum

There are numerous minimization algorithms that can minimize $f(\mathbf{x})$ [171]; however, in this work, two non-linear minimization algorithms were used, namely: Levenberg-Marquardt (LM), for solving unconstrained problems and trust-region reflective, for solving constrained problems, as well as genetic algorithm (GA), a metaheuristic algorithm for solving nonconvex problems.

B.1 Levenberg-Marquardt (LM) Algorithm

The LM algorithm is a modified version of Newton's method and a prominent non-linear least-squares minimization scheme [148,172]. The following provides a brief overview of the minimization scheme [148].

If the data is independently distributed[26] for each i^{th} data point and contains m data points, then $f(\mathbf{x})$ can be defined as

$$f(\mathbf{x}) = \sum_{i=1}^{m} \left(\frac{D_i - M_i(\mathbf{x})}{\sigma_i} \right)^2 , \tag{B.3}$$

where σ_i is the standard deviation of the i^{th} data point. The scalar-valued function is then,

$$f_i(\mathbf{x}) = \frac{D_i - M_i(\mathbf{x})}{\sigma_i} , \tag{B.4}$$

and vector $\boldsymbol{F}(\mathbf{x})$ can be defined as

$$\mathbf{F}(\mathbf{x}) = \begin{bmatrix} f_1(\mathbf{x}) \\ \vdots \\ f_m(\mathbf{x}) \end{bmatrix} , \tag{B.5}$$

Thus,

$$f(\mathbf{x}) = \sum_{i=1}^{m} f_i(\mathbf{x})^2 = \left\| \mathbf{F}(\mathbf{x}) \right\|_2^2 , \tag{B.6}$$

[26] This simplification is made for derivation purposes. The derived method can be generalized to solve eq. (B.2), if the noise is not independently distributed

and the gradient[27] of Eq. (B.6) gives (in matrix notation),

$$\nabla f(\mathbf{x}) = 2\mathbf{J}(\mathbf{x})^{\mathrm{T}}\mathbf{F}(\mathbf{x}), \tag{B.7}$$

where $\mathbf{J}(\mathbf{x})$ is the Jacobian matrix at $\mathbf{x}$.

The Hessian can be approximated as [148]

$$\mathbf{H}\big(f(\mathbf{x})\big) \approx 2\mathbf{J}(\mathbf{x})^{\mathrm{T}}\mathbf{J}(\mathbf{x}), \tag{B.8}$$

and from Newton's method,

$$\mathbf{H}\big(f(\mathbf{x})\big)\Delta\mathbf{x} = -\nabla f(\mathbf{x}) \tag{B.9}$$

where $\Delta\mathbf{x}$ is the difference between the current solution, $\mathbf{x}^{k+1}$, and the previous solution $\mathbf{x}^{k}$. Eq. (B.7) then becomes,

$$\mathbf{J}(\mathbf{x}^k)^T\mathbf{J}(\mathbf{x}^k)\Delta\mathbf{x} = -\mathbf{J}(\mathbf{x}^k)\mathbf{F}(\mathbf{x}^k). \tag{B.10}$$

The search for the optimal solution iteratively solves Eq. (B.10) for $\Delta\mathbf{x}$ so that the next update is found by, $\mathbf{x}^{k+1} = \mathbf{x}^{k} + \Delta\mathbf{x}$, until $\Delta\mathbf{x}$ reaches a defined tolerance in the vicinity of a minimum where $\nabla f(\mathbf{x}) = 0$.

Sometimes, $\mathbf{J}(\mathbf{x}^k)^{\mathrm{T}}\mathbf{J}(\mathbf{x}^k)$ might not accurately approximate the Hessian, in which case $\mathbf{J}(\mathbf{x}^k)^{\mathrm{T}}\mathbf{J}(\mathbf{x}^k)$ is regularized with zeroth-order Tikhonov, resulting in the LM non-linear minimization algorithm,

$$\left[\mathbf{J}(\mathbf{x}^k)^T\mathbf{J}(\mathbf{x}^k) + \lambda\mathbf{I}\right]\Delta\mathbf{x} = -\mathbf{J}(\mathbf{x}^k)\mathbf{F}(\mathbf{x}^k) \tag{B.11}$$

where λ is a positive parameter that is adjusted to ensure convergence.

[27] The gradient describes how the surface $\boldsymbol{F}(\mathbf{x})$ is changing.

B.2 Trust-Region-Reflective (TRR) Algorithm

When there is prior information about the QoIs specifically, a bounded range within which they should exist, constraints can be placed on the minimization problem. Using this bounded information is particularly helpful if the problem is ill-posed in the vicinity of the solution or if there are several local minimums in the search domain. The TRR algorithm is a type of interior-point algorithm [171] that narrows the search for the QoIs to within a trusted region. Note that there are inference approaches that allow for a variety of prior information incorporated into the inference (*cf.* Appendix A).

The trust-region-reflective algorithm is an interior point minimization algorithm equivalent to the unconstrained trust-region algorithm [173] modified by Coleman and Li [174], who proposed a reflection at the constraints during the line search step[28]. For the unconstrained trust-region problem, consider a model, q_k, that is Taylor series expansion of $f(\mathbf{x}_k)$, the scalar-valued objective function, about $\mathbf{x}_k$, the current solution,

$$q_k(\mathbf{x}_k + \Delta\mathbf{x}) = f(\mathbf{x}_k) + \nabla f(\mathbf{x}_k)^{\mathrm{T}} \Delta\mathbf{x} + \tfrac{1}{2} \Delta\mathbf{x}^{\mathrm{T}} \nabla^2 f(\mathbf{x}_k) \Delta\mathbf{x}\,, \tag{B.12}$$

and whose behaviour near $\mathbf{x}_k$, is similar to the behaviour of $f(\mathbf{x}_k)$. Next, define a neighbourhood, Δ_k, where the algorithm will only "trust" q_k, subject to the constraint,

$$\left\|\Delta\mathbf{x}\right\| \le \Delta_k\,, \tag{B.13}$$

to ensure that q_k is in a region close to $\mathbf{x}_k$, where it does behave like $f(\mathbf{x}_k)$ [173]. This leads to the minimization subproblem,

$$\begin{aligned} &\min_{\Delta\mathbf{x}} \; q(\mathbf{x}_k + \Delta\mathbf{x}) \\ &s.t. \;\; \left\|\Delta\mathbf{x}\right\| \le \Delta_k \end{aligned}\,. \tag{B.14}$$

[28] The line search step refers to movement along the vector between the current step and the next step.

The trusted neighbourhood decreases if the proposed solution does not minimize $f(\mathbf{x}_k)$. The optimality conditions show that $\Delta\mathbf{x}$ will be the solution of the linear system,

$$\left(\nabla^2 f(\mathbf{x}_k) + \lambda \mathbf{I}\right)\Delta\mathbf{x} = -\nabla f(\mathbf{x}_k), \tag{B.15}$$

where λ is the Lagrange multiplier [173]. The algorithm will search for the optimal solution iteratively until $\Delta\mathbf{x}$ reaches a defined tolerance in the vicinity of a minimum where $\nabla f(\mathbf{x}) = 0$.

The defined bounds of the minimization problem aim to solve,

$$\begin{aligned} &\min_{\Delta\mathbf{x}} f(\mathbf{x}) \\ &s.t.\ \ \mathbf{x_l} \le \mathbf{x}^* \le \mathbf{x_u} \end{aligned}, \tag{B.16}$$

where $\mathbf{x}^*$ is the optimal solution, and $\mathbf{x_l}$ and $\mathbf{x_u}$ are the lower and upper limits, respectively. The constraints are considered during the line search[29] step for determining $\Delta\mathbf{x}$. Coleman and Li [174] propose a piecewise reflective line search off the bounds defined by the constraints so that the optimal solution will always lie within $\mathbf{x_l} \le \mathbf{x}^* \le \mathbf{x_u}$. Figure B-2 illustrates the trust-region reflective algorithm.

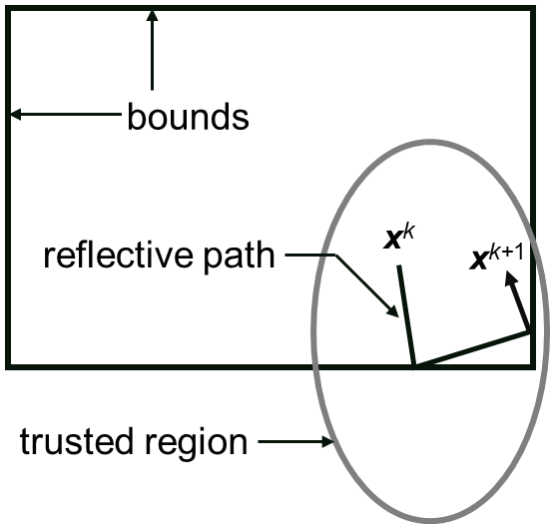

Figure B-2: Schematic of the trust-region-reflective algorithm. Modified from Ref. [175].

[29] The scaling of $\Delta\mathbf{x}$ to determine how far to move on the function surface.

B.3 Genetic Algorithm (GA)

Although non-linear minimization algorithms provide a solution to a problem, the solution might not always be a global minimum (i.e. the solution domain could be nonconvex) as it can be "stuck" in a local minimum. This can happen even in a bounded region in the vicinity or far from the optimal solution depending on the size of the defined constrained region. Metaheuristic algorithms such as GA provide a better guarantee of finding the global minimum through a random sampling of the whole solution domain [176].

The Genetic algorithm actually is class of evolutionary algorithms that rely on the mechanics of evolution strategies [176]. In this minimization approach, a set of individuals, called parents, are generated at the initial step of minimization to form a starting population. Each parent is a chromosome whose number of genes is determined by the number of QoIs (*cf.* Figure B-3). The value of a "goodness of fit" function, usually the fitness function, is evaluated for each parent in the population, and a selection process is carried out so that only the fittest parents (i.e. the individuals with the lowest value of $f(\mathbf{x})$) survive to produce children that move on to the next generation. Children are produced through various ways such as elitism where the fittest parents move on to the next generation as children, cross-over, where parents are paired at random and exchange genes, or mutation where particular genes in a parent undergo random sampling [176,177].

Several modifications can be applied to the basic GA approach for a variety of desired goals [176], such as defining the "goodness of fit" function as the gradient of the objective function $\nabla f(\mathbf{x})$, so that the fittest parents are those with the lowest value of the gradient (i.e. approaching the minimum faster), or defining a non-linear minimization algorithm that refines the GA solution (hybrid GA).

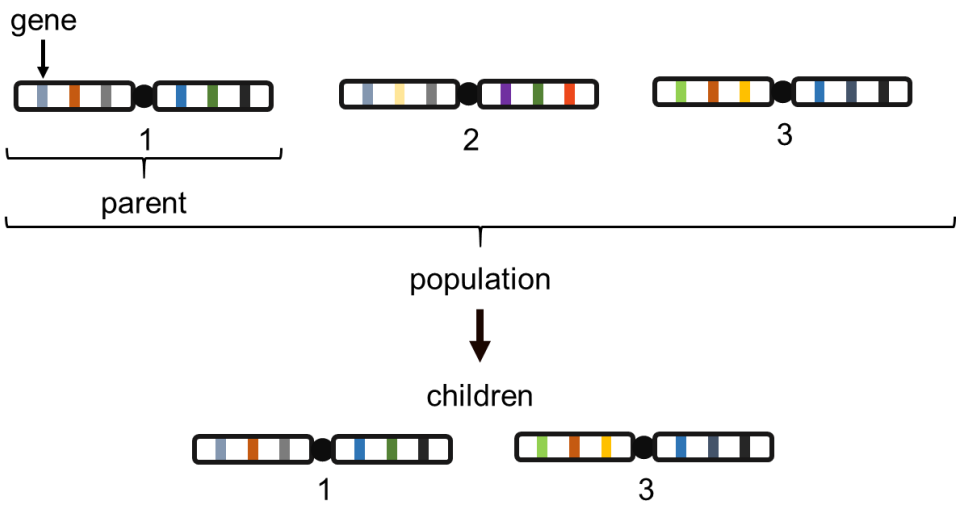

Figure B-3: Genetic algorithm with individuals having six QoIs. Children here have been chosen from elite parents.

Appendix C

Calibration Procedure

C.1 Component characterization

All optical components within the detection system were spectrally characterized to ensure their spectral positions, efficiency and bandwidths were fully known.

C.1.1 Spectrometer calibration

The spectral characterization of all components was carried out using a spectrometer (FLAME-T-VIS-NIR-ES, Ocean Optics). The spectral efficiency of the spectrometer was calibrated at the National Research Council (NRC) using an intensity calibrated light source. Figure C-1(a) shows the spectral efficiency of the spectrometer. Wavelength calibration of the spectrometer was also carried out using a Mercury-Argon (Hg-Ar) light source. The spectrometer data was linearly fit to the Hg-Ar light data using the Levenberg-Marquardt minimization scheme. The minimization was carried out in MATLAB® [107] using the "*lsqcurvefit*" function resulting in a linear correction of $\lambda - 1.97$, where λ is the spectral position of the spectrometer data. Figure C-1(b) shows the raw and corrected data.

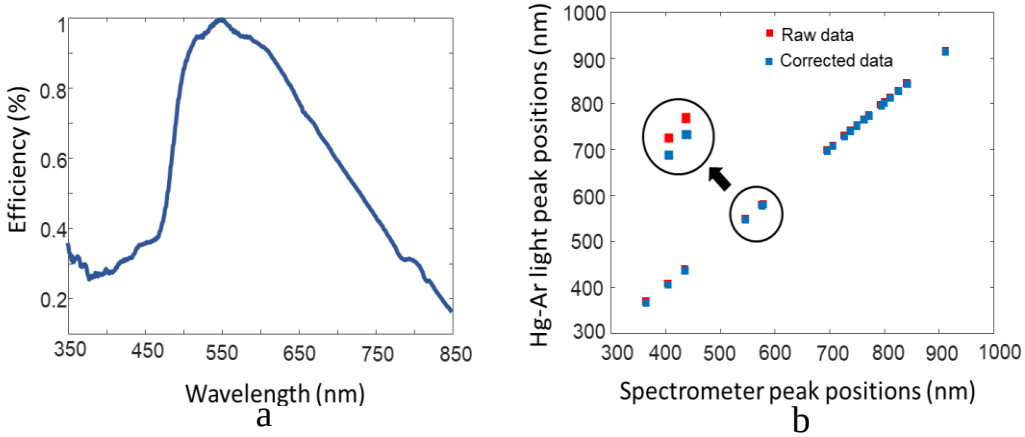

Figure C-1: Spectrometer Calibration: (a) spectral efficiency, and (b) wavelength correction. The inset in (b) shows, more clearly, the discrepancy between the raw and corrected data.

C.1.2 Optical component spectral characterization

A stabilized Halogen-Tungsten light source, 350 – 2600 nm (SLS201L/M, Thorlabs), fibre-coupled to an integrating sphere (Ø2" IS200-4, Thorlabs) and the spectrometer arrangement shown in Figure C-2 was used to characterize each optical component. Figure C-3 shows the transmission spectra of the dichroic mirrors and bandpass filters. Note that the 650 nm bandpass filter has a transmission of only 70% as compared to > 90% on the other bandpass filters. The effective bandwidth of the spectrum "seen" by the second PMT is achieved by convoluting the spectrums of the second dichroic mirror and the 650 nm bandpass filter. Figure C-4 shows the bandwidths and spectral positions of each PMT channel and how they compare to the spectrum of the Halogen-Tungsten light source.

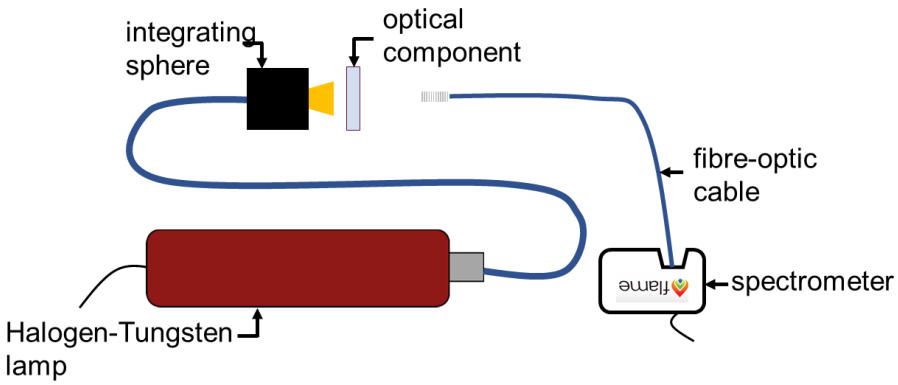

Figure C-2: Setup for characterizing the optical components.

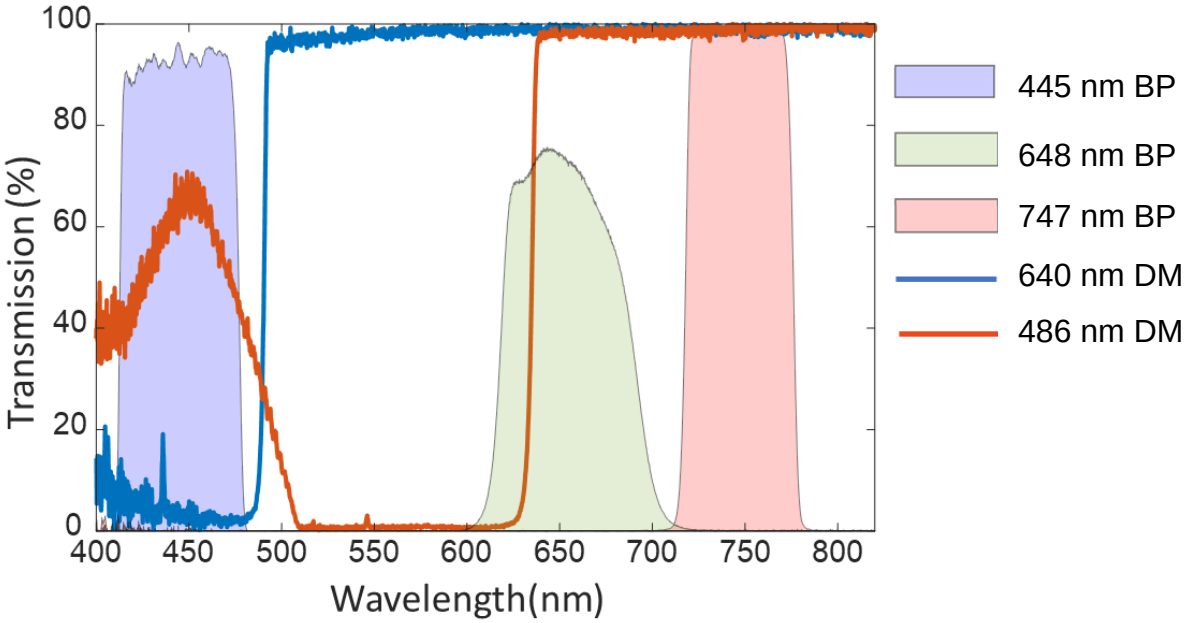

Figure C-3: Spectra of the optical components in the detection system. The center wavelengths of the bandpass filters have been determined more accurately by the calibrated spectrometer.

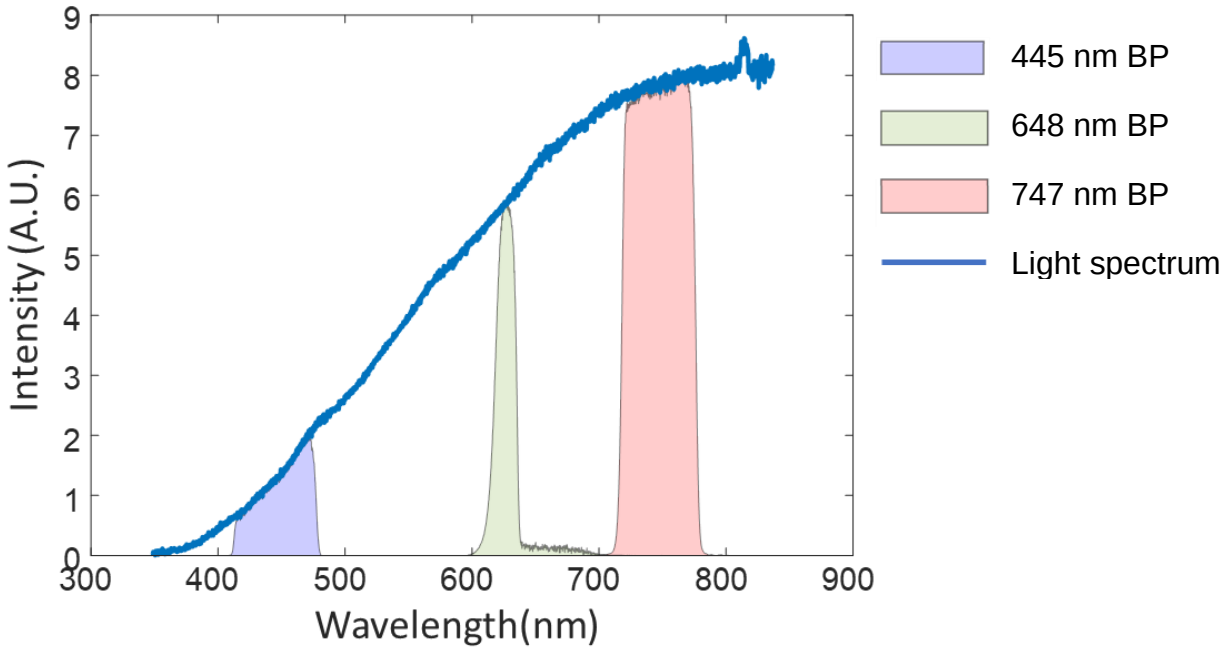

Figure C-4: Light spectrum and the spectral positions and bandwidths of the PMT channels.

C.2 TiRe-LII apparatus calibration

For this thesis work, the TiRe-LII detection system was directly calibrated for relative sensitivity. This subsection describes the calibration procedure carried out. The PMT responses were also analyzed to ensure proper functioning.

C.2.1 Calibration setup and data collection

As seen in Figure C-5, the calibration setup included the halogen-tungsten light source fibre-coupled to the integrating sphere placed in front of the detection system, an optical chopper, and an optical filter wheel were placed in front of the collection optics.

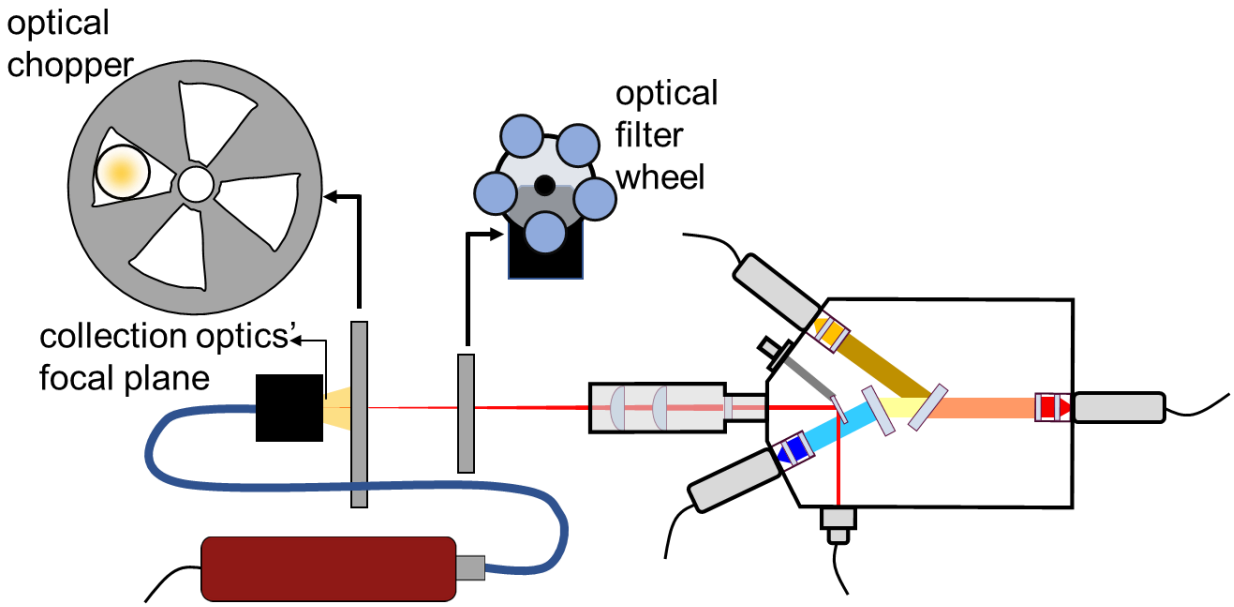

Figure C-5: Calibration setup.

The face of the integrating sphere was placed at the focal plane of the collection optics. To determine the focal plane of the collection optics, the laser diode within the demultiplexer box is turned on, and the flipper mirror is flipped in the "on" position to reflect the laser diode beam into the collection optics, which then focuses the beam onto the focal plane. After the integrating sphere

has been appropriately positioned, the laser diode is turned off and the flipper mirror is flipped out of the way.

The signals from the three PMTs within the detection system were digitized into voltage data by an oscilloscope (HDO6104 1 GHz High Definition Oscilloscope – Teledyne) with a 50 Ω coupling. The PMTs were powered by a voltage box that regulates the voltage supplied to the PMTs by changing the gains[30] from 1 – 1000. Care was taken so that the PMTs were not damaged by ensuring the PMT output voltages did not exceed the recommended maximum output voltages, shown in Table C-1, of a similar PMT[31].

Table C-1: Maximum recommended PMT output voltages [114].

Illumination Time	Max. Output Voltage (50 Ω Coupling)	Max. Repetition Frequency
DC	5 mV	-
100 μs	50 mV	100 Hz
1 μs	500 mV	10 Hz
10 μs	5 V	1 Hz

The optical chopper was placed in front of the light source to allow for a higher voltage readout as per Figure C-5 and to increase the signal-to-noise ratio by clearly separating the background signal from the light signal. In the absence of the optical chopper (DC light source), the voltage readout was noisy, and the surrounding had to be kept dark to minimize background noise. Figure C-6 compares the voltage readout with and without the optical chopper in place.

[30] The voltage box supply for PMT 1 and 3 had a reverse bias so that higher gains resulted in lower PMT sensitivity.
[31] Data on the PMTs used in this work was not available due to the model being discontinued.

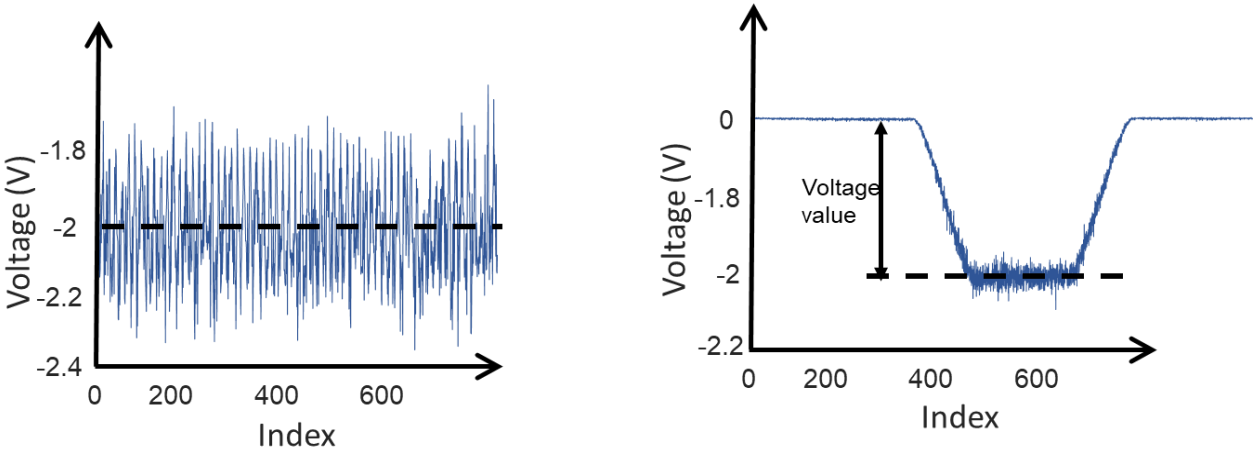

Figure C-6: PMT voltage: (a) without an optical chopper, and (b) with an optical chopper

Mansmann *et al*. [114] demonstrated the importance of evaluating the performance of the PMTs to ensure that all PMT responses are linear (i.e. PMT output is directly proportional to total irradiance) and to determine and avoid the range of PMT gains that introduce non-linear responses. To assess PMT non-linearity, five different neutral density (ND) filters (held in place by the optical filter wheel) with percent transmissions of 2%, 10 %, 30%, 60 %, 90 % and 100 %, corresponding to optical densities (OD) of 1.67, 1, 0.52, 0.22, 0.046 and 0, are used to alter the light levels incident on the PMTs. Figure C-7 shows the spectral transmissions for the ND filters.

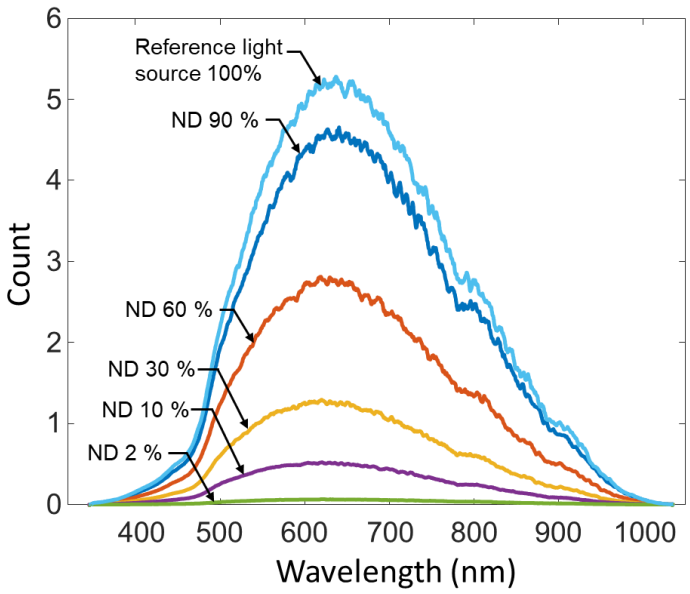

Figure C-7: Spectral transmissions of the ND filters.

Calibration data were collected for the three PMTs at gains between 350[32] to 900 for the blue[33] and red channels and between 400 to 900 for the yellow channel with increments of 50. At each gain, three data points are collected with three different ND filters to assess non-linearity and for statistical analysis. The measurement trials for the statistical analysis were obtained by applying the ND filter attenuation percentage to the voltage data to obtain the unattenuated light level voltages. At some gains, the PMT sensitivity was too low to collect data with three ND filters; in this scenario, the three data points were collected with one or two ND filters with some data points re-measured using one of the ND filters. The optical chopper was operated at 197 Hz.

Figure C-8 shows the data collected for each PMT and the associated error bars. Notice that the error bars are larger at higher gains since space charge effects are more significant at such gains (*cf.* §3.1.3.1).

[32] The intensity of the light source was not high enough to collect reliable data at gains lower than 350 for the blue and red channels and 400 for the yellow channel.

[33] The PMT channels with bandpass filters centered at 445 nm, 648 nm, and 747 nm are referred to as the blue, yellow and red channels, respectively, in this section.

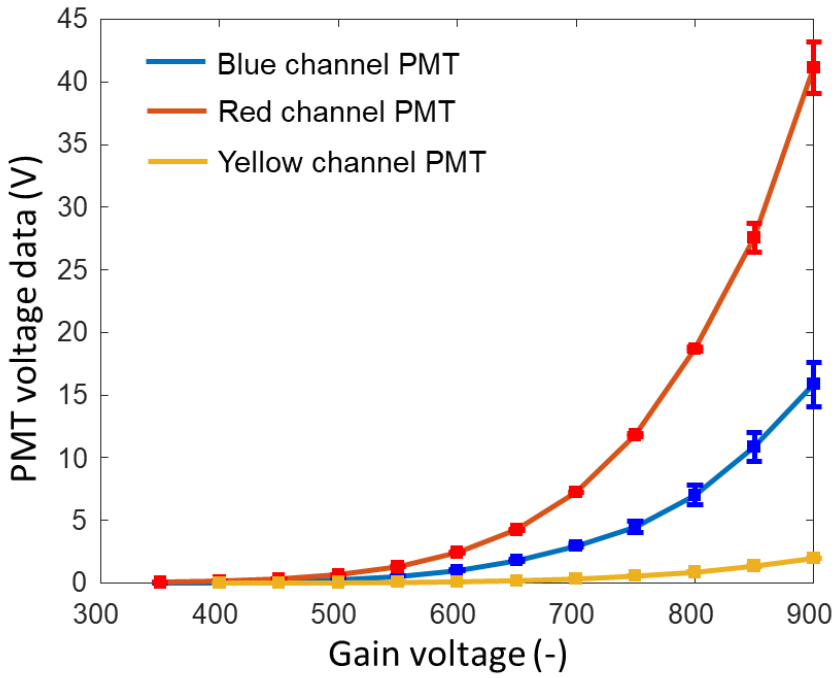

Figure C-8: PMT calibration data.

C.2.2 Evaluating PMT Performance

Evaluating the performance of the PMTs involved quantifying the deviation from linearity as a function of gains and light levels. The percent deviation from linearity is found using [114],

$$\left[\left(\frac{S(\tau_i)}{S(\tau_{\text{ref}})}\frac{\tau_{\text{ref}}}{\tau_i}\right)-1\right]100\%\,, \tag{C.1}$$

where $S(\tau_i)$, is the light signal from the PMT when an ND filter of transmission, τ_i, is used, normalized to signal of the lowest light level signal, $S(\tau_{\text{ref}})$ when the ND filter of the highest OD with transmission τ_{ref} is used. Figure C-9 shows the extent of non-linearity of each PMT as a function of gains and light levels. Only gains at which data were collected with more than one ND filter are shown.

As shown in Figure C-9, there is a larger deviation from linearity at higher gains for the PMTs on the blue and red channels. This trend is, however, not present for the PMT on the yellow channel, which deviates the least, with the largest deviation at the 500 gain, which can be attributed to the low light levels on the yellow channel due to the higher OD of the bandpass filter. Therefore, efforts were made to conduct experiments at gains with ±10% non-linearity. It should be noted that at lower gains, the PMTs were not sensitive enough to the available light intensity from the light source; hence, data collected with ND filters with ~10% transmission could introduce significant errors in the analysis. This could be an additional reason for the results at the 500 gain on the yellow channel PMT.

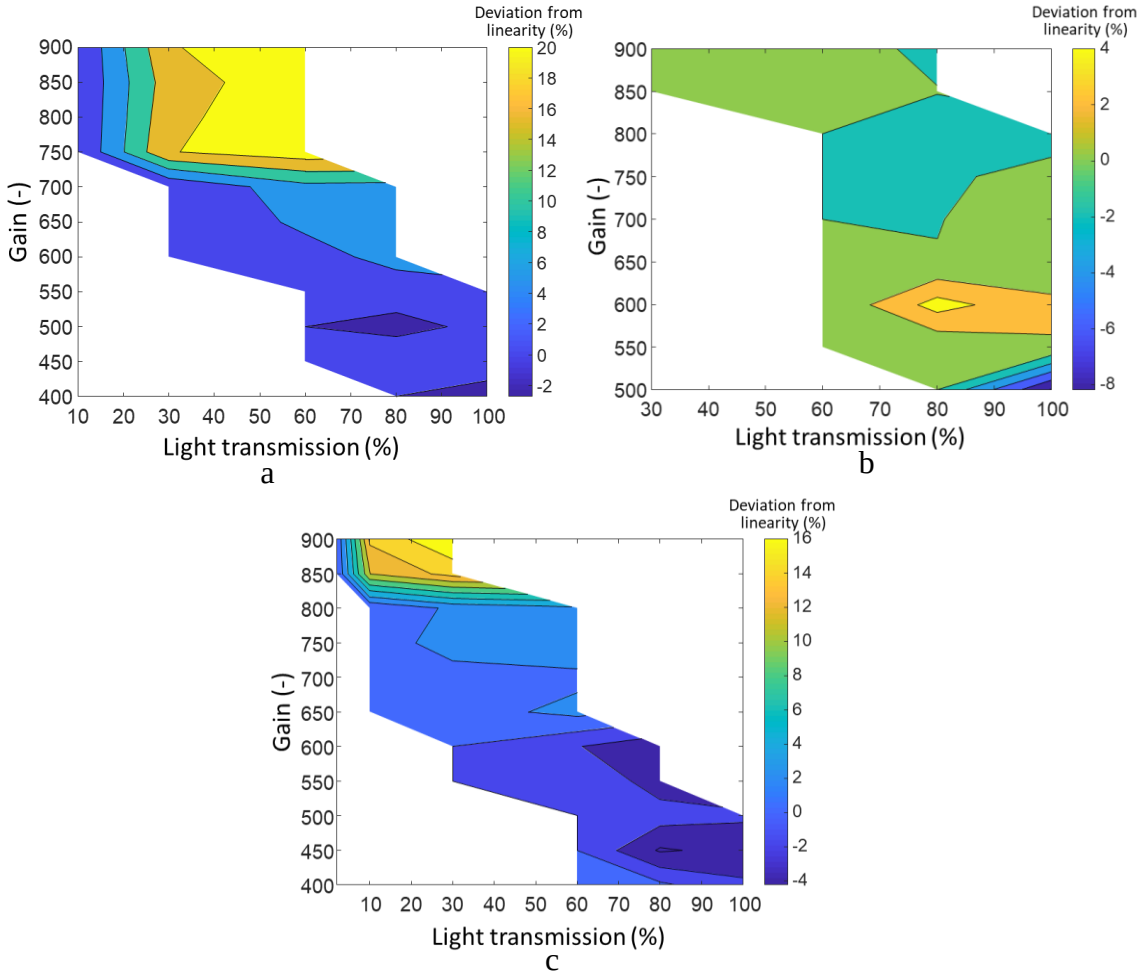

Figure C-9: Deviation from linearity for: (a) the blue channel PMT, (b) the yellow channel PMT, and (c) the red channel PMT.

C.2.3 Determining the calibration factors

A relative sensitivity calibration analysis similar to that performed by Mansmann *et al*. [66] is used in this study. Each PMT is calibrated for sensitivity, against a calibration light source and for gain, across all gains. The overarching idea is to relate how much voltage is induced on a PMT due to a known amount of incident irradiation and determine how this relation changes across PMT gains. The amount of irradiance, E_i, incident on the ith PMT within a wavelength bandwidth, $d\lambda$, is found by

$$E_i = \int_{\Delta\lambda_i} E^{\text{ref}}\left(\lambda\right) d\lambda \,, \tag{C.2}$$

where E^{ref} is the spectrum of the light source and $\Delta\lambda_i$ is the spectral bandwidth of the ith PMT bandpass filter. This will induce a PMT voltage, V_i^{meas} and the sensitivity calibration factor, D_i, is then defined as

$$D_i = \frac{\tau E_i}{V_i^{\text{meas}}} \,, \tag{C.3}$$

where τ is the transmission of any ND filter used.

The gain correction factor is found by modelling the PMT response according to [66],

$$\ln\left(V_i^{\text{meas}}\right) = A_i \ln\left(V_i^{\text{gain}}\right) + B_i \,, \tag{C.4}$$

where V_i^{gain} is the gain voltage (ranging from 1 – 1000) the PMT was set at when a voltage, V_i^{meas}, was induced due to an incident irradiation; A_i and B_i are coefficients in the response model. The coefficient, B_i, is eliminated by normalizing Eq. (C.4) to a reference gain, $V_i^{\text{ref,gain}}$ and its corresponding induced voltage, $V_i^{\text{ref,meas}}$,

$$\frac{V_i^{\text{meas}}}{V_i^{\text{ref,meas}}} = \left(\frac{V_i^{\text{gain}}}{V_i^{\text{gain,ref}}} \right)^{A_i} . \tag{C.5}$$

The gain correction factor, for the *i*th PMT at each gain voltage, can then be defined as

$$G_i\left(V_i^{\text{gain}}\right) = \left(\frac{V_i^{\text{gain}}}{V_i^{\text{gain,ref}}} \right)^{-A_i} , \tag{C.6}$$

such that $V_i^{\text{gain,ref}} = V_i^{\text{gain}} G_i\left(V_i^{\text{gain}}\right)$. The coefficient, A_i, is found by solving the weighted minimization problem,

$$A_i = \arg\min_{A_i} \left\{ \left\| \frac{V_i^{\text{meas}} - V_i^{\text{ref,meas}} \Big/ G\left(V_i^{\text{gain}}\right)}{\sigma_i^{\text{gain}}} \right\|_2^2 \right\}, \tag{C.7}$$

where σ_i^{gain} is the standard deviation of the data at each gain. Figure C-10 shows the coefficient, A_i, for each PMT.

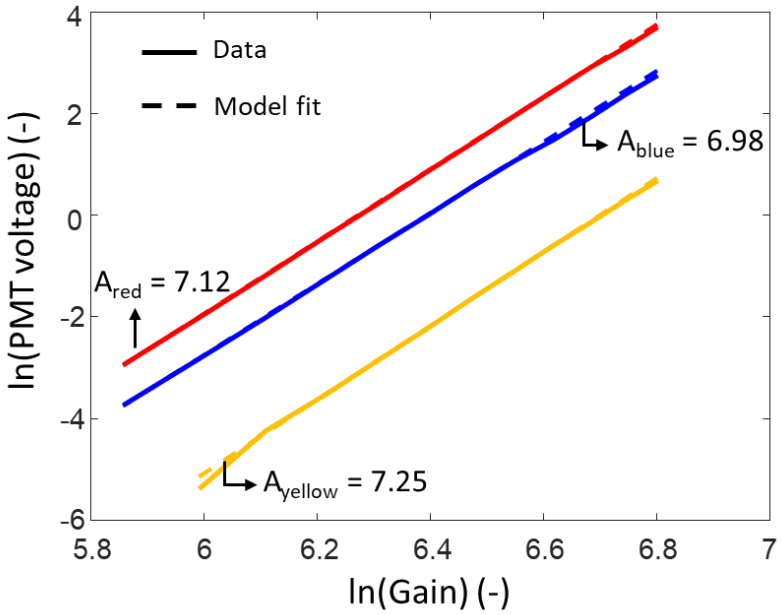

Figure C-10: Coefficient fit to PMT data.

One sensitivity calibration factor, D_i^{ref} , is determined at the reference gain and corrected by the gain correction factor, $G_i\left(V_i^{\text{gain}}\right)$; i.e. data at collected at any gain is corrected to what the response would be at the reference gain and then calibrated for sensitivity. Therefore, the calibrated experimental signal, J_i^{exp} , from the *i*th PMT, set at a gain, V_i^{gain} , is determined as

$$J_i^{\text{exp}} = D_i^{\text{ref}} G\left(V_i^{\text{gain}}\right) J_i^{\text{raw}} \ , \tag{C.8}$$

where J_i^{raw} are the raw experimental signals.

The 500 gain is chosen as the reference gain voltage as it is the half-way point for the range of all gains. Figure C-11 shows the calibration curve, $D_i^{\text{ref}} G\left(V_i^{\text{gain}}\right)$, of each PMT across all gains.

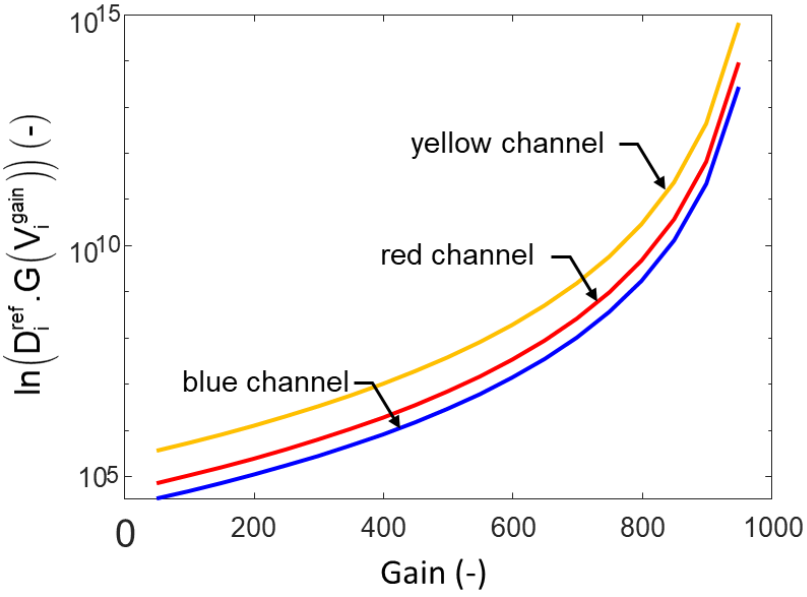

Figure C-11: Calibration constants over PMT gains.

C.3 Optical chain alignment

The laser path, detection solid angle and probe volume need to be aligned to ensure that the nanoparticles in the probe volume are being heated up within the focal point of the collection optics. The probe volume is defined by the focal point of the collection optics, which is determined

with the aid of the photodiode within the demultiplexer box (*cf.* Figure 3-7). After the collection optics focal point was determined, two laser diodes (L1 and L2) passing through irises (M1 and M2), positioned normal to each other, were aligned to intersect the probe volume, as seen in Figure C-12. The laser diodes add extra axes to aid laser alignment. To ensure that the laser beam does not damage the laser diodes, a pin object was placed at the probe volume to mark the intersection position, and all laser diodes were turned off and protected from the laser beam.

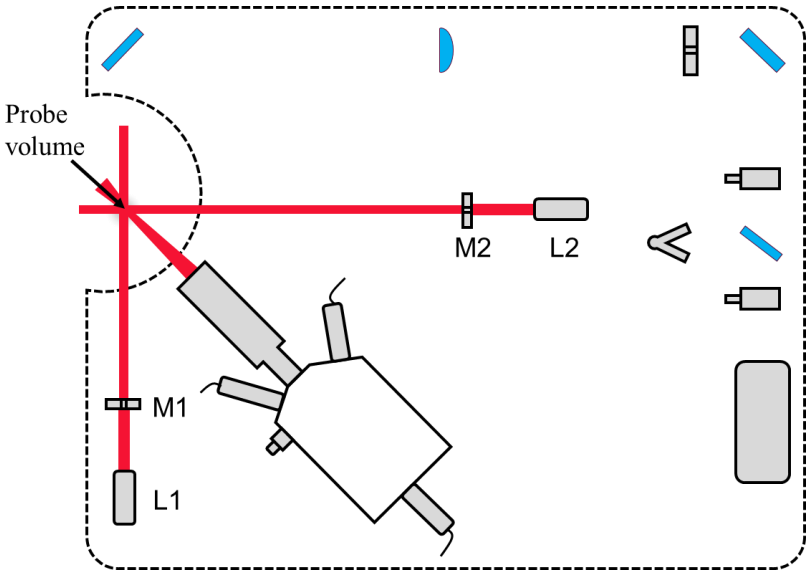

Figure C-12: Alignment laser diodes.

Once the probe volume was fully defined, the laser beam travels through each optical component in the optical chain while ensuring it is parallel to both the optical breadboard and the walls of the room. A burn paper was used to track the position of the beam. If the beam did not intersect the pin object at the probe volume (i.e., the alignment was off), the 1064 nm mirror (Figure 3-2, part I) or another appropriate component was adjusted until the pin object and beam intersected. Note, when the pin object was removed and the sample cell was set in place, the laser beam path was slightly altered due to refraction by the cell window; in which case, re-alignment

was done by ensuring the laser diode from the demultiplexer box intersects the laser beam on a burn paper.

C.4 Equipment validation

After calibrating the detection system and aligning the laser system, it was necessary to validate the calibration factors and ensure proper functioning of the laser system to guarantee that the experimental data is reliable. The validation experiment was conducted on a soot-laden aerosol as there are extensive data and results from soot experiments in the literature to validate the results. The soot temperatures and fluence curve were used as validation parameters.

C.4.1 Validation data collection

Two methods were explored for the generation of the soot aerosol. One method involved placing a box over a lamp to create a build-up of soot, as shown in Figure C-13(a). Gas flowing through a T-junction venturi induces a low-pressure point that acts as a suction to draw the soot particles into the upstream flow. The gas flow is directed into the sample cell, where soot particles are heated with the laser pulse. The second method involved placing the lamp so that the flame is within the probe volume; soot within the flame is then laser-heated. Figure C-13(b) shows this setup.

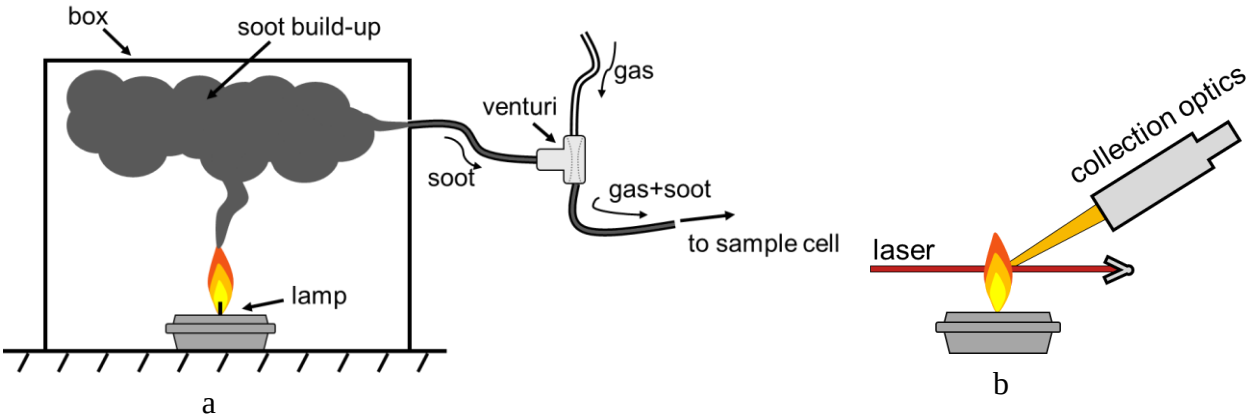

Figure C-13: Soot data collection using (a) box and venturi setup, and (b) direct soot flame.

However, the first method was not appropriate for data collection because the soot particles were significantly aggregated, to macroscopic particles, upon reaching the probe volume due to the travel time after soot formation. The significant soot aggregation needs to be accounted for as the absorption properties will differ from soot monomers [67,178]. Therefore, data from the second method were used for analysis. Data were collected at seven fluences to construct the soot fluence curve. At each fluence, at least 500 data shots[34] were recorded for statistical analysis. Due to the flame's flickering, some data shots did not capture incandescence and were eliminated from the analysis. To avoid PMT overexposure and damage during data collection, PMT gains were adjusted to ensure that the superposition of the signals resulting from the DC background radiation of the flame and pulsed radiation due to the laser-heated soot particles did not induce PMT voltages greater than those recommended by Table C-1.

C.4.2 Validation data analysis

Figure C-14(a) shows the raw uncalibrated incandescence data from the soot nanoparticles. As seen in Figure C-14(b), the relative magnitude of the signal on the yellow channel is lower than expected upon calibration. The expected range of temperatures of the soot particles, at the fluences used, is between 2000 K – 4500 K [61] and the spectral intensity of the incandescence should be similar to the Planck's distribution. Therefore, the relative magnitudes of the signals: Blue > Red > Yellow, will produce non-physical temperatures for soot particles, as discussed later on in this section.

The instantaneous spectral incandescence model (*cf.* Eq. (2.3)) can be fit to the data from all three channels at an instant of time to find the soot temperature and visually evaluate the relative

[34] Shots refer to one measurement of the experimental signal by the PMT.

channel magnitudes. The fitting is performed with data from selected pairs of channels, according to Table C-2. A wavelength-independent absorption function, $E(\mathbf{m}_\lambda)$, as suggested by Ref. [179], is used.

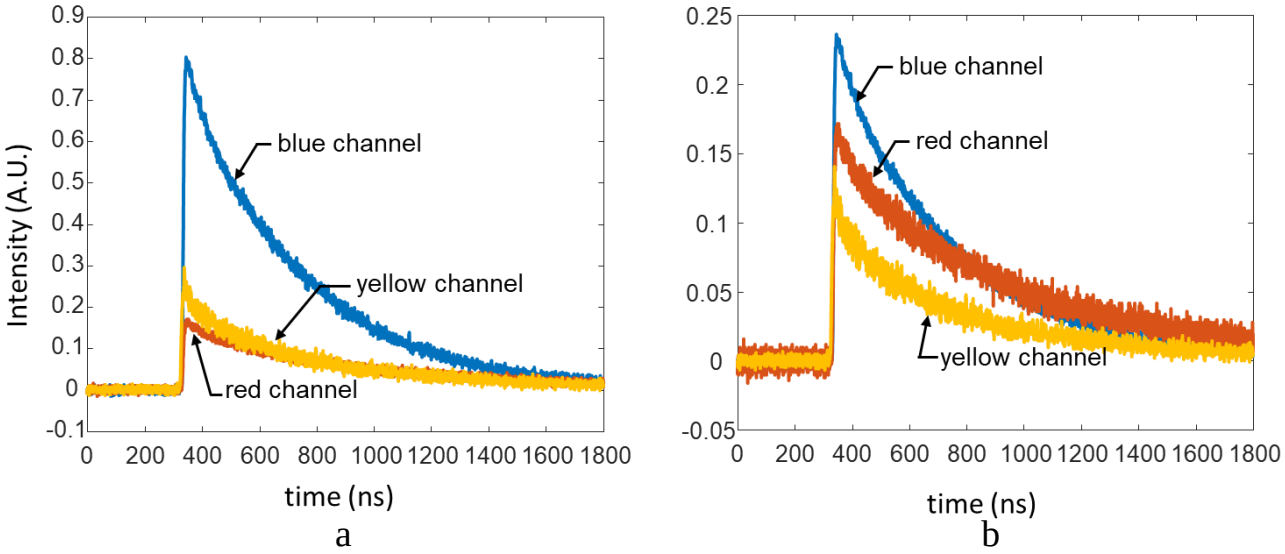

Figure C-14: LII data of flame soot irradiated with a fluence of 1.04 mJ/mm^2 (a) Raw (b) Calibrated. Calibration constants were normalized to the red channel.

Table C-2: Selected channels for model fit.

	Channels used
T1	blue and red
T2	blue and yellow
T3	yellow and red
T4	blue, yellow and red

The LM minimization algorithm is used to fit the data and is implemented in MATLAB® [107] using the "*lsqnonlin*" function. Figure C-15 shows the model fit to the data at 500 ns after peak incandescence; using data from the yellow channel to determine the soot temperature produces either too high (5805.8 K) or too low (1703.7 K) a temperature for soot irradiated at a fluence of 1.04 mJ/mm^2 [61].

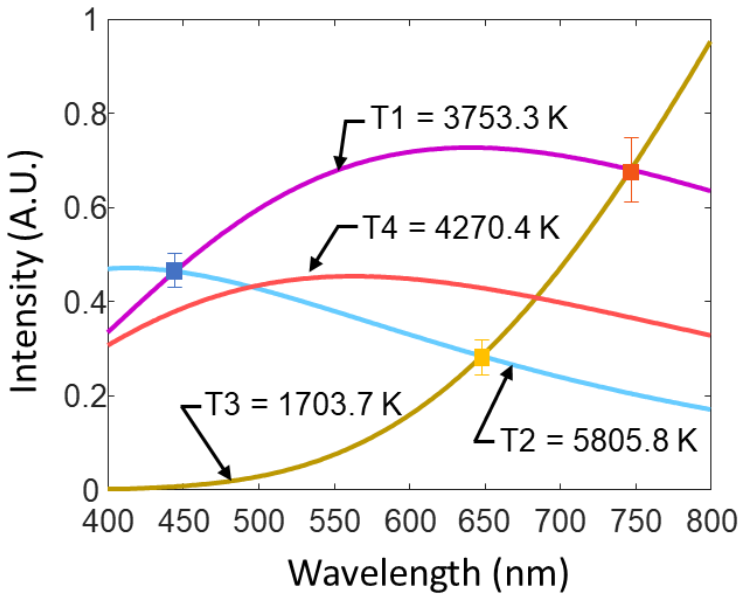

Figure C-15: Model fit to channel data at 500 ns after peak incandescence.

Plotting the pyrometric cooling temperature histories with channel pairs, as shown in Figure C-16 below, shows a similar disagreement for T1, T2 and T3 in Figure C-15, and a non-physical temperature of 6,000 K is computed from the blue and yellow channel pair.

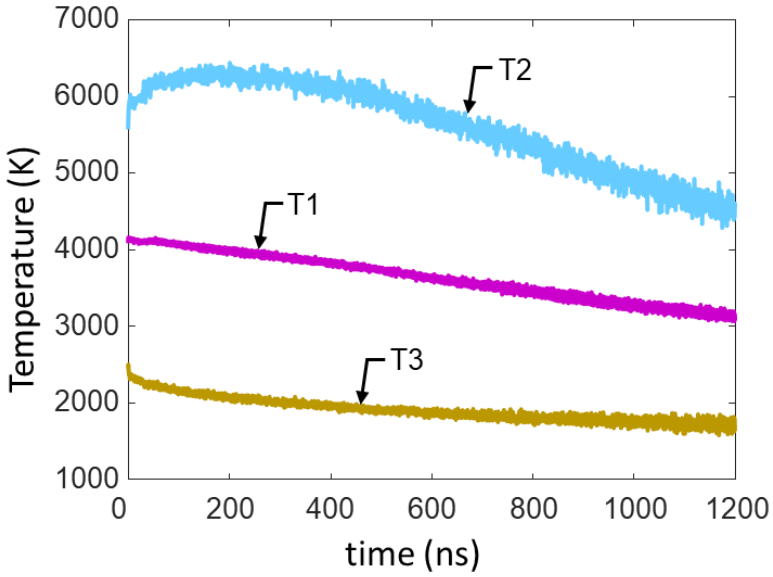

Figure C-16: Pyrometric temperature profiles of flame soot nanoparticles. Error bars have been omitted for clarity.

Troubleshooting the problem with the yellow (648 nm) channel involved the following:

1. The spectrometer was placed at the PMT port of the yellow channel on the demultiplexer box to capture the spectrum of the irradiation incident on the PMT in this channel. Although the obtained spectrum differed slightly from that achieved from convoluting the transmission spectra of the bandpass filter and dichroic mirror, results were similar.
2. The 648 nm bandpass filter was replaced by a 557 nm 100 % transmission bandpass filter. Data was collected from flame soot generated by a burner generating a laminar co-flow ethylene diffusion flame, with fuel and airflow rates similar to Ref [21]. This troubleshooting attempt took place at NRC. Although the deviation of the channel decreased slightly, the problem persisted.

After all troubleshooting attempts yielded similar results for the third colour channel, it was concluded that quantitative research work would be conducted with only two colours with detection wavelengths at 445 nm (blue) and 747 nm (red). To ensure that the two-colour detection system was indeed working appropriately, a fluence study was conducted with the lamp flame soot, as shown in Figure C-17. The sublimation temperature of soot (plateau regime) is around 4450 K [61], further verifying the calibration for a working two-colour detection system. The integrated intensity as a function of fluence, shown in Figure C-18, also shows soot sublimation at the higher fluence since the integrated intensity drops due to mass loss at higher fluences.

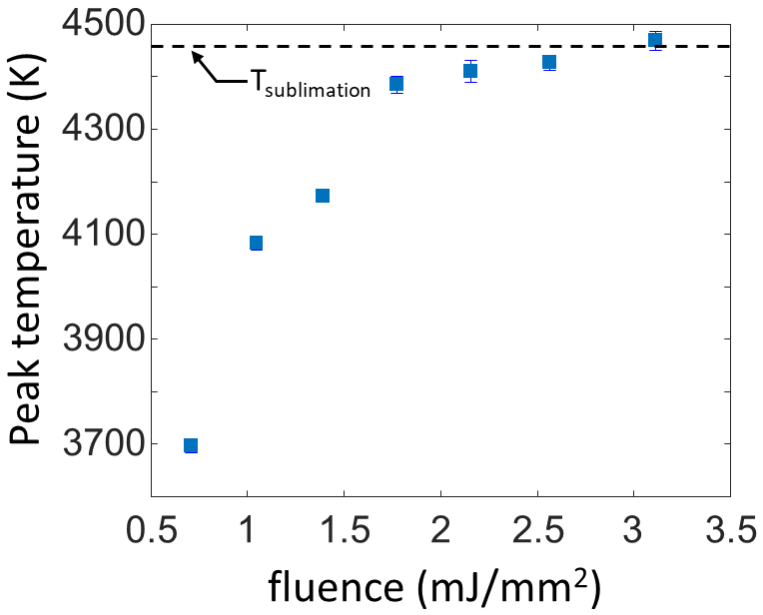

Figure C-17: Fluence curve of lamp flame soot obtained from two-colour pyrometry with detection wavelengths, 445 nm and 747 nm. Error bars are three standard deviations of the mean.

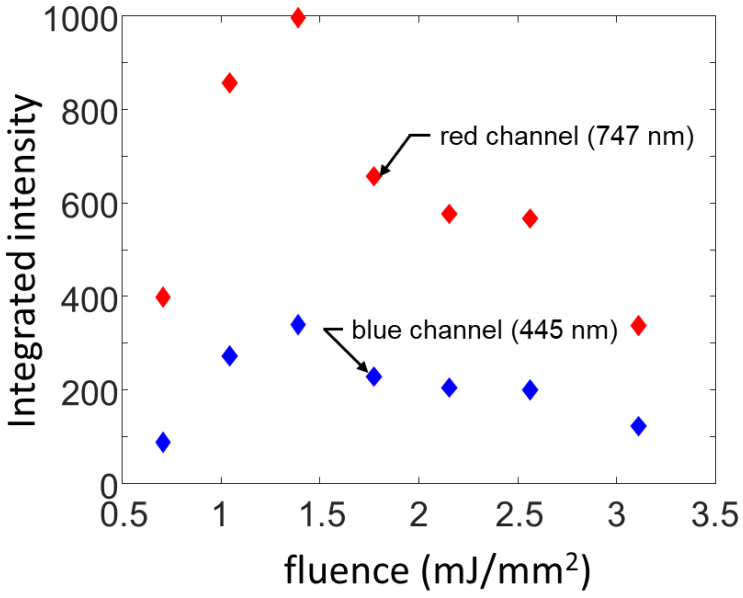

Figure C-18: Integrated intensities at various fluences.

Appendix D

Conduction related information

D.1 Knudsen number determination

The Knudsen number, *Kn*, is computed to determine what conduction regime the nanoparticles are cooling. The Knudsen number is computed by $Kn = \lambda_{MFP}/L$, where λ_{MFP} is the mean free path (MFP) and L is the characteristic length, which is taken as the radius, for a spherical nanoparticle [91]. The characteristic length of aggregates is complicated to determine but some researchers have used the concept of an equivalent sphere [70]. Although there are multiple ways to calculate the MFP [91], in this work, it is determined by [151]

$$\lambda_{MFP} = \frac{k_B T_g}{\sqrt{2}\sigma_g p_g}, \tag{C.9}$$

where, k_B is Boltzmann constant, T_g and p_g are the temperature and pressure of the gas, respectively and σ_g is the collision cross-section informed by the variable hard sphere (VHS) of the molecule. The VHS of the gas molecules are taken from Ref [157].

D.2 Inferred TACs from all nanoaerosols at all fluences

The inferred TACs from all nanoaerosols at each fluence is shown in Figure D-1. Only TACs at lower fluences (shaded area in Figure D-1) were averaged to produce the inferred TACs shown in Figure 5-11 as these results were more reliable than results at higher fluences as informed from the results of the inferred size distribution.

The variance of each inferred TAC were computed from Eq. (A.9). The uncertainty of the average TAC is computed according to,

$$\frac{1}{\sqrt{n}}\left[\sum_{i=1}^{n}\sigma_{(x,x)_i}\right]^{1/2}, \tag{C.10}$$

where $\sigma_{(x,x)i}$ is the variance of each TAC data point, x, and n is the number of data points that are averaged.

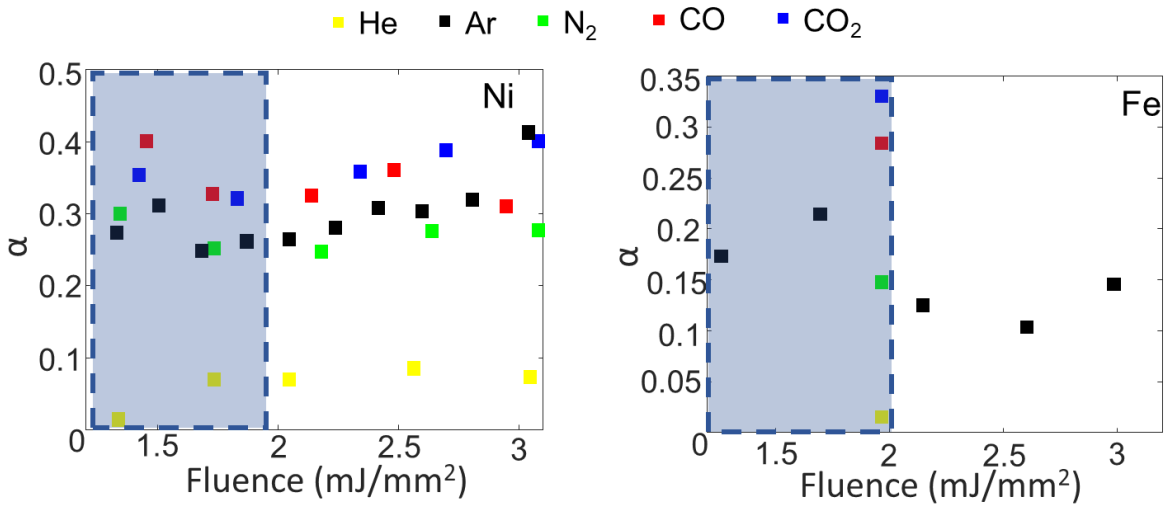

Figure D-1: TACs inferred for all nanoaerosols at all fluences.

D.3 Fitting procedure to exponential conduction cooling

The TAC inference procedure developed by Daun *et al*. [56] equated the internal energy of the nanoparticle to the heat conduction from the nanoparticle, modelled in the FMR,

$$\rho_{\mathrm{p}}\left(T_{\mathrm{p}}\right)c_{\mathrm{p}}\left(T_{\mathrm{p}}\right)\frac{\pi d_{\mathrm{p}}^3}{6}\frac{d\left(T_{\mathrm{p}}\left(t\right)\right)}{dt}=-\alpha\pi d_{\mathrm{p}}^2\frac{1}{4}\frac{p_{\mathrm{g}}}{k_{\mathrm{B}}T_{\mathrm{g}}}\sqrt{\frac{8k_{\mathrm{B}}T_{\mathrm{g}}}{\pi m_{\mathrm{g}}}}\left(2+\frac{\zeta_{\mathrm{rot}}}{2}\right)k_{\mathrm{B}}\left(T_{\mathrm{p}}-T_{\mathrm{g}}\right). \tag{C.11}$$

Letting $\theta(t) = T_{\mathrm{p}} - T_{\mathrm{g}}$ and re-arranging,

$$\frac{d\left(\theta\left(t\right)\right)}{dt}=\alpha C_1\theta\left(t\right), \tag{C.12}$$

where

$$C_1=-\pi d_{\mathrm{p}}^2\frac{1}{4}\frac{p_{\mathrm{g}}}{k_{\mathrm{B}}T_{\mathrm{g}}}\sqrt{\frac{8k_{\mathrm{B}}T_{\mathrm{g}}}{\pi m_{\mathrm{g}}}}\left(2+\frac{\zeta_{\mathrm{rot}}}{2}\right)k_{\mathrm{B}}\left[\rho_{\mathrm{p}}\left(T_{\mathrm{p}}\right)c_{\mathrm{p}}\left(T_{\mathrm{p}}\right)\frac{\pi d_{\mathrm{p}}^3}{6}\right]^{-1}. \tag{C.13}$$

Solving Eq. (C.12) results in

$$\ln\theta(t) = \alpha C_1 t + C_2, \tag{C.14}$$

where C_2 is a constant of integration. This allows for a simplified linear temperature model in time where α and C_2 can be solved through linear regression. By defining an average diameter size class in the nanoaerosol, α and C_2 were inferred using the Bayesian framework (with no priors) and the trust-region reflective algorithm, implemented in MATLAB® [107] using the "*lsqnonlin*" function, with upper and lower bounds. Figure D-2 shows a fit to a dataset.

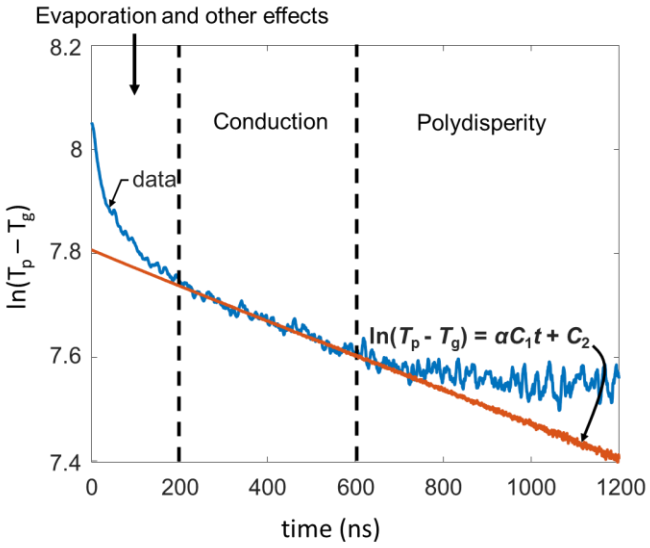

Figure D-2: Linear model fit to exponential conduction.

There are three clearly defined regimes of cooling, namely, evaporation and other effects, conduction, and polydispersity. The other effects in the evaporation regime refer to other non-incandescent signals that may be corrupting the prompt signals. The conduction regime is the section of the data that is expected to be linear in the log space, and polydispersity effects begin to take effect at much later cooling times. The linear model fit to the data in Figure D-2 was performed between 200 ns and 600 ns, chosen by visual approximation. A change to this time window could alter the inferred parameters significantly. This subjectivity introduced uncertainties in the inference procedure.

Appendix E

Additional supplemental information

E.1 Relationship between refractive indices, optical conductivity and dielectric constant

The refractive indices of Ni and Fe presented in §2.1 were computed from the values of the real component of the dielectric function and the optical conductivity reported by Krishnan *et al*. [76]. For a non-magnetic material (the liquid metals lose their ferromagnetism since they are above their Curie temperature [76]), the real component of the dielectric function, $\varepsilon_{I,\lambda}$ and the optical conductivity, σ_λ, are given as [76],

$$\varepsilon_{1,\lambda} = n_\lambda^2 + k_\lambda^2 , \tag{C.15}$$

$$\sigma_\lambda = 4\pi\varepsilon_0 n_\lambda k_\lambda \nu , \tag{C.16}$$

where n_λ and k_λ are the components of the complex index of refraction, ε_0 is vacuum permittivity, and ν is the frequency; $\nu = c_0/\lambda$, where c_0 is the speed of light and λ is the wavelength. The imaginary component of the dielectric function, $\varepsilon_{II,\lambda}$ is given as [180],

$$\varepsilon_{II,\lambda} = 2 n_\lambda k_\lambda , \tag{C.17}$$

so Eq (C.16) becomes,

$$\varepsilon_{II,\lambda} = \frac{\sigma_\lambda \lambda}{2\pi\varepsilon_0 c_0} . \tag{C.18}$$

Then n and k can be computed from [180],

$$n_\lambda = \sqrt{\frac{\left\|\boldsymbol{\varepsilon}_\lambda\right\| + \varepsilon_{I,\lambda}}{2}} , \tag{C.19}$$

$$k_\lambda = \sqrt{\frac{\|\boldsymbol{\varepsilon}_\lambda\| - \varepsilon_{\mathrm{I},\lambda}}{2}}, \tag{C.20}$$

where $\|\boldsymbol{\varepsilon}\|$ is the norm of the dielectric function; $\|\boldsymbol{\varepsilon}_\lambda\| = \sqrt{\varepsilon_{\mathrm{I},\lambda}^2 + \varepsilon_{\mathrm{II},\lambda}^2}$.

E.2 Q-switch noise removal

The Q-switch is a method of producing a pulsed laser output through controlled stimulated emission (*cf.* §3.1.1); this creates an electromagnetic interference that the PMTs detect, i.e. the Q-switch noise. The Q-switch noise from the laser head was removed from all datasets. This noise was non-random and structured since it had the same unchanging form with every shot. Figure E-1 shows the data, the Q-switch noise, and the data with the Q-switch noise removed. The Q-switch noise was removed by subtracting it from the data before calibration factors are applied. However, because the data and the Q-switch noise are not taken synchronously, there could be a mismatch in peaks, which would alter the data after removal. For this reason, the noise peaks in the data and the peaks in the Q-switch noise need to be matched before noise removal.

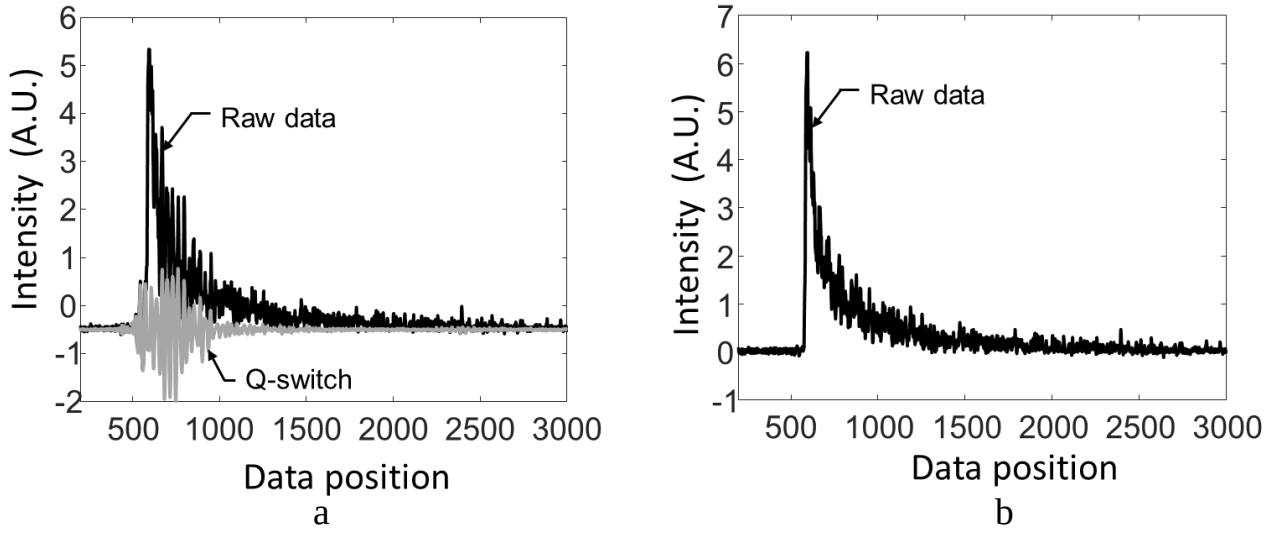

Figure E-1: (a) Raw data and Q-switch noise with peaks matched, and (b) raw data with Q-switch removed from one channel.

E.3 Absence of non-linearities in data across PMT gains

The calibration constants are derived under conditions that the induced current output by the PMTs are proportional to the intensity of the incident light; however, space charge effects at high gains and non-linear behaviours at lower light levels can affect the PMT responses during experiments and introduce non-linearities that affect the PMT data [66]. PMT data for a defined experimental condition are expected to yield the same result regardless of the gains used during experiments. Figure E-2 shows the pyrometric temperature profiles from three datasets collected at three different sets of PMT gains for the same experimental condition. All the datasets at all set of gains produce the same temperature histories (within uncertainty), showing that there were no non-linearities were present during data collection and further validating the calibration factors.

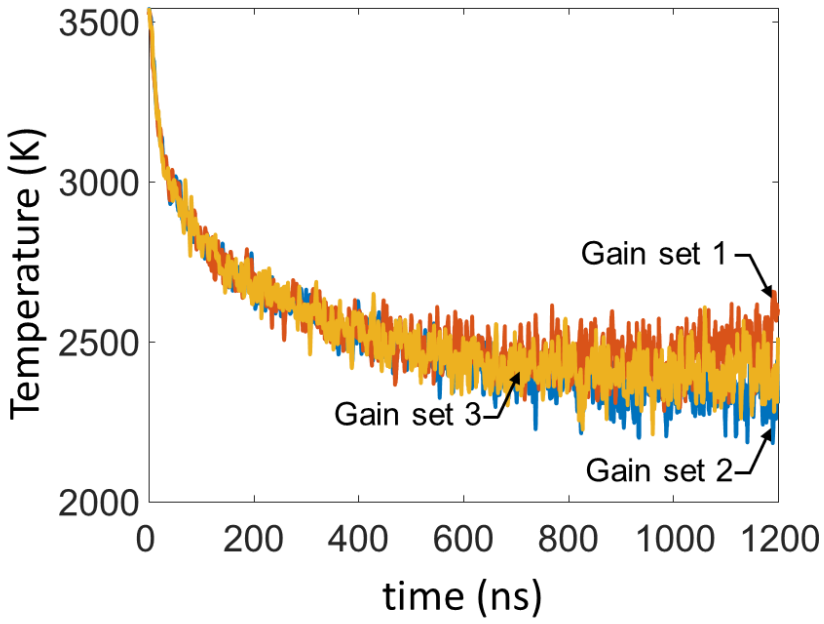

Figure E-2: Pyrometric temperature histories at different set of PMT gains.

E.4 Covariance of the data

Figure E-3 shows that the covariance of the data is diagonally dominant (i.e. high variances), which could allow for a diagonal approximation (i.e. independently distributed data) although, because there were high covariances close to the diagonal, the covariance matrix was approximated with ten covariances on either side of the variance diagonal.

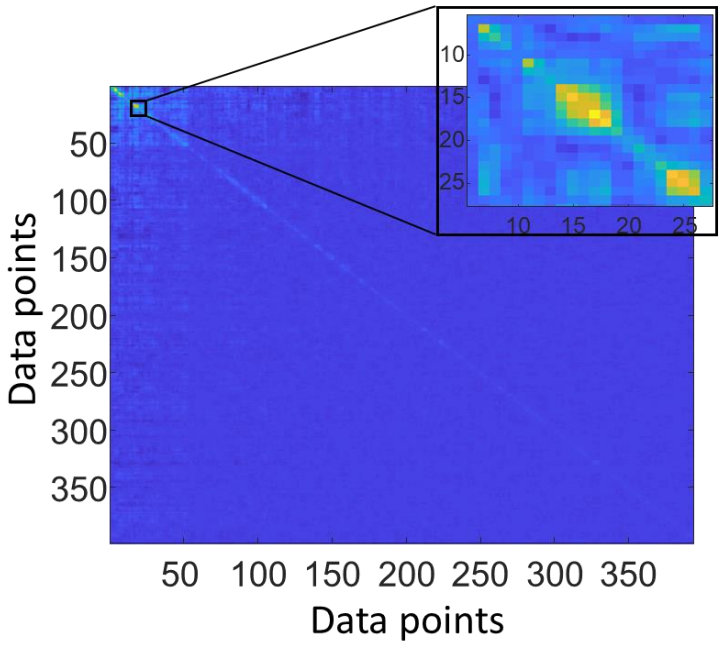

Figure E-3: Covariance of incandescence shot dataset from one PMT.

The covariance matrix, from *n* observations of *m* random variables is computed according to,

$$\mathbf{\Gamma}_{\mathrm{b}} = \frac{1}{n}\sum_{i=1}^{n}\left(\mathbf{X}_i - \overline{\mathbf{X}}\right)\left(\mathbf{X}_i - \overline{\mathbf{X}}\right)^{\mathrm{T}}, \tag{C.21}$$

where $\mathbf{\Gamma}_{\mathrm{b}}$, is the data covariance matrix of dimension, $\mathbf{\Gamma}_{\mathrm{b}} \in \mathbb{R}^{m\times m}$, $\mathbf{X}$ is the data matrix of dimension, $\mathbf{X} \in \mathbb{R}^{n\times m}$ and $\overline{\mathbf{X}}$ is the mean of the random variables from all observations with dimension, $\overline{\mathbf{X}} \in \mathbb{R}^{1\times m}$.

E.5 Data from LII 300 Artium Technologies

The LII data from the plasmonic nanoparticles obtained from the in-house TiRe-LII apparatus used in this work were compared to the LII data obtained from the LII 300 to access the duration of the signals. Figure E-4 compares the LII data obtained from both apparatus. The LII 300 broadens the short duration signal, which the in-house TiRe-LII apparatus accurately captures. However, the LII 300 has more sensitivity than the in-house TiRe-LII apparatus because there were detectable signals from significantly dilute nanocolloids which was not the case for the TiRe-LII. This shows that the design of the LII 300 traded fast response for sensitivity and the amplifiers used to accomplish this introduced signal sampling delay that broadens the signals. The LII 300 was built in this way because it was meant to detect soot at very low concentrations. The temporal blending did not affect soot signal decay since the signals were due to incandescence, which generally have much longer signal decay.

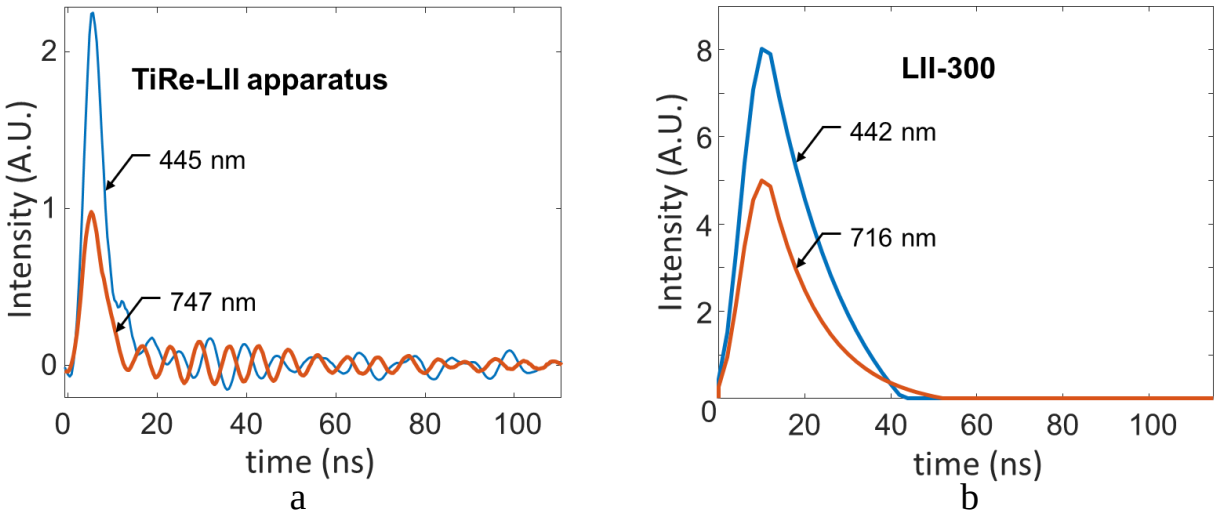

Figure E-4: Comparing signals from Ag nanoparticles from (a) In-house TiRe-LII apparatus and (b) LII 300 Artium Technologies.

References

[1] Environment_Canada, Health_Canada. Priority Substances List Assessment Report for Respirable Particulate Matter. 2000.

[2] Gomes JFP, Albuquerque PCS, Miranda RMM, Vieira MTF. Determination of Airborne Nanoparticles from Welding Operations. J Toxicol Environ Heal Part A 2012;75:747–55. https://doi.org/10.1080/15287394.2012.688489.

[3] Chow JC. Measurement Methods to Determine Compliance with Ambient Air Quality Standards for Suspended Particles. J Air Waste Manage Assoc 1995;45:320–82. https://doi.org/10.1080/10473289.1995.10467369.

[4] Roco MC. Nanoparticles and nanotechnology research. vol. 1. 1999.

[5] Elahi N, Kamali M, Baghersad MH. Recent biomedical applications of gold nanoparticles: A review. Talanta 2018;184:537–56. https://doi.org/10.1016/j.talanta.2018.02.088.

[6] Kievit FM, Veiseh O, Bhattarai N, Fang C, Gunn JW, Lee D, *et al*. PEI-PEG-chitosan-copolymer-coated iron oxide nanoparticles for safe gene delivery: Synthesis, complexation, and transfection. Adv Funct Mater 2009;19:2244–51. https://doi.org/10.1002/adfm.200801844.

[7] Lal S, Link S, Halas NJ. Nano-optics from sensing to waveguiding. Nat Photonics 2007;1:641–8. https://doi.org/10.1038/nphoton.2007.223.

[8] Stark WJ, Stoessel PR, Wohlleben W, Hafner A. Industrial applications of nanoparticles. Chem Soc Rev 2015;44:5793–805. https://doi.org/10.1039/c4cs00362d.

[9] Patel AR, Vavia PR. Nanotechnology and pharmaceutical inhalation aerosols. vol. 45. 2007.

[10] Athanassiou EK, Grass RN, Stark WJ. Aerosol Science and Technology Chemical Aerosol Engineering as a Novel Tool for Material Science: From Oxides to Salt and Metal Nanoparticles Chemical Aerosol Engineering as a Novel Tool for Material Science: From Oxides to Salt and Metal Nanoparticles. Aerosol Sci Technol 2010;44:161–72. https://doi.org/10.1080/02786820903449665.

[11] Biskos G, Vons V, Yurteri CU, Schmidt-Ott A. Generation and sizing of particles for aerosol-based nanotechnology. KONA Powder Part J 2008;26:13–35. https://doi.org/10.14356/kona.2008006.

[12] Tavakoli F, Olfert JS. An Instrument for the Classification of Aerosols by Particle Relaxation Time: Theoretical Models of the Aerodynamic Aerosol Classifier. Aerosol Sci Technol 2013;47:916–26. https://doi.org/10.1080/02786826.2013.802761.

[13] Stephens M, Turner N, Sandberg J. Particle identification by laser-induced incandescence in a solid-state laser cavity. Appl Opt 2003;42:3726. https://doi.org/10.1364/ao.42.003726.

[14] Sipkens TA, Hadwin PJ, Grauer SJ, Daun KJ. Predicting the heat of vaporization of iron at high temperatures using time-resolved laser-induced incandescence and Bayesian model selection. J Appl Phys 2018;123. https://doi.org/10.1063/1.5016341.

[15] Canadian Environmental Quality Guidelines Canadian Council of Ministers of the Environment. 1999.

[16] Tsuzuki T. Commercial scale production of inorganic nanoparticles. Int J Nanotechnol 2009;6:567–78. https://doi.org/10.1504/IJNT.2009.024647.

[17] Kammler HK, Mädler L, Pratsinis SE. Flame synthesis of nanoparticles. Chem Eng Technol 2001;24:583–96. https://doi.org/10.1002/1521-4125(200106)24:6<583::AID-CEAT583>3.0.CO;2-H.

[18] Weeks RW, Duley WW. Aerosol-particle sizes from light emission during excitation by TEA CO 2 laser pulses ARTICLES YOU MAY BE INTERESTED IN. J Appl Phys 1974;45:4661. https://doi.org/10.1063/1.1663111.

[19] Boiarciuc A, Foucher F, Mounaïm-Rousselle C. Soot volume fractions and primary particle size estimate by means of the simultaneous two-color-time-resolved and 2D laser-induced incandescence. Appl Phys B Lasers Opt 2006;83:413–21. https://doi.org/10.1007/s00340-006-2236-8.

[20] Hadwin PJ, Sipkens TA, Thomson KA, Liu F, Daun KJ. Quantifying uncertainty in soot volume fraction estimates using Bayesian inference of auto-correlated laser-induced incandescence measurements. Appl Phys B Lasers Opt 2016;122:1–16. https://doi.org/10.1007/s00340-015-6287-6.

[21] Snelling DR, Liu F, Smallwood GJ, Gülder ÖL. Determination of the soot absorption function and thermal accommodation coefficient using low-fluence LII in a laminar coflow ethylene diffusion flame. Combust Flame 2004;136:180–90. https://doi.org/10.1016/j.combustflame.2003.09.013.

[22] Bauer FJ, Daun KJ, Huber FJT, Will S. Can soot primary particle size distributions be determined using laser-induced incandescence? Appl Phys B Lasers Opt 2019;125. https://doi.org/10.1007/s00340-019-7219-7.

[23] Melton LA. Soot diagnostics based on laser heating. Appl Opt 1984;23:2201. https://doi.org/10.1364/AO.23.002201.

[24] Vander Wal RL, Ticich TM, West JR. Laser-induced incandescence applied to metal nanostructures. Appl Opt 1999;38:5867. https://doi.org/10.1364/ao.38.005867.

[25] Murakami Y, Sugatani T, Nosaka Y. Laser-induced incandescence study on the metal aerosol particles as the effect of the surrounding gas medium. J Phys Chem A 2005;109:8994–9000. https://doi.org/10.1021/jp058044n.

[26] Kock BF, Kayan C, Knipping J, Orthner HR, Roth P. Comparison of LII and TEM sizing

during synthesis of iron particle chains. Proc Combust Inst 2005;30:1689–97. https://doi.org/10.1016/j.proci.2004.07.034.

[27] Gurentsov E V., Eremin A V. Size measurement of carbon and iron nanoparticles by laser induced incadescence. High Temp 2011;49:667–73. https://doi.org/10.1134/S0018151X11050087.

[28] Menser J, Daun K, Dreier T, Schulz C. Laser-induced incandescence from laser-heated silicon nanoparticles. Appl Phys B 2016;122:277. https://doi.org/10.1007/s00340-016-6551-4.

[29] Sipkens TA, Singh NR, Daun KJ. Time-resolved laser-induced incandescence characterization of metal nanoparticles. Appl Phys B Lasers Opt 2017;123. https://doi.org/10.1007/s00340-016-6593-7.

[30] Gelbwachs J, Birnbaum M. Fluorescence of Atmospheric Aerosols and Lidar Implications. Appl Opt 1973;12:2442. https://doi.org/10.1364/ao.12.002442.

[31] Zinn B, Bowman C, Hartley D, Price E, Skifstad J. Experimental Diagnostics in Gas Phase Combustion Systems. New York: American Institute of Aeronautics and Astronautics; 1977. https://doi.org/10.2514/4.865275.

[32] Eckbreth AC. Effects of laser-modulated particulate incandescence on Raman scattering diagnostics ARTICLES YOU MAY BE INTERESTED IN. J Appl Phys 1977;48:4473. https://doi.org/10.1063/1.323458.

[33] Schulz C, Kock BF, Hofmann M, Michelsen H, Will S, Bougie B, *et al*. Laser-induced incandescence: Recent trends and current questions. Appl Phys B Lasers Opt 2006;83:333–54. https://doi.org/10.1007/s00340-006-2260-8.

[34] Roth P, Filippov A V. In situ ultrafine particle sizing by a combination of pulsed laser heatup and particle thermal emission. J Aerosol Sci 1996;27:95–104. https://doi.org/10.1016/0021-8502(95)00531-5.

[35] Snelling DR, Smallwood GJ, Gülder ÖL, Bachalo WD, Sankar S. Soot Volume Fraction Characterization Using the Laser-Induced Incandescence Detection Method. 2000.

[36] Boiarciuc A, Foucher F, Mounaïm-Rousselle C. Soot volume fractions and primary particle size estimate by means of the simultaneous two-color-time-resolved and 2D laser-induced incandescence. Appl Phys B 2006;83:413. https://doi.org/10.1007/s00340-006-2236-8.

[37] Michelsen HA, Schulz C, Smallwood GJ, Will S. Laser-induced incandescence: Particulate diagnostics for combustion, atmospheric, and industrial applications. Prog Energy Combust Sci 2015;51:2–48. https://doi.org/10.1016/j.pecs.2015.07.001.

[38] Michelsen HA, Liu F, Kock BF, Bladh H, Boiarciuc A, Charwath M, *et al*. Modeling laser-induced incandescence of soot: A summary and comparison of LII models. Appl Phys B Lasers Opt 2007;87:503–21. https://doi.org/10.1007/s00340-007-2619-5.

[39] Filippov A V, Markus MW, Roth P. In-situ characterization of ultrafine particles by laser-induced incandescence : sizing and particle structure determination 1999;30:71–87.

[40] Sipkens T, Joshi G, Daun KJ, Murakami Y. Sizing of molybdenum nanoparticles using time-resolved laser-induced incandescence. J Heat Transfer 2013;135. https://doi.org/10.1115/1.4023227.

[41] Starke R, Kock B, Roth P. Nano-particle sizing by laser-induced-incandescence (LII) in a shock wave reactor. Shock Waves 2003;12:351–60. https://doi.org/10.1007/s00193-003-0178-1.

[42] Eremin A, Gurentsov E, Mikheyeva E, Priemchenko K. Experimental study of carbon and iron nanoparticle vaporization under pulse laser heating. Appl Phys B Lasers Opt 2013;112:421–32. https://doi.org/10.1007/s00340-013-5530-2.

[43] Daun KJ. Thermal accommodation coefficients between polyatomic gas molecules and soot in laser-induced incandescence experiments. Int J Heat Mass Transf 2009;52:5081–9. https://doi.org/10.1016/j.ijheatmasstransfer.2009.05.006.

[44] Daun KJ, Titantah JT, Karttunen M. Molecular dynamics simulation of thermal accommodation coefficients for laser-induced incandescence sizing of nickel particles 2012:221–8. https://doi.org/10.1007/s00340-012-4896-x.

[45] Daun KJ, Titantah JT, Karttunen M. Erratum to : Molecular dynamics simulation of thermal accommodation coefficients for laser-induced incandescence sizing of nickel particles 2013:599–600. https://doi.org/10.1007/s00340-013-5403-8.

[46] Daun KJ, Sipkens TA, Titantah JT, Karttunen M. Thermal accommodation coefficients for laser-induced incandescence sizing of metal nanoparticles in monatomic gases 2013:409–20. https://doi.org/10.1007/s00340-013-5508-0.

[47] Sipkens TA, Singh NR, Daun KJ, Bizmark N, Ioannidis M. Examination of the thermal accommodation coefficient used in the sizing of iron nanoparticles by time-resolved laser-induced incandescence. Appl Phys B Lasers Opt 2015;119:561–75. https://doi.org/10.1007/s00340-015-6022-3.

[48] Sipkens TA, Daun KJ, Titantah JT, Karttunen M. Quantifying the thermal accommodation coefficient for iron surfaces using molecular dynamics simulations. ASME Int. Mech. Eng. Congr. Expo. Proc., vol. 8B-2015, American Society of Mechanical Engineers (ASME); 2015. https://doi.org/10.1115/IMECE2015-52150.

[49] Sipkens TA, Mansmann R, Daun KJ, Petermann N, Titantah JT, Karttunen M, *et al*. In situ nanoparticle size measurements of gas-borne silicon nanoparticles by time-resolved laser-induced incandescence. Appl Phys B Lasers Opt 2014;116:623–36. https://doi.org/10.1007/s00340-013-5745-2.

[50] Altman I. On energy accommodation coefficient of gas molecules on metal surface at high temperatures. Surf Sci 2020;698:121609. https://doi.org/10.1016/j.susc.2020.121609.

[51] Eremin A, Gurentsov E, Popova E, Priemchenko K. Size dependence of complex refractive index function of growing nanoparticles. Appl Phys B Lasers Opt 2011;104:285–95. https://doi.org/10.1007/s00340-011-4420-8.

[52] Beyer V, Greenhalgh DA. Laser induced incandescence under high vacuum conditions. Appl Phys B Lasers Opt 2006;83:455–67. https://doi.org/10.1007/s00340-006-2238-6.

[53] Wal RL Vander. Laser-induced incandescence: excitation and detection conditions, material transformations and calibration. Appl Phys B 2009;96:601–11. https://doi.org/10.1007/s00340-009-3521-0.

[54] Maffi S, Cignoli F, Bellomunno C, De Iuliis S, Zizak G. Spectral effects in laser induced incandescence application to flame-made titania nanoparticles. Spectrochim Acta - Part B At Spectrosc 2008;63:202–9. https://doi.org/10.1016/j.sab.2007.11.022.

[55] De Iuliis S, Migliorini F, Dondè R. Laser-induced emission of TiO2 nanoparticles in flame spray synthesis. Appl Phys B Lasers Opt 2019;125:219. https://doi.org/10.1007/s00340-019-7324-7.

[56] Daun KJ, Smallwood GJ, Liu F. Investigation of thermal accommodation coefficients in time-resolved laser-induced incandescence. J Heat Transfer 2008;130:1–9. https://doi.org/10.1115/1.2977549.

[57] Snelling DR, Thomson KA, Liu · F, Smallwood · G J, Liu F. Comparison of LII derived soot temperature measurements with LII model predictions for soot in a laminar diffusion flame. Appl Phys B 2009;96:657–69. https://doi.org/10.1007/s00340-009-3614-9.

[58] Talebi Moghaddam S, Daun KJ. Plasma emission during time-resolved laser-induced incandescence measurements of aerosolized metal nanoparticles. Appl Phys B Lasers Opt 2018;124:0. https://doi.org/10.1007/s00340-018-7028-4.

[59] Talebi-Moghaddam S, Sipkens TA, Daun KJ. Laser-induced incandescence on metal nanoparticles: validity of the Rayleigh approximation. Appl Phys B Lasers Opt 2019;125:1–16. https://doi.org/10.1007/s00340-019-7325-6.

[60] Will S, Schraml S, Leipertz A. Two-dimensional soot-particle sizing by time-resolved laser-induced incandescence. 1995.

[61] Goulay F, Schrader PE, Lopez-Yglesias X, Michelsen HA. A data set for validation of models of laser-induced incandescence from soot: Temporal profiles of LII signal and particle temperature. Appl Phys B Lasers Opt 2013;112:287–306. https://doi.org/10.1007/s00340-013-5504-4.

[62] Rohlfing EA, Chandler DW. Two-color pyrometric imaging of laser-heated carbon particles in a supersonic flow. Chem Phys Lett 1990;170:44–50. https://doi.org/10.1016/0009-2614(90)87087-8.

[63] Flower WL. Optical Measurements of Soot Formation in Premixed Flames. Combust Sci

Technol 1983;33:17–33. https://doi.org/10.1080/00102208308923666.

[64] Snelling DR, Smallwood GJ, Sawchuk RA, Neill WS, Gareau D, Clavel DJ, *et al*. In-Situ Real-Time Characterization of Particulate Emissions from a Diesel Engine Exhaust by Laser-Induced Incandescence. 2000.

[65] Daun K, Menser J, Mansmann R, Moghaddam ST, Dreier T, Schulz C. Spectroscopic models for laser-heated silicon and copper nanoparticles. J Quant Spectrosc Radiat Transf 2017;197:3–11. https://doi.org/10.1016/j.jqsrt.2016.10.006.

[66] Mansmann R, Sipkens TA, Menser J, Daun KJ, Dreier T, Schulz C. Detector calibration and measurement issues in multi-color time-resolved laser-induced incandescence. Appl Phys B 2019;125:126. https://doi.org/10.1007/s00340-019-7235-7.

[67] Bladh H, Johnsson J, Rissler J, Abdulhamid H, Olofsson NE, Sanati M, *et al*. Influence of soot particle aggregation on time-resolved laser-induced incandescence signals. Appl. Phys. B Lasers Opt., vol. 104, Springer; 2011, p. 331–41. https://doi.org/10.1007/s00340-011-4470-y.

[68] Snelling DR, Smallwood GJ, Liu F, Gülder ÖL, Bachalo WD. A calibration-independent laser-induced incandescence technique for soot measurement by detecting absolute light intensity 2005;44:6773–85.

[69] Sipkens TA, Menser J, Mansmann R, Schulz C, Daun KJ. Investigating temporal variation in the apparent volume fraction measured by time-resolved laser-induced incandescence. Appl Phys B Lasers Opt 2019;125:1–20. https://doi.org/10.1007/s00340-019-7251-7.

[70] Liu F, Yang M, Hill FA, Snelling DR, Smallwood GJ. Influence of polydisperse distributions of both primary particle and aggregate size on soot temperature in low-fluence LII. Appl Phys B Lasers Opt 2006;83:383–95. https://doi.org/10.1007/s00340-006-2196-z.

[71] Snelling D, Liu F, Smallwood GJ. Evaluation of the nanoscale heat and mass transfer model of LII: prediction of the excitation intensity . 2000.

[72] Craig F. Bohren DRH. Absorption and Scattering of Light by Small Particles. Canada: John Wiley & Sons, Inc.; 1998.

[73] Sorensen CM. Light scattering by fractal aggregates: A review. Aerosol Sci Technol 2001;35:648–87. https://doi.org/10.1080/02786820117868.

[74] Miller JC. Optical properties of liquid metals at high temperatures. Philos Mag 1969;20:1115–32. https://doi.org/10.1080/14786436908228198.

[75] Daun KJ. Discussion of ‘“ Normal Spectral Emissivity Measurement of Liquid Iron and Nickel Using Electromagnetic Levitation in Direct Current Magnetic Field .”’ Metall Mater Trans A 2016;47:3300–2. https://doi.org/10.1007/s11661-016-3527-2.

[76] Krishnan S, Yugawa KJ, Nordine PC. Optical properties of liquid nickel and iron

1997;55:8201–6.

[77] Shvarev KM, Baum BA, Gel'd P V. Optical properties and electronic characteristics of liquid solutions of nickel in silicon. Sov Phys J 1975;18:521–4. https://doi.org/10.1007/BF01093245.

[78] Ordal MA, Bell RJ, Alexander RW, Long LL, Querry MR. Optical properties of Au, Ni, and Pb at submillimeter wavelengths. Appl Opt 1987;26:744. https://doi.org/10.1364/ao.26.000744.

[79] Filippov A V., Zurita M, Rosner DE. Fractal-like aggregates: Relation between morphology and physical properties. J Colloid Interface Sci 2000;229:261–73. https://doi.org/10.1006/jcis.2000.7027.

[80] Draine BT, Flatau PJ. Discrete-Dipole Approximation For Scattering Calculations. J Opt Soc Am A 1994;11:1491. https://doi.org/10.1364/josaa.11.001491.

[81] Friedlander SK, Wang CS. The self-preserving particle size distribution for coagulation by brownian motion. J Colloid Interface Sci 1966;22:126–32. https://doi.org/10.1016/0021-9797(66)90073-7.

[82] Hinds WC. Aerosol Technology, Properties, Behavior, and Measurment of Airborne Particles. Second Edi. John Wiley & Sons Inc; 1999.

[83] Eremin A, Gurentsov E, Schulz C. Influence of the bath gas on the condensation of supersaturated iron atom vapour at room temperature. J Phys D Appl Phys 2008;41. https://doi.org/10.1088/0022-3727/41/5/055203.

[84] Lemaire R, Mobtil M. Modeling laser-induced incandescence of soot: a new approach based on the use of inverse techniques. Appl Phys B Lasers Opt 2015;119:577–606. https://doi.org/10.1007/s00340-015-6032-1.

[85] Hixson RS, Winkler MA, Hodgdon ML. Sound speed and thermophysical properties of liquid iron and nickel. Phys Rev B 1990;42:6485–91. https://doi.org/10.1103/PhysRevB.42.6485.

[86] Information National Center for Biotechnology. PubChem Element Summary for AtomicNumber 28, Nickel 2020. https://pubchem.ncbi.nlm.nih.gov/element/Nickel (accessed October 15, 2020).

[87] Rulison AJ, Rhim WK. Constant-pressure specific heat to hemispherical total emissivity ratio for undercooled liquid nickel, Zirconium, and Silicon. Metall Mater Trans B 1995;26:503–8. https://doi.org/10.1007/BF02653866.

[88] Pottlacher G, Jaeger H, Neger T. Thermophysical Measurements on Liquid Iron and Nickel. High Temp - High Press 1987;19:19–27.

[89] Desai PD. Thermodynamic properties of nickel. Int J Thermophys 1987;8:763–80.

https://doi.org/10.1023/A:1021783327988.

[90] Hofeldt DL. Real-time soot concentration measurement technique for engine exhaust streams. SAE Tech Pap 1993. https://doi.org/10.4271/930079.

[91] Liu F, Daun KJ, Snelling DR, Smallwood GJ. Heat conduction from a spherical nano-particle: Status of modeling heat conduction in laser-induced incandescence. Appl Phys B Lasers Opt 2006;83:355–82. https://doi.org/10.1007/s00340-006-2194-1.

[92] Watson KM. Thermodynamics of the Liquid State. Ind Eng Chem 1943;35:398–409. https://doi.org/https://doi.org/10.1021/ie50400a004.

[93] Li W, Davis & EJ, Dauis EJ. Aerosol Evaporation in the Transition Regime. Aerosol Sci Technol 1996;25:21. https://doi.org/10.1080/02786829608965375.

[94] Loyalka SK. Mechanics of aerosols in nuclear reactor safety: A review. Prog Nucl Energy 1983;12:1–56. https://doi.org/10.1016/0149-1970(83)90024-0.

[95] McCoy BJ, Cha CY. Transport phenomena in the rarefied gas transition regime. Chem Eng Sci 1974;29:381–8. https://doi.org/10.1016/0009-2509(74)80047-3.

[96] Kennard EH. Kinetic Theory of Gases. vol. 142. Nature Publishing Group; 1938. https://doi.org/10.1038/142494a0.

[97] Michelsen HA. Understanding and predicting the temporal response of laser-induced incandescence from carbonaceous particles. J Chem Phys 2003;118:7012–45. https://doi.org/10.1063/1.1559483.

[98] Kock BF, Tribalet B, Schulz C, Roth P. Two-color time-resolved LII applied to soot particle sizing in the cylinder of a Diesel engine. Combust Flame 2006;147:79–92. https://doi.org/10.1016/j.combustflame.2006.07.009.

[99] Kuhlmann SA, Reimann J, Will S. On heat conduction between laser-heated nanoparticles and a surrounding gas. J Aerosol Sci 2006;37:1696–716. https://doi.org/10.1016/j.jaerosci.2006.06.009.

[100] Dean JA. Lange's handbook of Chemistry. 15th ed. McGRAW-HILL, INC; 1999.

[101] Lu HM, Jiang Q. Surface tension and its temperature coefficient for liquid metals. J Phys Chem B 2005;109:15463–8. https://doi.org/10.1021/jp0516341.

[102] Young DA, Alder BJ. Critical point of metals from the van der Waals model. Phys Rev A 1971;3:364–71. https://doi.org/10.1103/PhysRevA.3.364.

[103] Lee H-K, Frohberg MG, Hajra JP. The determination of the surface tensions of liquid iron, nickel and iron-nickel alloys using the electromagnetic oscillating droplet technique. Steel Res 1993;64:191–6. https://doi.org/10.1002/srin.199301007.

[104] Keene BJ. Review of data for the surface tension of iron and its binary alloys. Int Mater Rev 1988;33:1–37. https://doi.org/10.1179/imr.1988.33.1.1.

[105] Kharab A, Guenther RB. An introduction to numerical methods: A MATLAB® approach, second edition. 2005.

[106] Shampine LF. Variable Order Adams Codes. vol. 44. 2002.

[107] The MathWorks Inc. MATLAB n.d.

[108] Sipkens TA, Daun KJ. Defining regimes and analytical expressions for fluence curves in pulsed laser heating of aerosolized nanoparticles. Opt Express 2017;25:5684. https://doi.org/10.1364/oe.25.005684.

[109] Menser J, Daun K, Dreier T, Schulz C. Laser-induced atomic emission of silicon nanoparticles during laser-induced heating. Appl Opt 2017;56:E50. https://doi.org/10.1364/ao.56.000e50.

[110] Olofsson NE, Johnsson J, Bladh H, Bengtsson PE. Soot sublimation studies in a premixed flat flame using laser-induced incandescence (LII) and elastic light scattering (ELS). Appl Phys B Lasers Opt 2013;112:333–42. https://doi.org/10.1007/s00340-013-5509-z.

[111] Big Sky Laser. User ’s Manual ULTRA CFR Nd:YAG Laser System 2007.

[112] Liu F, Rogak S, David ·, Snelling R, Meghdad Saffaripour ·, Thomson KA, *et al*. Effects of laser fluence non-uniformity on ambient-temperature soot measurements using the auto-compensating laser-induced incandescence technique. Appl Phys B 2016;122:286. https://doi.org/10.1007/s00340-016-6553-2.

[113] Polyakov S V. Photomultiplier Tubes. Exp. Methods Phys. Sci., vol. 45, Academic Press; 2013, p. 69–82. https://doi.org/10.1016/B978-0-12-387695-9.00003-2.

[114] Mansmann R, Dreier T, Schulz C. Performance of photomultipliers in the context of laser-induced incandescence 2017. https://doi.org/10.1364/AO.56.007849.

[115] Liu F, Snelling · D R, Thomson KA, Smallwood · G J. Sensitivity and relative error analyses of soot temperature and volume fraction determined by two-color LII. Appl Phys B 2009;96:623–36. https://doi.org/10.1007/s00340-009-3560-6.

[116] Manual I. Model 3076 Constant Output Atomizer 2005.

[117] Woo J, Chae EH, Kim SH, Ho J, Wook J, Mi S, *et al*. Preparation of fine Ni powders from nickel hydrazine complex 2006;97:371–8. https://doi.org/10.1016/j.matchemphys.2005.08.028.

[118] Bai L, Yuan F, Tang Q. Synthesis of nickel nanoparticles with uniform size via a modified hydrazine reduction route 2008;62:2267–70. https://doi.org/10.1016/j.matlet.2007.11.061.

[119] Chou K Sen, Huang KC. Studies on the chemical synthesis of nanosized nickel powder and its stability. J Nanoparticle Res 2001;3:127–32. https://doi.org/10.1023/A:1017940804321.

[120] Eluri R, Paul B. Synthesis of nickel nanoparticles by hydrazine reduction : mechanistic study and continuous flow synthesis 2012:1–14. https://doi.org/10.1007/s11051-012-0800-1.

[121] Wu SH, Chen DH. Synthesis and characterization of nickel nanoparticles by hydrazine reduction in ethylene glycol. J Colloid Interface Sci 2003;259:282–6. https://doi.org/10.1016/S0021-9797(02)00135-2.

[122] Wu ZG, Munoz M, Montero O. The synthesis of nickel nanoparticles by hydrazine reduction. Adv Powder Technol 2010;21:165–8. https://doi.org/10.1016/j.apt.2009.10.012.

[123] He F, Zhao D. Manipulating the size and dispersibility of zerovalent iron nanoparticles by use of carboxymethyl cellulose stabilizers. Environ Sci Technol 2007;41:6216–21. https://doi.org/10.1021/es0705543.

[124] Liu Y, Majetich SA, Tilton RD, Sholl DS, Lowry G V. TCE dechlorination rates, pathways, and efficiency of nanoscale iron particles with different properties. Environ Sci Technol 2005;39:1338–45. https://doi.org/10.1021/es049195r.

[125] Huang KC, Ehrman SH. Synthesis of iron nanoparticles via chemical reduction with palladium ion seeds. Langmuir 2007;23:1419–26. https://doi.org/10.1021/la0618364.

[126] He F, Zhao D, Liu J, Roberts CB. Stabilization of Fe-Pd Nanoparticles with Sodium Carboxymethyl Cellulose for Enhanced Transport and Dechlorination of Trichloroethylene in Soil and Groundwater 2007. https://doi.org/10.1021/ie0610896.

[127] Singh R, Misra V, Singh RP. Synthesis, characterization and role of zero-valent iron nanoparticle in removal of hexavalent chromium from chromium-spiked soil. J Nanoparticle Res 2011;13:4063–73. https://doi.org/10.1007/s11051-011-0350-y.

[128] Ruíz-Baltazar A, Esparza R, Rosas G, Pérez R. Effect of the Surfactant on the Growth and Oxidation of Iron Nanoparticles 2015. https://doi.org/10.1155/2015/240948.

[129] Lee PC, Melsel D. Adsorption and Surface-Enhanced Raman of Dyes on Silver and Gold Sols1. vol. 86. 1982.

[130] Sui Z, Chen X, Wang L, Chai Y, Yang C, Zhao J. An Improved Approach for Synthesis of Positively Charged Silver Nanoparticles. Chem Lett 2005;34. https://doi.org/10.1246/cl.2005.100.

[131] Abbaszadegan A, Ghahramani Y, Gholami A, Hemmateenejad B, Dorostkar S, Nabavizadeh M, *et al*. The Effect of Charge at the Surface of Silver Nanoparticles on Antimicrobial Activity against Gram-Positive and Gram-Negative Bacteria: A Preliminary Study 2015. https://doi.org/10.1155/2015/720654.

[132] Kumar S, Bhushan P, Bhattacharya S. Positively Charged Silver Nanoparticles as Labels for Paper-Based Colorimetric Detection of Heparin. Springer 2018. https://doi.org/10.1007/978-981-10-7554-4_41.

[133] Huang H, Yuan Q, Yang X. Preparation and characterization of metal-chitosan nanocomposites. Colloids Surfaces B Biointerfaces 2004;39:31–7. https://doi.org/10.1016/j.colsurfb.2004.08.014.

[134] Hu S, Gu F, Chen M, Wang C, Li J, Yang J, *et al*. A novel method for identifying and distinguishing Cryptococcus neoformans and Cryptococcus gattii by surface-enhanced Raman scattering using positively charged silver nanoparticles. Sci Rep 2020;10:12480. https://doi.org/10.1038/s41598-020-68978-0.

[135] Mulfinger L, Solomon SD, Bahadory M, Jeyarajasingam A V., Rutkowsky SA, Boritz C. Synthesis and Study of Silver Nanoparticles. J Chem Educ 2007;84:322. https://doi.org/10.1021/ed084p322.

[136] Livingston JD, Carpay FMA. Controlled Nucleation for the Regulation of the Particle Size in Monodisperse Gold Suspensions. Nat Phys Sci 1973;241:20.

[137] Leng Y. Materials Characterization: Introduction to Microscopic and Spectroscopic Methods. Second. Wiley-VCH; 2013.

[138] Alexander M, Dalgleish DG. Dynamic light scattering techniques and their applications in food science. Food Biophys 2006;1:2–13. https://doi.org/10.1007/s11483-005-9000-1.

[139] Cordouan Technologies. NanoQTM & Vasco Series Instruction Guide. 2016.

[140] Bhattacharjee S. DLS and zeta potential - What they are and what they are not? J Control Release 2016;235:337–51. https://doi.org/10.1016/j.jconrel.2016.06.017.

[141] Willets KA, Van Duyne RP. Localized Surface Plasmon Resonance Spectroscopy and Sensing 2007. https://doi.org/10.1146/annurev.physchem.58.032806.104607.

[142] Kaszuba M, Corbett J, Watson FMN, Jones A. High-concentration zeta potential measurements using light-scattering techniques. Philos. Trans. R. Soc. A Math. Phys. Eng. Sci., vol. 368, Royal Society; 2010, p. 4439–51. https://doi.org/10.1098/rsta.2010.0175.

[143] Cordouan Technologies. Wallis - Zeta Potential Analyzer. n.d.

[144] Amendola V, Meneghetti M. Size evaluation of gold nanoparticles by UV-vis spectroscopy. J Phys Chem C 2009;113:4277–85. https://doi.org/10.1021/jp8082425.

[145] Thompson R. A Note on Restricted Maximum Likelihood Estimation with an Alternative Outlier Model. J R Stat Soc Ser B 1985;47:53–5. https://doi.org/10.1111/j.2517-6161.1985.tb01329.x.

[146] Menser J, Daun K, Dreier T, Schulz C. Transition from laser-induced incandescence (LII)

to laser-induced breakdown (LIBS). LII Work., LII Workshop; 2018.

[147] Lehre T, Suntz R, Bockhorn H. Time-resolved two-color LII: Size distributions of nano-particles from gas-to-particle synthesis. Proc Combust Inst 2005;30:2585–93. https://doi.org/10.1016/j.proci.2004.08.113.

[148] Aster RC, Borchers B, Thurber CH. Parameter Estimation and Inverse Problems. Second. Elsevier; 2013.

[149] Logan DJ, Wolesensky W. Mathematical Methods in Biology . John Wiley & Sons Inc; 2009.

[150] Liu F, Smallwood GJ. Relationship between soot volume fraction and LII signal in AC-LII: Effect of primary soot particle diameter polydispersity. Appl Phys B Lasers Opt 2013;112:307–19. https://doi.org/10.1007/s00340-012-5330-0.

[151] Atkins P, Paula J de. Physical Chemistry for the Life Sciences. 8th ed. Oxford; 2006.

[152] Casimir HBG, Polder D. The influence of retardation on the London-van der Waals forces. Phys Rev 1948;73:360–72. https://doi.org/10.1103/PhysRev.73.360.

[153] Rodriguez AW, Capasso F, Johnson SG. The Casimir effect in microstructured geometries. Nat Photonics 2011;5:211–21. https://doi.org/10.1038/nphoton.2011.39.

[154] Kristyhn S, Pulay P. Can (semi) local density functional theory account for the London dispersion forces? vol. 229. 1994.

[155] Vargaftik NB, Filippov LP, Tarzimanov AA, Totskii EE. Handbook of Thermal Conductivity of Liquids and Gases - Natan B. Vargaftik - Google Books. CRC; 1994.

[156] Daun KJ, Huberman SC. Influence of particle curvature on transition regime heat conduction from aerosolized nanoparticles 2012. https://doi.org/10.1016/j.ijheatmasstransfer.2012.07.076.

[157] Bird GA. Molecular gas dynamics and the direct simulation of gas flows. sher Oxford : Clarendon Press ; New York : Oxford University Press; 1996.

[158] Inoue S, Matsumura Y. Molecular dynamics simulation of metal coating on single-walled carbon nanotube. Chem Phys Lett 2008;464:160–5. https://doi.org/10.1016/j.cplett.2008.09.014.

[159] Talebi-Moghaddam S, Robinson-Enebeli S, Sipkens TA, Klinkova A, Daun KJ. Investigating non-incandescence emission during laser induced incandescence experiments on aerosolized plasmonic nanoparticles. Proc. Int. Symp. Radiat. Transf., vol. 2019- June, Begell House Inc.; 2019, p. 153–61. https://doi.org/10.1615/RAD-19.190.

[160] Talebi-Moghaddam S, Robinson-Enebeli S, Clavel DJ, Smallwood GJ, Daun KJ. Anomalous cooling during laser-induced incandescence experiments on carbonaceous

nanoparticles. Gordon Res. Conf., Gordon Research Conferences; 2019.

[161] Talebi-Moghaddam S, Robinson-Enebeli S, Corbin JC, Klinkova A, Smallwood GJ, Daun KJ. Multi-photo induced photoluminescence emission during time-resolved laser-induced incandescence experiments on silver and gold nanoparticles. 4th Int. Symp. Gas-Phase Synth. Funct. Nanomater., 4th International Symposium Gas-Phase Synthesis of Functional Nanomaterials; 2020.

[162] Eichelbaum M, Schmidt BE, Ibrahim H, Rademann K. Three-photon-induced luminescence of gold nanoparticles embedded in and located on the surface of glassy nanolayers. Nanotechnology 2007;18:8. https://doi.org/10.1088/0957-4484/18/35/355702.

[163] Roloff L, Klemm P, Gronwald I, Huber R, Lupton JM, Bange S. Light Emission from Gold Nanoparticles under Ultrafast Near-Infrared Excitation: Thermal Radiation, Inelastic Light Scattering, or Multiphoton Luminescence? Nano Lett 2017;17:25. https://doi.org/10.1021/acs.nanolett.7b04266.

[164] Pattabi M, Pattabi RM. Photoluminescence from Gold and Silver Nanoparticles. Nano Hybrids 2014;6:1–35. https://doi.org/10.4028/www.scientific.net/nh.6.1.

[165] Huang T, Murray RW. Luminescence of tiopronin monolayer-protected silver clusters changes to that of gold clusters upon galvanic core metal exchange. J Phys Chem B 2003;107:7434–40. https://doi.org/10.1021/jp0276956.

[166] Rodrigo AG, Tsai P, Shearman H. On the Use of Bootstrapped Topologies in coalescent-Based Bayesian McMc Inference: A comparison of estimation and Computational Efficiencies. 2009.

[167] Han K, Kim W, Yu J, Lee J, Lee H, Gyu C, *et al*. A study of pin-to-plate type spark discharge generator for producing unagglomerated nanoaerosols. J Aerosol Sci 2012;52:80–8. https://doi.org/10.1016/j.jaerosci.2012.05.002.

[168] Crosland BM, Johnson MR, Thomson KA. Analysis of uncertainties in instantaneous soot volume fraction measurements using two-dimensional, auto-compensating, laser-induced incandescence (2D-AC-LII). Appl Phys B Lasers Opt 2011;102:173–83. https://doi.org/10.1007/s00340-010-4130-7.

[169] Baker S, Cousins RD. Clarification of the use of CHI-square and likelihood functions in fits to histograms. Nucl Instruments Methods Phys Res 1984;221:437–42. https://doi.org/10.1016/0167-5087(84)90016-4.

[170] Serang O, Maccoss MJ, Noble WS. Efficient Marginalization to Compute Protein Posterior Probabilities from Shotgun Mass Spectrometry Data n.d. https://doi.org/10.1021/pr100594k.

[171] Nocedal J, Wright SJ. Numerical Optimization. Second. Springer; n.d.

[172] Modest MF. Inverse Radiative Heat Transfer., Academic Press; 2003, p. 729–42.

https://doi.org/10.1016/B978-012503163-9/50023-0.

[173] Griva I, Nash SG, Sofer A. Linear and Nonlinear Optimization. second. Society for Industrial and Applied Mathematics; 2009.

[174] Colemant TF, Lit Y. A reflective newton method for minimizing a quadratic function subject to bounds on some of the variables. vol. 6. 1996.

[175] Branch MA, Coleman TF, Li Y. A Subspace, Interior, and Conjugate Gradient Method for Large-Scale Bound-Constrained Minimization Problems. Http://DxDoiOrg/101137/S1064827595289108 2006. https://doi.org/10.1137/S1064827595289108.

[176] Kelner V, Capitanescu F, Léonard O, Wehenkel L. A hybrid optimization technique coupling an evolutionary and a local search algorithm. J Comput Appl Math 2008;215:448–56. https://doi.org/10.1016/j.cam.2006.03.048.

[177] Goldberg DE. Genetic Algorithms in Search, Optimization & Machine Learning. Addision-Wesley; 1989.

[178] Liu F, Smallwood GJ. Effect of aggregation on the absorption cross-section of fractal soot aggregates and its impact on LII modelling. J Quant Spectrosc Radiat Transf 2010;111:302–8. https://doi.org/10.1016/j.jqsrt.2009.06.017.

[179] Snelling DR, Thomson KA, Smallwood GJ, Gülder ÖL, Weckman EJ, Fraser RA. Spectrally Resolved Measurement of Flame Radiation. AIAA J 2002;40:2002.

[180] Wooten F. Optical properties of solids. Academic Press Inc (london); 1972.

[181] Eggersdorfer ML, Pratsinis SE. Agglomerates and aggregates of nanoparticles made in the gas phase. Adv Powder Technol 2014;25:71–90. https://doi.org/10.1016/j.apt.2013.10.010.

[182] Hofmann S, Sharma R, Ducati C, Du G, Mattevi C, Cepek C, *et al*. In situ observations of catalyst dynamics during surface-bound carbon nanotube nucleation. Nano Lett 2007;7:602–8. https://doi.org/10.1021/nl0624824.